The Dissertation Committee for Aaron D. Barr
certifies that this is the approved version of the following dissertation:

Isotope Ratios for Medicine and Public Health

Committee:

Mark G. Raizen, Supervisor

Steven A. Abrams

Vernita Gordon

Keji Lai

Chih-Kang Shih

Isotope Ratios for Medicine and Public Health

by

Aaron D. Barr

Dissertation

Presented to the Faculty of the Graduate School of
The University of Texas at Austin
in Partial Fulfillment
of the Requirements
for the Degree of

Doctor of Philosophy

The University of Texas at Austin
May 2026

Acknowledgments

My sincere thanks and warmest gratitude go first of all to my advisor, Prof. Mark Raizen. Working in the Raizen group these past few years has been both a joy and a privilege. Some physicists produce brilliant original research, while others are talented at building and managing groups; Mark is one of those few who excel at both roles. Not many groups pursue as wide an array of interesting simultaneous research avenues; few groups as large as the Raizen group are able to maintain the genial esprit de corps that has transformed the grim, sunless basement laboratory spaces of UT's PMA building into a genuinely fun place to be.

I would like to thank the members of my committee for their support and encouragement, particularly Prof. Steven Abrams, whose expertise was essential in creating this project in the first place. Profs. Vernita Gordon, Keji Lai, and Chih-Kang Shih have known both me and my sister since we were undergraduates, and my thanks go to them for all their support.

Thanks are due as well to my previous advisors: Prof. Linda Reichl, with whom I worked through part of my undergraduate physics career and the first half of my graduate program, as well as Prof. Roy Schwitters, who sadly passed away in 2023.

My warmest regards go to the Raizen group, past and present. V.J. Ajith, who joined the lab as a postdoc at the same time I joined as PhD student, is an essential part of all the research in this dissertation; his experimental expertise and support at every step were literally invaluable.

Logan Hillberry and Yi Xu, of the prior generation of graduate students, were extremely generous with their time in helping me when I was first getting started in the lab, despite both being in the process of preparing for their final defenses, and I remain very grateful.

Kevin Melin and David Medellin, former graduate students of a yet earlier vintage, who nevertheless still appear in the lab from time to time like the Ghost of Christmas Past, have been tremendously helpful as a continual source of technical support, advice, and uncanny recollections of where old pieces of equipment are located.

Jason Boynewicz, Cole Thumann, and Zachary Morrison, the other lab members who overlapped with the Hillberry-Xu Era, have been a continual source of optimistic good cheer, lunchtime companionship, and inspiring experimental physics work.

Ahmed Helal, a research scientist now happily returned to the group, is owed a special thanks for his old vacuum chamber and optics, which were incorporated into our very first iron isotope spectroscopy setup.

Henry Chance and Joshua Fabre, the other members of the "Isotope Office," who are in the process of realizing the strontium separation discussed in Chapter 3, have been the best colleagues you could ask for; their drive, intellectual curiosity, and good-natured friendliness are an example to us all.

I'd like to thank Sam Lund for helping overcome the activation barrier to a desperately-needed lab reorganization process, and also for the *thematically-appropriate*[1] cookies she made for my doctoral defense.

Paromita Cesano Bagchi, who is doing fascinating work at the J.J. Pickle Research Campus (and who we consequently see less often than we all wish we did), and Mitchell Gale, the freshest of our recruits, both make the lab a better place to be.

Our undergraduates, Isabella Kazen and Zoey Lee, have done excellent work on questions related to sample ashing and preparation, and this is no doubt the beginning of brilliant careers for them both, whatever they may turn to next.

---

[1] Hint: imagine if gingerbread men had circulatory systems.

Special recognition also goes to Patrick Obi, now researching physics education under Prof. Michael Marder, who contributed to the early work on the dry ashing process and microsample preparation methods.

Thanks are due as well to Alicia, Sandy, and Max Born Raizen for graciously hosting me and the other group members at their home on multiple occasions.

Lastly, I want to thank my mother and sister, who have been endlessly supportive in countless ways. Since my sister is *also* partway through a materials science PhD program at MIT, it will be my turn to be endlessly supportive soon enough. Not many people have the privilege of physics siblings or mothers who can talk you through your real analysis homework, but I highly recommend it.

Abstract

Isotope Ratios for Medicine and Public Health

Aaron D. Barr, PhD
The University of Texas at Austin, 2026

SUPERVISOR: Mark G. Raizen

Isotopes hold the promise of great advances in medicine and public health. When used as tracers, rare stable isotopes can disentangle the causes and effects of disease, quantify the bioavailability of nutrients, or probe the details of complex metabolic processes, while changes in isotope ratios in the body can provide pathways to the development of novel methods for early disease detection. Radioisotopes are essential for modern medical imaging, diagnostics, and radiopharmaceuticals.

This project concerns the use of naturally occurring, stable iron isotopes as metabolic tracers for research into iron deficiency, and the more severe iron deficiency anemia, in infants and small children. Stable isotope studies are able to provide information regarding nutrient metabolism that is otherwise difficult to obtain, particularly in children. Examples include the relation of iron metabolism to growth and development, the effects of diet on iron bioavailability, the impact of acute and chronic illnesses on iron absorption and metabolism, as well as quantitative evaluation of the optimal iron intake for infants.

Our overall objective is to help address an unmet need in medicine for scalable analysis of stable isotope ratios from biological samples. What we are developing is intended to be an alternative to mass spectrometry, but with significant advantages in cost and scalability. Concurrently, we are pushing the envelope on detection efficiency

with ultra-small sample sizes. The goal is, ultimately, to make isotope ratio analysis cheap and straightforward enough to be used for routine medical screening.

Along the way, we are adapting spectroscopic techniques from AMO physics and sample preparation methods used by biochemists. We are also working on developing new fast methods for preparing microsamples of blood for analysis. Thanks to the elemental specificity of optical spectroscopy techniques, we can achieve high sensitivity with very minimal sample preparation. The current object of study is iron isotopes, but what we learn here will be adapted to a wide variety of medically significant elements in the future.

The perennial limiting factor in medical and scientific use of isotopes is supply; isotopically enriched samples have historically been subject to both limited availability and high costs. Our group is conducting active research into separation methods for isotopes of medical and scientific interest, and Chapter 3 concerns this work. Chapter 4 covers a fruitful experimental sideline into atom/surface interactions, which may prove useful in a range of medically-applicable optical spectroscopy and quantum sensing applications.

Table of Contents

List of Tables 11
List of Figures 12
Chapter 1: Isotope Ratio Analysis for Medicine 14
  1.1 Experiment objectives 17
  1.2 Isotope ratios in medicine 18
    1.2.1 Isotopes: a brief history 18
    1.2.2 Biological isotope fractionation 25
    1.2.3 Biological fractionation: diagnostic marker of disease 30
    1.2.4 Rare isotopes as metabolic tracers 35
  1.3 Iron and iron deficiency 42
    1.3.1 Effects of pediatric iron deficiency 43
    1.3.2 Iron deficiency and public health 45
    1.3.3 Bioavailability studies 47
    1.3.4 Scarcity of pediatric data 51
Chapter 2: Experimental / Technical Background 53
  2.1 Protocol for stable isotope tracer studies 53
    2.1.1 Sequence for analysis 54
    2.1.2 Alternative to mass spectrometry 61
    2.1.3 Pediatric blood draw 62
  2.2 Sample preparation 64
    2.2.1 Wet/dry methods: capillary tubes and blood spot cards 65
    2.2.2 Dry ashing 67
    2.2.3 Sample compaction 70
    2.2.4 Microsamples 73
  2.3 Laser-induced fluorescence spectroscopy 77
    2.3.1 372 nm transition 78
    2.3.2 Isotope shifts 80
    2.3.3 Collimation and Doppler broadening 84
    2.3.4 Optical setup 87
  2.4 Results 89

Chapter 3: Stable Isotope Separation for Medicine 90
- 3.1 Calutrons: the old method 90
  - 3.1.1 The U.S. calutron program 91
  - 3.1.2 Isotope supply issues 92
- 3.2 MAGIS/MRLIS 94
  - 3.2.1 Failure of AVLIS to replace calutrons 94
  - 3.2.2 Difficulty of laser separation methods 96
  - 3.2.3 MAGIS 96
  - 3.2.4 MRLIS 98
  - 3.2.5 Large mode volume cavity simulation 102
  - 3.2.6 Non-parallelism/incidence angle effects 105
  - 3.2.7 Advantages of CW lasers 109
  - 3.2.8 Comparison with pulsed lasers 111
  - 3.2.9 Applications 113

Chapter 4: Atomic Thermalization by Weak Adsorption on Polymer Films . 119
- 4.1 Producing thin polymer films 121
  - 4.1.1 Theory 122
  - 4.1.2 Apparatus 126
  - 4.1.3 Thickness estimation 126
- 4.2 Polymer scattering of Fe / Yb 127
  - 4.2.1 Estimation of scattered atom temperature 131
  - 4.2.2 Coated/uncoated QCM crystals 134
  - 4.2.3 Chilled substrates: TEC and LN2 137
- 4.3 Numerical model 140

Chapter 5: Future Directions 144
- 5.1 Push to 1-drop detection 144
- 5.2 Ionization spectroscopy 144
- 5.3 Isotope separation 144
- 5.4 Isotope detection in other elements 144
- 5.5 Scaleup of blood sample handling 145

Bibliography 146

List of Tables

3.1 Strontium separation parameters 115

List of Figures

1.1 CBQS laboratories 15
1.2 CBQS external collaborators 16
1.3 Frederick Soddy and Ernest Rutherford 19
1.4 Thorium decay products 20
1.5 Henry Moseley and Dr. Margaret Todd 22
1.6 J. J. Thomson and neon m/q apparatus 23
1.7 Neon m/q parabolas and Francis Aston's spectrograph 25
1.8 Urey, Bigeleisen, and Goeppert-Mayer 26
1.9 Osteoblasts and osteoclasts in developing bone 31
1.10 Structural hierarchy of collagen 32
1.11 George de Hevesy and Ole Chievitz 35
1.12 Rutherford's laboratory building, 1906 36
1.13 27″ Berkeley cyclotron, 1935 38
1.14 Whole-body count apparatus for isotope tracers 40
1.15 Hemoglobin molecular structure 42
1.16 Neurological development timeline 44
1.17 Global anemia prevalence for women in 2019 46
1.18 Nutrisano beverage and supplements 50
1.19 Moroccan tea 51

2.1 Ferritin storing Fe^{3+} ions 54
2.2 Protocol for stable iron isotope tracer studies 55
2.3 Schematics from 1953 patent of Coulter counter 58
2.4 Modern flow cytometer 59
2.5 Dried blood spot card and capillary tube sampling 63
2.6 Chain of blood sample processing 64
2.7 Dried blood spot cards and capillary sampling tubes 65
2.8 Whole blood samples before and after dry ashing 69
2.9 Hardened surface on heated blood samples 70
2.10 Manual tamping process for iron oxide powder samples 72
2.11 Microsample ashing procedure 74
2.12 Rotary sample holder and collimator 75

2.13 Hematite, magnetite, and wüstite 78
2.14 Level scheme of 372 nm transition of atomic iron 79
2.15 King plot for 372 nm transition of iron 82
2.16 Relative abundances of naturally-occurring stable iron isotopes 83
2.17 Hyperfine structure components for 372 nm transition in ^{57}Fe 84
2.18 Velocity-selection effect of collimation on a point source 85
2.19 Optical setup for iron isotope spectroscopy 87
2.20 Optical diagram for iron isotope spectroscopy 88
2.21 Iron isotope spectrum from 150 μg blood microsample 89

3.1 Calutron operators at Y-12 plant, 1944 90
3.2 Calutron alpha “racetrack” 91
3.3 ONRL stable isotope separation calutrons 93
3.4 U-AVLIS schematic and LLNL dye laser corridor 95
3.5 MAGIS magnetic-state optical pumping scheme 97
3.6 Simulation of MAGIS 98
3.7 MRLIS schematic 100
3.8 Numerical simulation of cavity transmission coefficients 101
3.9 Numerical simulation of laser beam incidence angle on cavity 106
3.10 Numerical simulation of effect of mirror non-parallelism 108
3.11 Optical pumping scheme for photoionization 114
3.12 CW and pulsed un-ionized fraction 117

4.1 100 micron PDMS film 120
4.2 Optical microscope image of PDMS surface 122
4.3 Instras spin-coater 126
4.4 Silane ring molecules D4, D5, and D6 127
4.5 Experimental setup for Fe and Yb surface scattering 128
4.6 Ytterbium oven cross-section 129
4.7 Ytterbium oven and chamber 130
4.8 Fe/Yb fluorescence spectra 131
4.9 Voigt fit to collimated beam / scattered fluorescence spectrum 132
4.10 Histogram of estimated temperatures 133
4.11 Coated/uncoated QCM crystals exposed to Yb beam 137
4.12 Yb fluorescence spectra and maximum fluorescence intensity 139
4.13 Temperature reduction via scattering 142

Chapter 1: Isotope Ratio Analysis for Medicine

Isotopes hold the promise of great advances in medicine and public health. When used as tracers, rare stable isotopes can disentangle the causes and effects of disease, quantify the bioavailability of nutrients, or probe the details of complex metabolic processes, while changes in isotope ratios in the body can provide pathways to the development of novel methods for early disease detection [1]. Radioisotopes are essential for modern medical imaging, diagnostics, and radiopharmaceuticals [2, 3, 4].

This project concerns the use of naturally occurring, stable iron isotopes as metabolic tracers for research into iron deficiency, and the more severe iron deficiency anemia, in infants and small children. Stable isotope studies are able to provide information regarding nutrient metabolism that is otherwise difficult to obtain, particularly in children. Examples include the relation of iron metabolism to growth and development, the effects of diet on iron bioavailability, the impact of acute and chronic illnesses on iron absorption and metabolism, as well as quantitative evaluation of the optimal iron intake for infants. We have been very fortunate to pursue this line of research in partnership with Prof. Steven Abrams, M.D., a researcher, professor, and pioneer of stable isotope methods, particularly in children. From a personal standpoint, this has been a very exciting and promising topic to work on for many reasons, but I will highlight two here. First, it is an interesting challenge from a technical perspective; we are adapting tried-and-true ultra-high sensitivity AMO physics techniques to novel biomedical applications, and developing new sample handling methods as we do so. Second, and most importantly, this project has the potential to meaningfully impact a longstanding public health issue of global significance.

The work in this dissertation is one facet of a larger multi-project / multi-institution initiative. We are the stateside, co-founding lab of the Center for Biomedical Quantum Sensing (CBQS), operating on a \$22 million, 6-year grant from the Novo Nordisk Foundation (NNF) in Denmark [5]. The leadership of CBQS is shared among three group co-leaders: Mark Raizen at the University of Texas at Austin (UT Austin), Eugene Polzik at the Niels Bohr Institute Quantum Optics Center (NBI-QUANTOP), and Ulrik Andersen at the Technical University of Denmark (DTU).

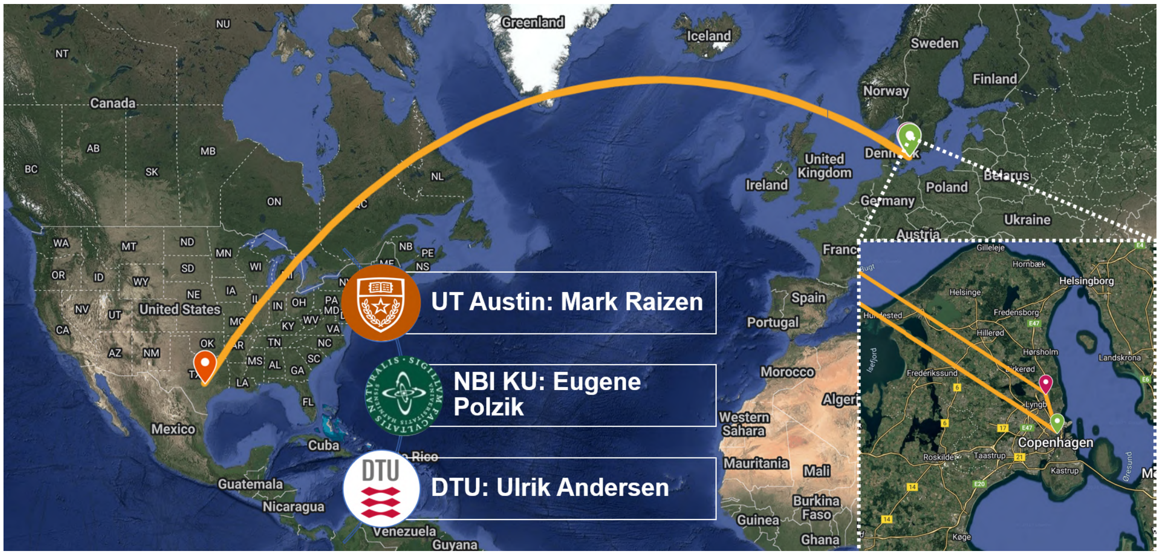

Figure 1.1: Center for Biomedical Quantum Sensing laboratories [5].

The goal of the Center is to "develop and use novel quantum sensing principles and techniques for biomedical diagnostics... providing ultra-sensitive platforms for early detection of disease and facilitating profound investigations into molecular systems at an unprecedented scale and precision [6]." The intent is for CBQS to foster a collaborative, interdisciplinary approach, applying the techniques of physics research to medicine. This exchange, it is hoped, will facilitate a fruitful and beneficial partnership between physicians, medical researchers, and quantum physicists. To that end, CBQS has a broad constellation of external collaborators, encompassing a wide range of medical and physics research expertise [7].

Although it is now part of the CBQS collaboration, the earliest work on this project predates the awarding of the NNF grant, having originated under the auspices of the nonprofit Pointsman Foundation, of which Mark Raizen is the Founder, Chairman of the Board, and President [8]. The Pointsman Foundation supports a range of

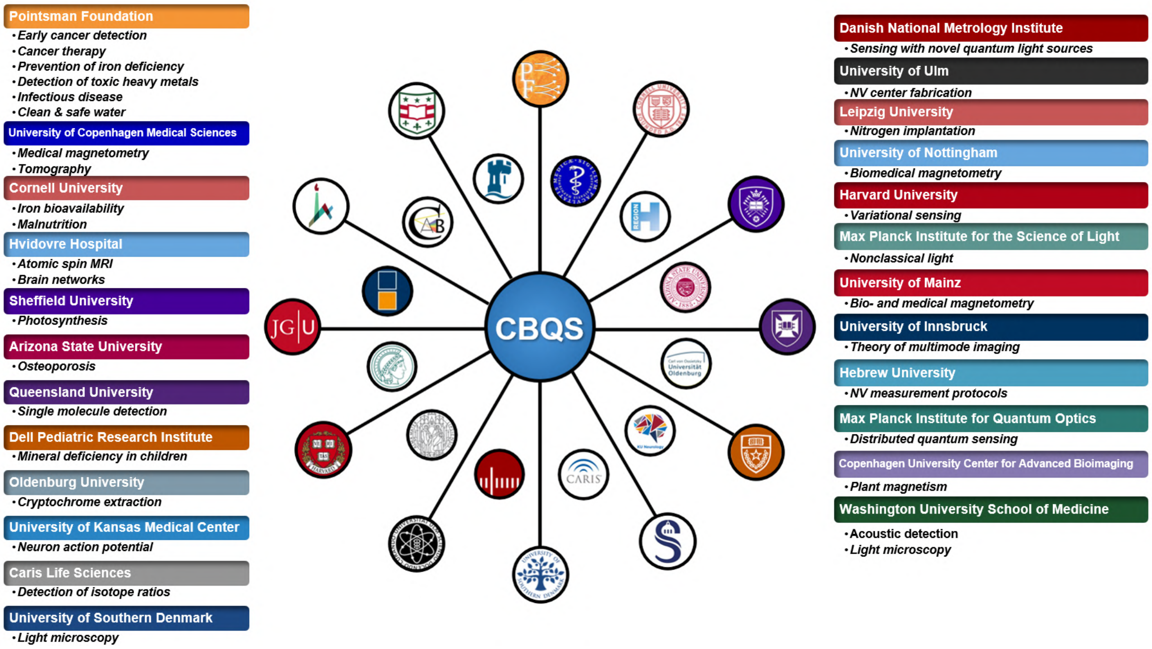

Figure 1.2: CBQS external collaborators [7].

projects that aim to “bring advances in the physical sciences to benefit humanity,” including the early detection of cancer, the production of clean and sterile water, and the detection of toxic heavy metal contamination in food. The current operating model of the Foundation is to principally fund projects through the production and sale of medical isotopes, particularly ^{176}Yb, which is in high demand as a precursor for ^{177}Lu, a β-emitting radioisotope used in the production of radiopharmaceuticals such as Lutathera and Pluvicto from Swiss-based pharmaceutical corporation Novartis [9, 10]. The isotope separation method employed by the Pointsman Foundation is discussed in greater detail in Chapter 3. At the end of the current funding period, the Pointsman and the Novo Nordisk Foundations plan to establish a joint research center in Copenhagen, Denmark.

1.1 Experiment objectives

Before delving into the experimental details, it would be a good idea to first provide a big-picture overview of what we hope to achieve with this project. The overall objective is to help address an unmet need in medicine for routine analysis of stable isotope ratios from biological samples. What we are developing is intended to be an alternative to mass spectrometry, but with significant improvements in cost and scalability. Concurrently, our aim is to push the envelope on detection efficiency with ultra-small sample sizes. The current target, which should be achieved early next year[1], is to perform isotope spectroscopy of iron using single-drop blood samples. Our hope is, ultimately, to make isotope ratio analysis cheap and straightforward enough to be used for routine medical screening.

Along the way, we are adapting spectroscopic techniques from AMO physics and sample preparation methods used by biochemists. We are working on developing new fast methods for preparing microsamples of blood for analysis. Thanks to the elemental specificity of optical spectroscopy techniques, we can achieve high sensitivity with very minimal sample preparation. The current object of study is iron isotopes, but in future what we learn here will be adapted to a wide variety of medically significant elements.

The perennial limiting factor in medical and scientific use of isotopes is supply; isotopically enriched samples have historically been subject to both limited availability and high costs. Our group is conducting active research into separation methods for isotopes of medical and scientific interest, and Chapter 3 concerns this work. Chapter 4 covers a fruitful experimental sideline into atom/surface interactions, which may prove useful in a range of medically-applicable optical spectroscopy and quantum sensing applications.

---

[1] 2026.

1.2 Isotope ratios in medicine

This research has two distinct modes of application. One mode makes use of enriched rare stable isotopes administered as metabolic tracers; this mode is considered in detail in Section 1.2.4 and elsewhere. The second mode involves the phenomenon of biological fractionation, the small but measurable changes in the natural isotope ratios of particular elements in the body, caused by disease. These changes provide a potential pathway to early diagnosis of serious medical conditions when they are most treatable. The mechanisms of biological fractionation of isotopes can be complex. However, there are a few key mechanisms: in chemical equilibrium effects, heavier isotopes tend to concentrate in the chemical species with stronger bonds and lower vibrational energies; isotopes may also be fractionated by transport mechanisms like ion channels and pumps, which can discriminate between isotopes due to size or binding energy differences; enzymes and metal binding proteins have also been observed to slightly fractionate isotopes for analogous reasons.

Medicine and the physics of isotopes have a deeply interwoven history, from Henri Becquerel's 1896 discovery of radioactivity in uranium salts to present-day isotope tracers and radiopharmaceuticals [11]. While the major work of the various Nobel laureates and scientific luminaries who advanced atomic and nuclear physics in the 20th century is generally well known, their significant contributions to medicine are often not. These underappreciated contributions, as well as important background for the physics of biological isotope effects, are briefly outlined in the following subchapters; understanding this co-evolution helps to contextualize the experiments in this dissertation.

1.2.1 Isotopes: a brief history

In a 1913 *Nature* paper, British chemist Frederick Soddy proposed the idea of isotopes to explain a phenomenon that had been baffling early radiochemists for over a decade: some of the daughter products of radioactive elements are chemically

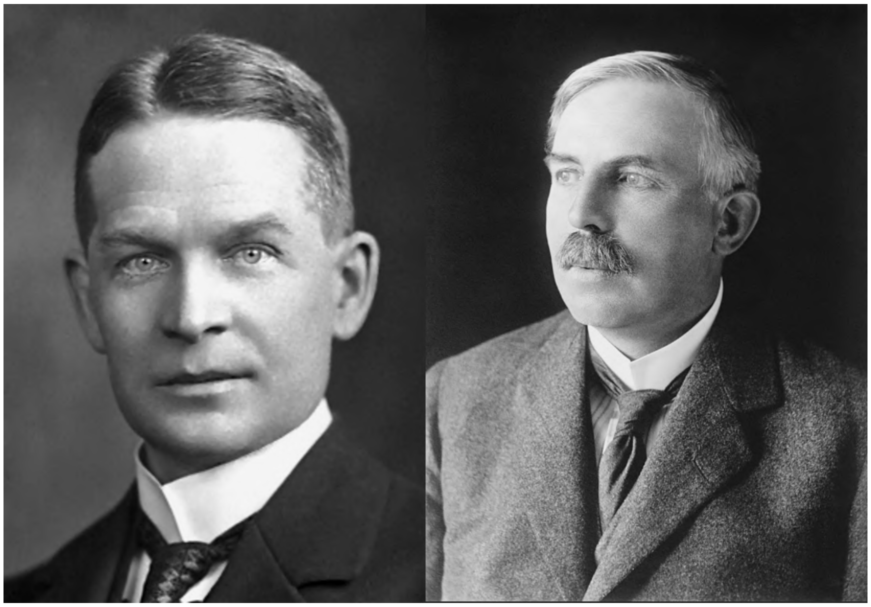

Figure 1.3: Left: Frederick Soddy. Right: Ernest Rutherford. Both photographs taken in the 1920s. [12, 13]

indistinguishable from known elements, yet their decay signatures are distinctly different. For example, a 1907 paper described a decay product of thorium, termed "radiothorium," that is chemically inseparable from thorium. However, instead of the expected 14-billion year half-life of familiar thorium, radiothorium's half-life is less than 2 years: "It is ... probable that the decrease in activity of thorium preparations, which we observed after numerous chemical treatments, was the result solely of the decay of radiothorium [14]." "Thorium X," another thorium decay product, was described in a 1909 paper in which the authors were unable to find "any differences in the chemical behaviour of radium [and] thorium X [15, 16]." However, thorium X has a half-life of only 3.6 days, compared to the expected 1,600 years for radium. By 1913, a large and confusing menagerie of such mysterious "radioelements" had been identified. The cluttered, ad-hoc nomenclature of the thorium decay chain suggests a dire need for some systematizing idea: "mesothorium-1 and mesothorium-2," "radiothorium," "thorium X," "thorium emanation," as well as "thorium A, B, and C" [15, 17].

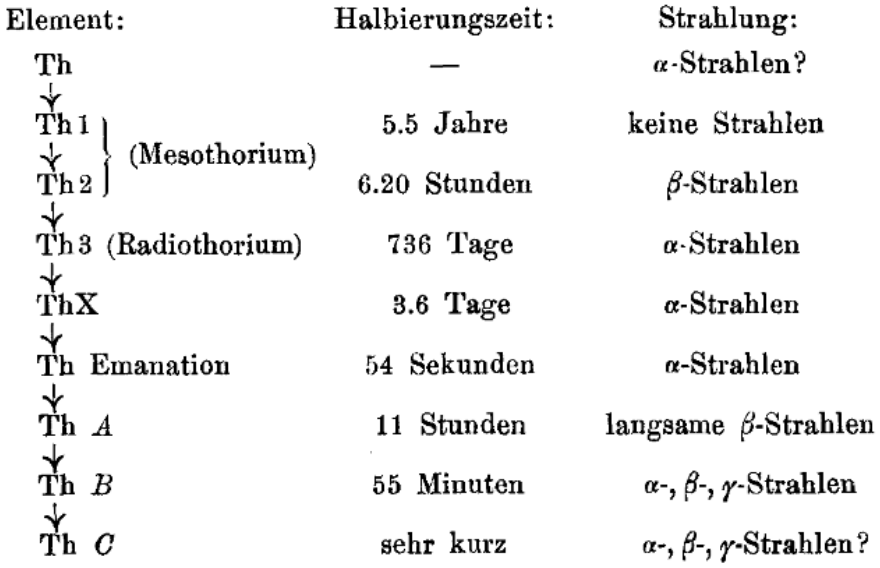

Element:	Halbierungszeit:	Strahlung:
Th	—	α-Strahlen?
Th 1 } (Mesothorium)	5.5 Jahre	keine Strahlen
Th 2	6.20 Stunden	β-Strahlen
Th 3 (Radiothorium)	736 Tage	α-Strahlen
ThX	3.6 Tage	α-Strahlen
Th Emanation	54 Sekunden	α-Strahlen
Th *A*	11 Stunden	langsame β-Strahlen
Th *B*	55 Minuten	α-, β-, γ-Strahlen
Th *C*	sehr kurz	α-, β-, γ-Strahlen?

Figure 1.4: Identification of thorium decay products as of 1909. [15]

Fortunately, 1913 turned out to be a year of tremendous advances in the physics of isotopes. British physicist Henry Moseley, working in Rutherford's lab in Manchester, derived an empirical formula for the frequency of X-rays emitted when outer-shell electrons fill a vacancy in the inner K and L shells of an atom [18]. Moseley's work was immediately interpreted in terms of the brand-new Bohr atomic model[2], which predicts that the energy levels of one-electron (hydrogen-like) atoms are given by [19]:

$$E_n = -\frac{\mu c^2 \alpha^2 Z_{\text{eff}}^2}{2n^2} \tag{1.1}$$

where μ is the reduced mass of the electron and nucleus, α is the fine-structure constant, and Z_{eff} is the effective charge, reduced by shielding effects from other electrons:

---

[2] Also published in 1913!

$$Z_{\text{eff}} = Z - \sigma \tag{1.2}$$

Photons emitted in radiative transitions $n_i \to n_f$ have frequency:

$$hv = \Delta E = \frac{\mu c^2 \alpha^2}{2} (Z - \sigma)^2 \left(\frac{1}{n_f^2} - \frac{1}{n_i^2} \right) \tag{1.3}$$

Using $cR_\infty = \frac{m_e c^2 \alpha^2}{2h}$ and $\mu \approx m_e$ for inner shells,

$$\nu \approx cR_\infty (Z - \sigma)^2 \left(\frac{1}{n_f^2} - \frac{1}{n_i^2} \right). \tag{1.4}$$

Taking the square root gives:

$$\sqrt{\nu} = \sqrt{cR_\infty \left(\frac{1}{n_f^2} - \frac{1}{n_i^2} \right)} (Z - \sigma) \equiv A_{n_i \to n_f} (Z - \sigma) \tag{1.5}$$

Thus $\sqrt{\nu}$ vs. Z is a straight line with slope:

$$A_{n_i \to n_f} = \sqrt{cR_\infty \left(\frac{1}{n_f^2} - \frac{1}{n_i^2} \right)} \tag{1.6}$$

indicating that the frequencies of these characteristic X-rays[3] depend on atomic number Z, rather than atomic mass. Prior to Moseley's work, the atomic number had largely been thought to be an index marking the place of each element in the periodic table, and not a physical, measurable quantity [20].

Moseley's Law suggests Z is more fundamental than atomic mass: "We have here a proof that there is in the atom a fundamental quantity, which increases by regular steps as we pass from one element to the next. This quantity can only be the charge on the central positive nucleus, of the existence of which we already have

---

[3] So-called because they differ for each element.

Figure 1.5: Left: Henry Moseley in 1914. He died the following year in the gruesome Battle of Suvla Bay during WWI. Right: Dr. Margaret Todd, medical pioneer and polymath, in 1902. [21, 22]

definite proof [18].” This result allowed Soddy, later that year, to make the inference that the “radioelements” were not just chemically similar to known elements, but were identically those known elements, having the same nuclear charge but different nuclear masses. Soddy’s paper also introduced the word “isotope,” which had been suggested to him by Scottish medical doctor and author Margaret Todd[4], who coined the term by combining the Greek *isos* (same) and *topos* (place), since isotopes are distinct variants of a given element occupying the “same place” on the periodic table [23].

As if this was not enough discovery for one year, J.J. Thomson *also* published a landmark isotope physics paper in 1913, providing the first concrete evidence that

---

[4] One of the first female students to enroll, in 1886, in the Edinburgh School of Medicine for Women.

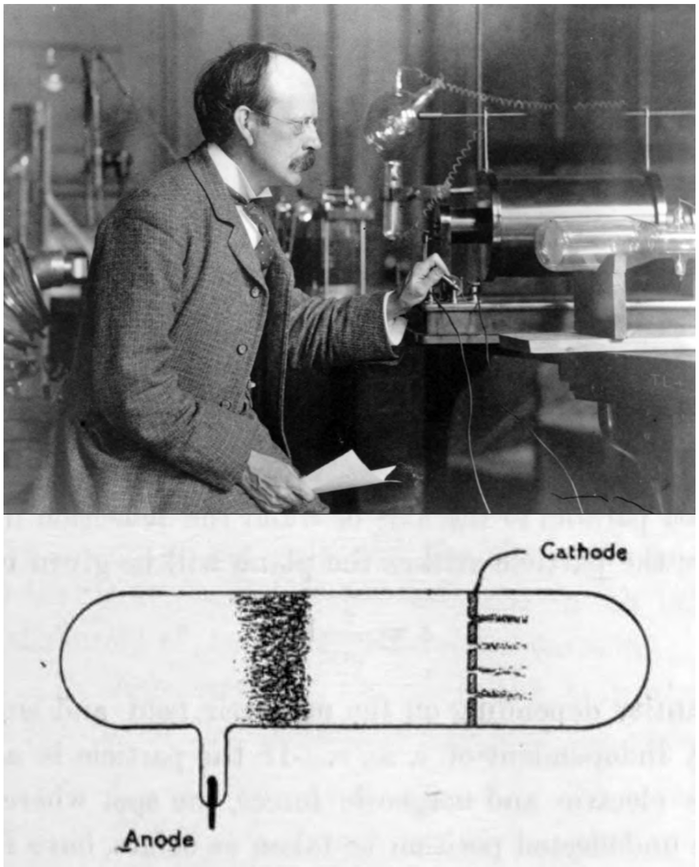

Figure 1.6: Above: J. J. Thomson in 1890. Below: The original illustration of Thomson's apparatus for measuring the mass-to-charge ratio for neon. [24, 25]

isotopes are not limited to the decay products of heavy radioactive elements; isotopes exist for light, stable elements as well. In one of the earliest mass spectrometry experiments, Thomson studied the mass-to-charge ratio of ions formed by a perforated cathode in a neon-filled gas discharge tube [25]. The perforated cathode allowed positive ions to stream through, forming a collimated beam. Near the far end of the tube, the ions were deflected by parallel electric and magnetic fields, striking a photographic plate at the end of the tube, recording their positions. The E-field and B-field induced mutually perpendicular deflections, and all ions of a particular mass-to-charge value lie on a single parabola on the target.

For an ion of charge q and mass m entering the field region with velocity v

along the x-axis, and with the electric and magnetic fields E and B along the y-axis, the small deflection angles acquired are:

$$\theta_E = \frac{qE\ell}{mv^2}, \quad \theta_B = \frac{qB\ell}{mv} \tag{1.7}$$

where ℓ is the length of the field region, and d is the distance from the end of the field region to the photographic plate. To first order, the y-, z- displacements at the plate are given by:

$$y \approx \theta_E\left(d + \frac{\ell}{2}\right) = \frac{qE\ell\left(d + \frac{\ell}{2}\right)}{mv^2}, \quad z \approx \theta_B(d + \ell/2) = \frac{qB\ell(d + \ell/2)}{mv}. \tag{1.8}$$

Eliminating v, Thomson derived the parabolic relation:

$$y = \left[\frac{E}{B^2}\frac{m}{q}\frac{1}{\ell(L + \ell/2)}\right] z^2. \tag{1.9}$$

Hence,

$$y \propto \frac{m}{q} z^2 \tag{1.10}$$

So, all ions of a given m/q fall on the same parabola, regardless of velocity. Neon was then thought to have an atomic mass of 20.2 amu, but Thomson instead saw *two* distinct parabolas: one for $m/q = 20$, and a second parabola for $m/q = 22$. He correctly interpreted this result as evidence that neon consists of a mixture of two isotopes: “There can ... be little doubt that what has been called neon is not a simple gas but a mixture of two gases, one of which has an atomic weight about 20 and the other about 22. The parabola due to the heavier gas is always much fainter than that due to the lighter, so that probably the heavier gas forms only a small percentage of the mixture [25].”

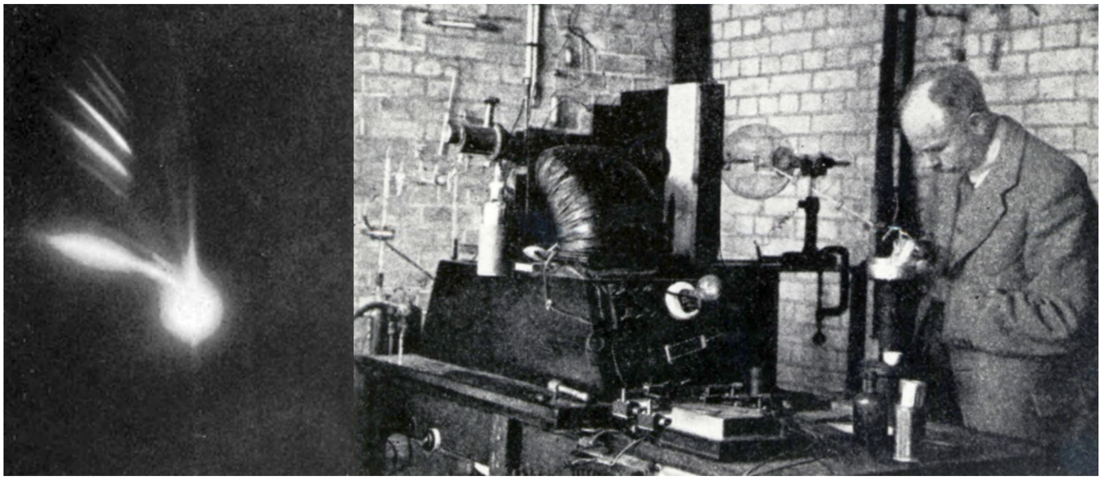

Figure 1.7: Left: Image of the parabolas formed by J. J. Thomson's experiment. The lower parabola is due to helium, and the two bright parabolas due to neon isotopes are visible above. Right: Francis Aston with his mass spectrograph. [25, 26]

Over the following years, Thomson's apparatus was refined into a precision mass spectrograph by his student, Francis W. Aston [27]. By 1920, Aston had catalogued a wide variety of isotopes among the light stable elements, showing that nearly all elements are mixtures of isotopes. including the two naturally occurring isotopes of chlorine, ^{35}Cl and ^{37}Cl, which explained chlorine's notably non-integral atomic weight of roughly 35.5 amu. Aston also identified two isotopes of argon, the six natural isotopes of krypton, and five of the seven natural isotopes of mercury [27, 28].

1.2.2 Biological isotope fractionation

As mass spectrometry continued to advance in sensitivity through the 1920s and 1930s, and was applied to more diverse samples, a new puzzle emerged. Researchers found that materials of biological origin, such as cellulose, proteins, and coal, are significantly enriched in the lighter ^{12}C isotope relative to abiotic sources of carbon like graphite[5], carbonaceous meteorites, and diamond. The first paper to identify this effect, published in 1939 by Alfred Nier and Earl Gulbransen, found a greater than 5% difference in the $^{12}C/^{13}C$ isotope ratio when comparing carbon sampled from plant sources and carbon from nonbiological sources [29]. However, the mechanics of carbon isotope fractionation by living systems were not yet understood.

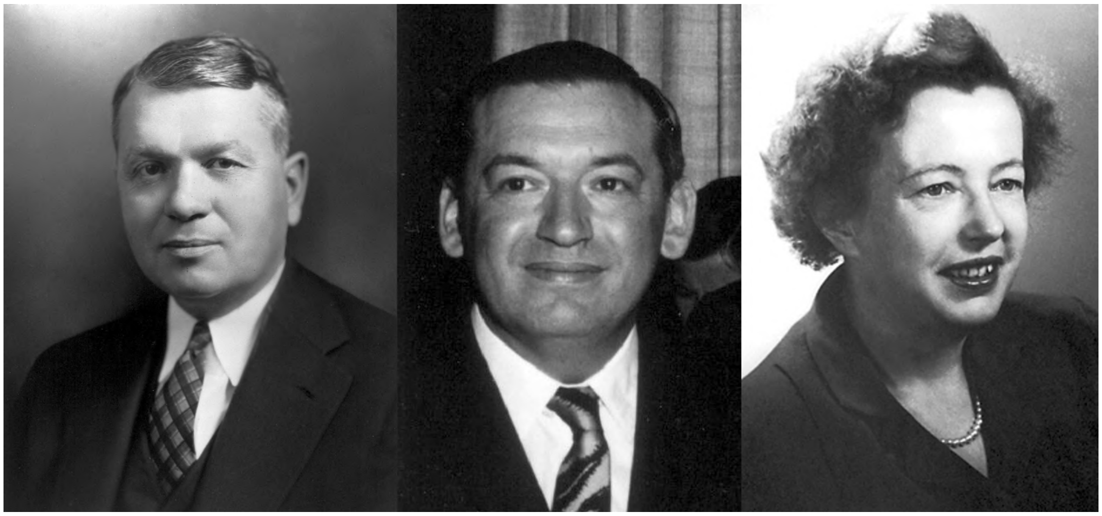

Figure 1.8: Harold Urey, Jacob Bigeleisen, and Maria Goeppert-Mayer. Work by Urey and his collaborators provided the first rigorous explanation for biological isotope effects. [30, 31, 32]

In papers independently published in 1947, Harold Urey[6] and his former Manhattan Project colleagues Jacob Bigeleisen and Maria Goeppert-Mayer gave the first systematic treatment of equilibrium isotope fractionation [33, 34]. They showed that isotopes affect the vibrational energies of chemical bonds due to their mass difference, which slightly alters equilibrium constants and reaction rates. The resulting Urey-Bigeleisen-Mayer (UBM) equation is usually considered the fundamental statistical-mechanical expression for the effect. Here, "equilibrium" means that the isotope

---

[5] Some graphite is of biological origin. Graphite also forms through purely geological processes. The Nier paper considered graphite that was clearly, in hindsight, geological.

[6] American physical chemist, Nobel laureate, and lead scientist for the Manhattan Project's non-electromagnetic isotope separation research.

distribution between two phases or compounds minimizes Gibbs free energy ΔG°, and the ratio of heavy to light isotopes in each phase is determined by thermodynamic equilibrium. This is in distinction to kinetic fractionation, where isotope ratios are shifted because one isotope reacts, diffuses, or escapes faster than the other in a non-equilibrium process such as evaporation.

Urey, Bigeleisen, and Goeppert-Mayer derived how equilibrium isotope fractionation factors depend on temperature and bond strengths, showing that heavier isotopes are preferentially concentrated in compounds with stiffer bonds and higher zero point energies. First, they considered an isotope exchange reaction between molecules A and B [35]:

$$(\mathrm{A-X}) + (\mathrm{B-X^*}) \rightleftharpoons (\ \mathrm{A-X^*}) + (\mathrm{B-X}). \tag{1.11}$$

where the heavier isotope is designated with an asterisk. The macroscopic equilibrium constant is given by:

$$K = \frac{a_{(\mathrm{A-X^*})}\ a_{(\mathrm{B-X})}}{a_{(\mathrm{A-X})}\ a_{(\mathrm{B-X^*})}} = e^{-\Delta G^\circ/RT} \tag{1.12}$$

where each a is the activity, or "effective concentration" of the species. Assuming that the molecules can be approximated as an ideal gas or ideal dilute solution, K can be written in terms of molecular partition functions. The partition functions account for the translational, rotational, vibrational, and electronic states of the molecules, and can be written as the product [34]:

$$q = q_{\mathrm{trans}}\ q_{\mathrm{rot}}\ q_{\mathrm{vib}}\ q_{\mathrm{elec}}\ . \tag{1.13}$$

For an exchange reaction,

$$K = \frac{q_{(\mathrm{A-X^*})}\ q_{(\mathrm{B-X})}}{q_{(\mathrm{A-X})}\ q_{(\mathrm{B-X^*})}} \times e^{-\Delta\varepsilon_0/kT} \tag{1.14}$$

where $\Delta\varepsilon_0$ is the difference in electronic and nuclear ground-state energies. Under the Born-Oppenheimer approximation, the potential-energy surfaces are the same for isotopologues[7], so the only ground-state shift is the vibrational zero-point energy, which is contained in q_{vib} . Thus, $q_{\text{elec},(\mathrm{A-X})} = q_{\text{elec},(\mathrm{A-X^*})}$, and q_{elec} cancels exactly in the exchange equation. For a non-linear molecule,

$$q_{\text{rot}} = \frac{(8\pi^2 kT)^{3/2}}{\sigma h^3} (I_x I_y I_z)^{1/2} . \tag{1.15}$$

The exchange ratio yields a rotational factor

$$\frac{q_{\text{rot},(\mathrm{A-X^*})}\ q_{\text{rot},(\mathrm{B-X})}}{q_{\text{rot},(\mathrm{A-X})}\ q_{\text{rot},(\mathrm{B-X^*})}} = \frac{\sigma_{(\mathrm{A-X})}\ \sigma_{(\mathrm{B-X^*})}}{\sigma_{(\mathrm{A-X^*})}\ \sigma_{(\mathrm{B-X})}} \left[\frac{I_{(\mathrm{A-X^*})}\ I_{(\mathrm{B-X})}}{I_{(\mathrm{A-X})}\ I_{(\mathrm{B-X^*})}}\right]^{1/2} . \tag{1.16}$$

The symmetry numbers σ account for indistinguishable orientations, and often cancel unless isotopic substitution breaks symmetries, such as by making previously equivalent sites distinguishable. The moments of inertia I change on isotopic substitution. For harmonic vibrational modes i with $u_i = h\nu_i/kT$,

$$q_{\text{vib}} = \prod_i \frac{e^{-u_i/2}}{1 - e^{-u_i}}. \tag{1.17}$$

The exchange ratio gives

$$\prod_i \left(\frac{e^{-u_i'/2}}{1 - e^{-u_i'}} \Big/ \frac{e^{-u_i/2}}{1 - e^{-u_i}} \right) = \prod_i \left(\frac{u_i'}{u_i}\right) \exp\left(\frac{u_i - u_i'}{2}\right) \frac{1 - e^{-u_i}}{1 - e^{-u_i'}} \tag{1.18}$$

for each species. The translation term is given by:

$$q_{\text{trans},i} = \frac{V}{\Lambda_i^3}, \quad \Lambda_i = \frac{h}{\sqrt{2\pi m_i kT}} \tag{1.19}$$

the volume term, V, cancels and leaves a mass factor:

---

[7] Molecules with the same chemical formula, but at least one constituent atom being a different isotope.

$$\frac{q_{\mathrm{trans,(A-X^*)}}\ q_{\mathrm{trans,(B-X)}}}{q_{\mathrm{trans,(A-X)}}\ q_{\mathrm{trans,(B-X^*)}}} = \left[\frac{m_{\mathrm{(A-X^*)}}\ m_{\mathrm{(B-X)}}}{m_{\mathrm{(A-X)}}\ m_{\mathrm{(B-X^*)}}}\right]^{3/2} \tag{1.20}$$

This factor can be shown to exactly cancel using what is known as the Teller-Redlich product rule, which is a mass-invariance identity for molecules under the rigid-rotor/harmonic oscillator (RRHO) and Born-Oppenheimer approximations [36]. Specifically, it says that for nonlinear molecules with N atoms, vibrational frequencies $\{\nu_i\}_{i=1}^{3N-6}$, and principal moments of inertia I_A, I_B, I_C, the quantity

$$\left(\prod_{i=1}^{3N-6} \nu_i\right) \frac{(I_A I_B I_C)^{1/2}}{M^{3/2}} \tag{1.21}$$

is constant under isotopic substitution. The remaining translation term cancels with part of the rotational/vibrational terms, and surviving terms yield the reduced partition function ratio, which is usually written as β:

$$\beta = \frac{\sigma}{\sigma'}\left(\frac{I}{I'}\right)^{1/2} \prod_i \left(\frac{u_i'}{u_i}\right) \exp\left(\frac{u_i - u_i'}{2}\right) \frac{1-e^{-u_i}}{1-e^{-u_i'}} \tag{1.22}$$

For two phases or molecular sites A and B that exchange the same element, the equilibrium fractionation factor is

$$\alpha_{(A-B)} = \frac{\beta_A}{\beta_B}. \tag{1.23}$$

In the high temperature limit, $u \ll 1$. Rewriting the above as $\ln \alpha_{\mathrm{(A-B)}} = (\ln \beta_A - \ln \beta_B)$, and using the Bernoulli expansion:

$$\ln \beta = \sum_{n=1}^{\infty} \frac{B_{2n}}{2n(2n)!} \sum_i \left(u_i^{2n} - u_i'^{2n}\right) \Rightarrow \ln \beta \approx \frac{A}{T^2} + \frac{B}{T^4} + \cdots \tag{1.24}$$

where the B_{2n} are Bernoulli numbers. Hence, isotope fractionation scales as $\propto 1/T^2$; fractionation increases approximately quadratically as temperature is decreased.

The role of bond strength in equilibrium isotope fractionation can also be inferred from Eq.1.24. Heavier isotopes result in lower bond vibrational frequencies than lighter isotopes, since $\nu \propto \sqrt{k/\mu}$. Remembering that $u_i = h\nu_i/kT$, it follows that $u_i > u'_i$. For two sites A and B, if the bond in site A is stiffer ($k_A > k_B$), then $\ln \beta_A > \ln \beta_B$ and $\alpha_{(A-B)} > 1$. Hence, at equilibrium, site A ends up enriched in the heavier isotope. As mentioned at the the beginning of this section, the UBM framework is applicable to processes at equilibrium; for reversible and near-reversible biological systems, the isotope fractionation values will tend to those predicted by Eq. 1.24. However, nearly unidirectional, driven processes are common in biological systems, such as diffusion across membranes, active transport, and enzyme-catalyzed reactions; these processes involve what are called kinetic, or rate effects. Lighter isotopes tend to be favored in directed processes, because they react or are transported slightly more rapidly than the heavier isotopes, resulting in fractionation [37].

In fact, the biological fractionation of carbon isotopes discussed earlier is primarily due to a kinetic isotope effect. Most carbon enters the Earth's biosphere via fixation of CO_2 by the enzyme RuBisCO[8], a crucial enzyme in photosynthesis. The reaction driven by RuBisCO discriminates in favor of $^{12}CO_2$ by as much as 0.3% [38]. This process systematically enriches biological systems in ^{12}C compared to abiotic carbon. Carbon isotope fractionation due to photosynthesis has been used to estimate past atmospheric CO_2 levels by measuring the carbon isotope ratios of fossils [39, 40].

1.2.3 Biological fractionation: diagnostic marker of disease

Biological isotope fractionation can serve as a sensitive diagnostic marker for a variety of serious disease conditions; detecting and monitoring alterations in the normal ratio of stable isotopes in the body is a promising avenue for the development of new methods of early disease diagnosis that could be incorporated into routine

---

[8] Ribulose-1,5-bisphosphate carboxylase/oxygenase.

disease screening. Achieving this goal will require significant advancements in affordable, scalable isotope ratio analysis methods. Some examples of disease-related isotope fractionation with substantial medical and scientific interest are outlined here.

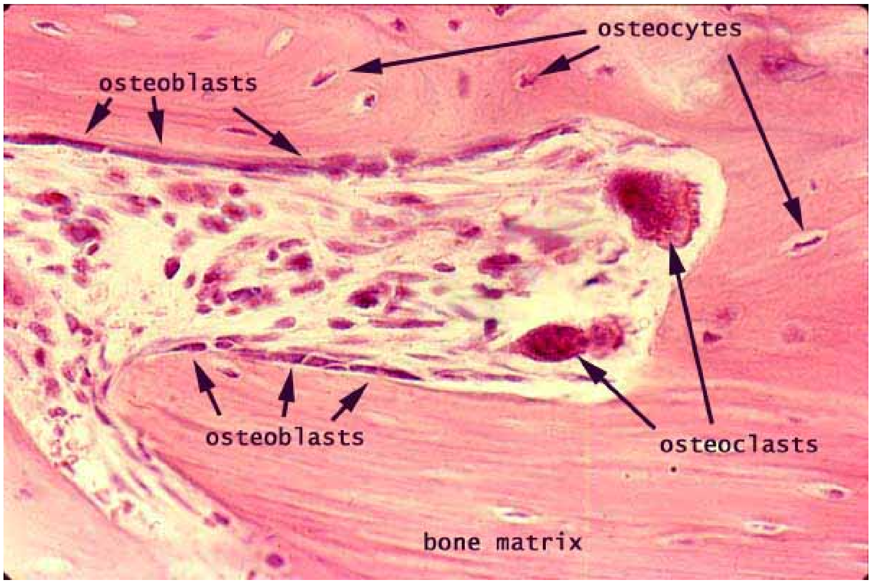

Figure 1.9: Osteoblasts and osteoclasts in developing bone (400× magnification) [41].

Calcium has five naturally occurring stable isotopes: ^{40}Ca, ^{42}Ca, ^{43}Ca, ^{44}Ca, and ^{46}Ca [9]. In healthy adults, about 99% of the body's calcium resides in bone, mostly as the hard mineral hydroxyapatite[10] [42]. There is a continual daily exchange of roughly 500 mg of calcium between bone and extracellular fluid, a dynamic equilibrium maintained by specialized cells [43]. Osteoblasts are cells that specialize in the formation of new bone. They form hydroxyapatite by pulling phosphate and Ca^{2+} ions from the extracellular fluid and concentrating it in matrix vesicles, small membrane-bound sacs that bud off the osteoblasts' plasma membranes [44]. Hydroxyapatite crystals are nucleated inside the matrix vesicles, and the subsequent crystal growth is spatially guided by collagen fibrils, which have a triple helix structure and

---

[9] The isotopes ^{42}Ca and ^{44}Ca have abundances of $\sim 0.6\%$ and $\sim 2.1\%$, respectively.

[10] $Ca_{10}(PO_4)_6(OH)_2$.

periodic gap zones at 40 nm intervals. Hydroxyapatite crystal growth is guided along the fibril axis inside these gaps [45, 46].

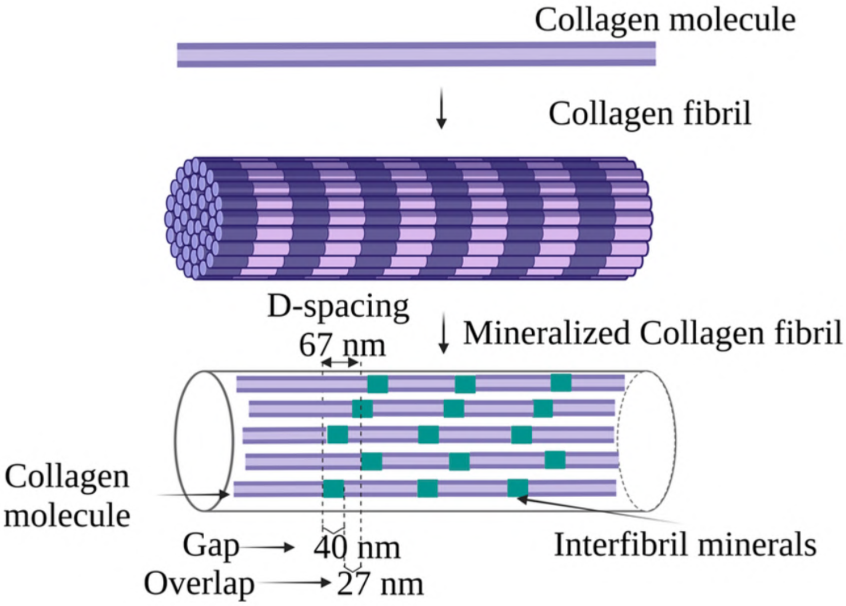

Figure 1.10: Structural hierarchy of collagen. Figure credit:[46]

The crystal nucleation process preferentially incorporates the lighter ^{42}Ca isotope into hydroxyapatite, leaving the blood and urine slightly enriched in the heavier ^{44}Ca isotope [47]. It has been suggested that because the Ca^{2+} ions can move freely and compete for sites in the growing crystals, kinetic isotope fractionation is responsible [48]. In healthy individuals, the degree of biological isotope fractionation between bone and blood serum is approximately $\Delta^{44/42}\text{Ca} = \delta^{44/42}\text{Ca}_{\text{bone}} - \delta^{44/42}\text{Ca}_{\text{serum}} \approx -0.03\%$ [49]. The delta notation indicates:

$$\delta^{44/42}\text{Ca} = \left(\frac{(^{44}\text{Ca}/^{42}\text{Ca})_{\text{sample}}}{(^{44}\text{Ca}/^{42}\text{Ca})_{\text{standard}}} - 1 \right) \times (100\%). \tag{1.25}$$

Because bone apatite is enriched in the lighter ^{42}Ca isotope relative to ^{44}Ca, when osteoclast cells break bone down again, greater quantities of the lighter calcium isotope are released back into circulation in the body, producing a measurable shift in the blood and urine calcium isotope ratios [50]. In people suffering from osteoporosis, a disease which causes harmful levels of bone loss, the $\delta^{44/42}$Ca isotope ratio can shift by roughly 0.015%, a nearly 20% change relative to the isotope ratio for healthy people [49]. Calcium isotope ratio shifts could serve as a nearly real-time, non-invasive biomarker for bone loss, with greater sensitivity to the onset of osteoporosis than other biomarkers; bone loss can be detected in calcium isotope data around one week after the onset of net bone loss, and long before changes are detectable via bone mineral density imaging[11] [51]. Additionally, calcium isotope ratio measurement has the immensely attractive feature of being useful for screening well before invasive procedures like bone biopsy would be considered clinically advisable.

Cancer is another disease for which stable isotope ratio measurement has promising diagnostic applications. Copper is an essential trace nutrient involved in a variety of critical cellular tasks, including cell proliferation and angiogenesis[12] [52]. Consequently, many tumors overexpress a variety of copper-containing enzymes with strong binding sites [53]. The Urey-Bigeleisen-Mayer equation predicts that heavier isotopes concentrate in molecules with stronger bonds[13]. This hints that tumor microenvironments, with their abundant strong copper binding sites, are likely to be enriched in ^{65}Cu, the heavier of the two naturally occurring copper isotopes. Direct measurements confirm that tumor tissue is indeed ^{65}Cu-enriched [53].

In comparison to healthy controls, people with many types of cancer, especially liver, breast, and hematologic cancers, have blood plasma relatively enriched in lighter ^{63}Cu. Reported δ^{65}Cu shifts are often -0.03% to -0.1% relative to healthy controls; the degree of shift correlates with tumor type and progression. A longitudinal study of breast and colorectal cancer reported that patients with serum δ^{65}Cu below -0.035% had poorer survival rates, and that a drop in δ^{65}Cu preceded molecular biomarkers by months [54]. However, liver diseases such as liver fibrosis can also

---

[11] Typically, dual-energy X-ray absorptiometry (DEXA) scans.

[12] The formation of new blood vessels.

[13] See Section 1.2.2.

strongly influence serum δ^{65}Cu, so clinical use will likely require pairing δ^{65}Cu with liver function assessment [55].

Breast cancer tissue has been demonstrated to sequester lighter zinc isotopes relative to healthy tissue[14]. One study measured δ^{66}Zn shifted ratio values for breast cancer tumors as -0.06 to -0.09%, compared to healthy breast tissue with δ^{66}Zn of -0.03 to -0.05%, indicating a tumor-specific sink for light zinc isotopes [56]. Mechanistically, metallothionein (MT), a small, cysteine-rich protein that plays important roles in detoxifying toxic metals and storing essential metals, is believed to be responsible for sequestering light zinc isotopes. Lighter isotopes are favored in cysteine sites, and MT overexpression in tumors therefore drives isotopically light tissue signatures [56]. In pancreatic and prostate cancers, urine samples have been observed to become relatively enriched in lighter ^{64}Zn versus healthy controls. The degree of light isotope enrichment was found to consistently track risk category[15], suggesting urinary δ^{66}Zn isotope ratios may provide a non-invasive diagnostic for pancreatic cancer, and a prognostic support for prostate cancer [57].

Compared with controls, blood cancer patients are found to have significantly higher δ^{66}Zn in their blood plasma. The zinc isotope ratio predicted patient survival even after accounting for other known risk factors: the group of subjects with a combination of increased δ^{66}Zn and decreased δ^{65}Cu was associated with an almost quadrupled risk of death within 5 years [58]. Additionally, the zinc and copper isotope ratios in the brain tissue of Alzheimer's patients differs significantly from that of controls, and varies systematically with Braak stage[16], consistent with zinc's involvement in amyloid/tau[17] pathology. Interestingly, the effects are in opposite directions: δ^{65}Cu is found to be lighter by -0.02% to -0.03%, while δ^{66}Zn is heavier by 0.02%

---

[14] Zinc has five stable isotopes, with ^{64}Zn and ^{66}Zn being the most abundant.

[15] Low/intermediate/high risk, based on clinical criteria including PSA levels and Gleason scores.

[16] The classification system for degree of pathology in Alzheimer's disease.

[17] Two proteins involved in brain function that misfold and clump together in Alzheimer's disease, damaging neurons.

to +0.03% [59]. The isotopic excursions are interpreted as consequences of altered bonding environments for zinc as plaques and tangles accrue, suggesting a potential means to improve Alzheimer's staging and monitoring methods if these isotope shifts in brain tissue can be correlated with a more accessible metric, such as isotope shifts in cerebrospinal fluid (CSF).

1.2.4 Rare isotopes as metabolic tracers

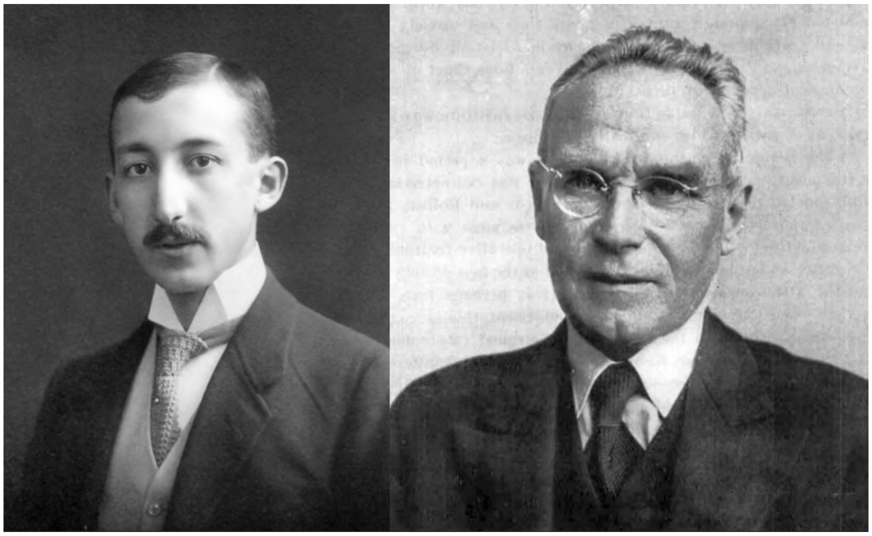

Figure 1.11: Left: George de Hevesy in 1913. Right: Ole Chievitz. [60]

The practical use of isotopes as tracers was pioneered by Hungarian physicist and radiochemist George de Hevesy in 1911, two full years before the *annus mirabilis* of 1913 fully established what isotopes actually *are*. His subsequent work on isotope tracers laid the groundwork for an experimental method with a transformative impact in chemistry, physiology, and medicine[18]. In chemistry, isotopic tracer methods permit measurement of equilibrium constants and reaction rates in trace concentrations; in biology and medicine, isotopes enable the mapping of metabolic pathways and

---

[18] de Hevesy received the 1943 Nobel Prize in Chemistry "for his work on the use of isotopes as tracers."

nutrient cycles. Isotope tracer methods also underpin both diagnostic nuclear imaging and radiotherapy dosimetry.

In 1911, de Hevesy arrived at the University of Manchester to work in Ernest Rutherford's laboratory as a postdoctoral researcher. There, he was tasked with isolating "radium D," a decay product of uranium which we now know to be a radioisotope of lead, ^{210}Pb. de Hevesy would later recall Rutherford cheerfully setting an experimental challenge: "My boy, if you are worth your salt, you separate radium D from all that nuisance lead [61]." The separation of one lead isotope from another was, of course, impossible by any means available at the time; after a year of strenuous effort, de Hevesy finally gave up. To make the best of this "depressing situation," as he later put it, de Hevesy considered whether the chemical inseparability of lead and radium D could be put to good use: "I thought to avail myself of the fact that radium D is inseparable from lead and to label small amounts of lead by addition of radium D of known activity [61]."

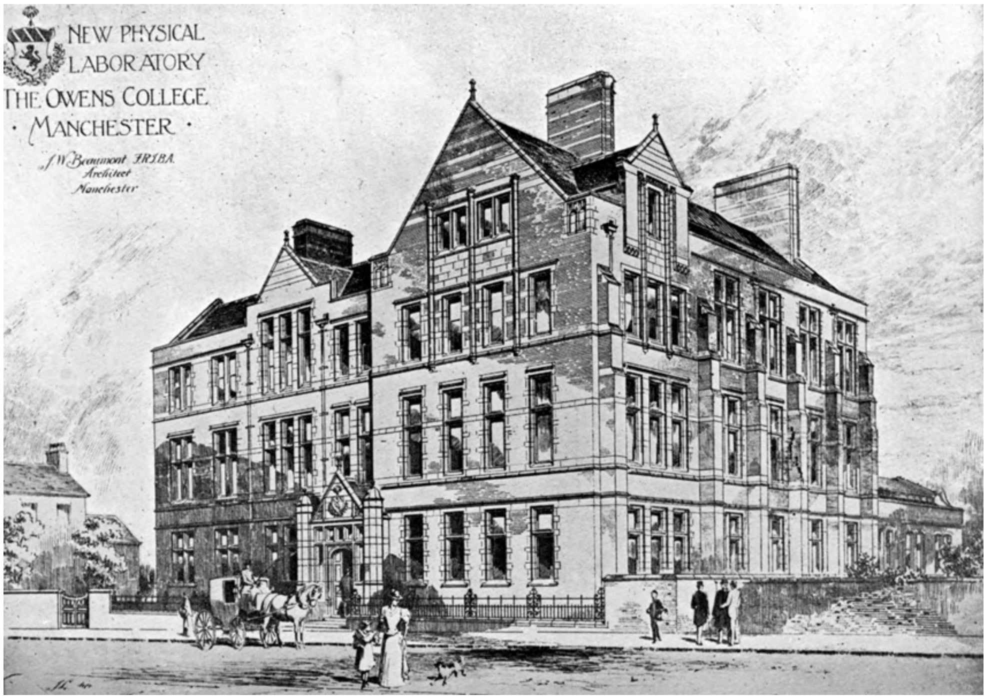

Figure 1.12: 1906 image of Rutherford's laboratory building at Manchester [62].

There is a famous story told by de Hevesy about his first experimental use of isotope tracers. During his time working in Rutherford's Manchester laboratory, the renters at the boarding house where he lived suspected their landlady of recycling leftovers from previous meals into stew for meals later in the week. To prove this, de Hevesy secretly added a tiny quantity of radium D from the laboratory to the leftovers at the end of a meal. When a stew with suspiciously familiar-looking ingredients appeared the next day, he tested it with an electroscope. The radioactive signature of radium D provided clear experimental evidence that their suspicions had been well-founded [60]! de Hevesy realized that the chemically identical isotopes of an element could serve as "labels" to trace atoms through complex systems with negligible disturbance to the systems; he termed this the "method of isotopic indicators [63]". For example, because radium D "can be detected in incomparably smaller amounts than lead, it can thus serve as a qualitative and quantitative proof [of the presence] of lead to which it was added: RaD becomes an indicator of lead [64]."

The 1934 discovery by Frédéric and Irène Joliot-Curie that radioisotopes could be artificially produced by α-particle bombardment provided a crucial means of producing radioisotopes of biomedical interest such as phosphorus, carbon, nitrogen, and oxygen [65]. In 1935, de Hevesy collaborated with Ole Chievitz, a Danish anatomist and surgeon at the University of Copenhagen[19], on an experiment that provided the first clear demonstration that isotopes can quantitatively trace metabolic pathways in living organisms. Their research was designed to test whether ^{32}P, a β-emitter with a two-week half-life, could follow phosphate metabolism *in vivo* [66]. Initially, de Hevesy produced their samples of ^{32}P by neutron bombardment of sulfur, most likely using a radon-beryllium neutron source [67]. However, the yields of ^{32}P from this method are very low, and subsequent samples were supplied by Martin Kamen

---

[19] Chievitz was deeply involved in the Danish Resistance during World War II, coordinating the clandestine transport of supplies concealed within deliveries for the University of Cophenhagen's anatomy department, and was a member of the covert Danish Freedom Council. Arrested and imprisoned by the Gestapo in 1944, he died in 1946, reportedly from health complications attributable to his wartime incarceration.

in Ernest Lawrence's cyclotron group at the University of California (UC) Berkeley [67]. The test subjects were living rats, to whom the tracer was administered intravenously or orally as minute quantities of ^{32}P orthophosphate. The ^{32}P decay signal was measured using Geiger-Müller counters and ashed tissue samples, allowing a determination of the rate of phosphorus exchange between blood plasma, soft tissues, and bone.

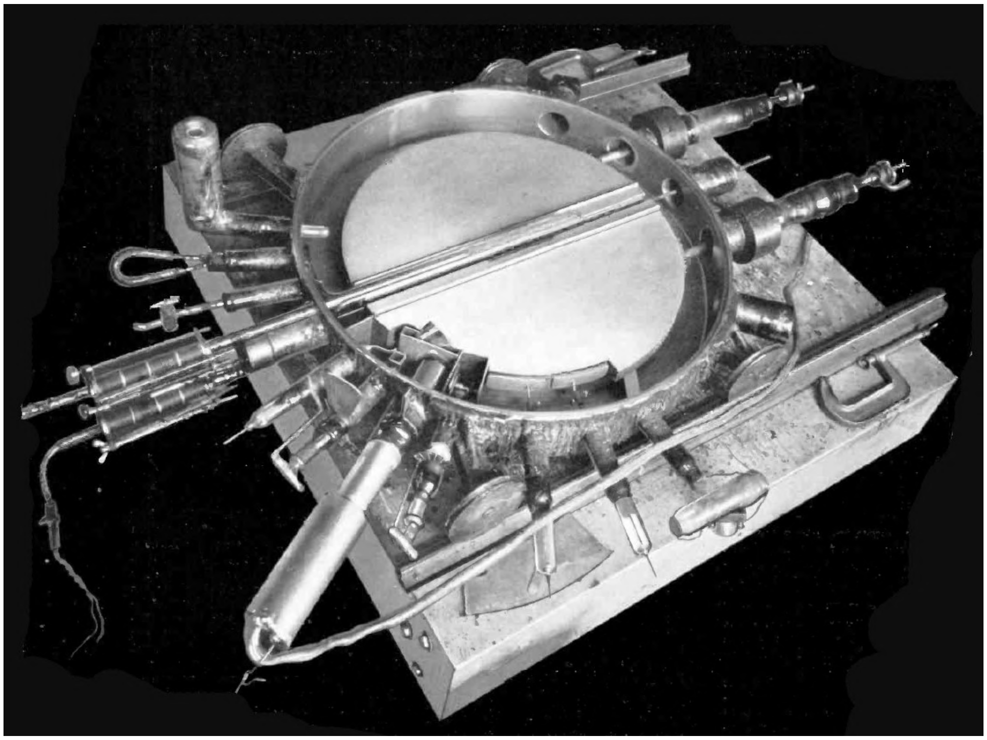

Figure 1.13: The 27″ Berkeley cyclotron in 1935 [68].

Chievitz and de Hevesy found that within hours, ^{32}P appeared in virtually all organs, particularly the kidneys and liver. This strongly suggested an active exchange process. They were also able to determine the biological half-times[20] for phosphate in different tissues. Soft-tissue phosphate is exchanged within hours to days, while bone phosphate is exchanged more slowly, over weeks: "the formation of bones is a

---

[20] The time required for half of a given quantity to be eliminated from a biological system.

dynamic process, the bone continuously taking up phosphorus atoms which are partly or wholly lost again, and are replaced by other phosphorus atoms. In the case of an adult rat, about 30% of the phosphorus atoms deposited in the skeleton were removed in the course of twenty days [66]."

Meanwhile, at UC Berkeley, physician John Lawrence[21] and his colleague Joseph Hamilton had become interested in using isotope tracing as a method to study electrolyte turnover in the human body. Two years after de Hevesy and Chievitz published their ^{32}P tracer experiment on rats, the Berkeley group extended this work by carrying out, arguably, the first demonstrations of isotope tracers in human metabolism [69, 70, 71]. ^{24}Na, a pure β-emitter with an experimentally convenient 15-hour half-life, was chosen as the tracer isotope. The samples of ^{24}Na were produced by deuteron bombardment of crystalline NaCl in the cyclotron constructed by Ernest Lawrence and his group at the nearby UC Berkeley Radiation Laboratory [71].

The experiments involved the intravenous injection of $80 - 200$ μCi doses of ^{24}NaCl into test subjects, who were hospital patients and healthy volunteers. Detection of the tracer was performed by a combination of external whole-body counts, as well as measurements from blood and urine samples. Whole-body counts were estimated using a special apparatus, consisting of a Geiger-Müller counter inside a lead box fitted over the hand and forearm. Measured activity served as an indicator of systemic ^{24}Na absorption. Within a year, Hamilton extended this tracer approach for studying electrolyte metabolism to potassium, chlorine, bromine, and iodine in healthy subjects [72].

In the 1930s to 1950s, cyclotron-produced isotopes, including the iron radioisotopes ^{59}Fe and ^{55}Fe, served as tracers for a wide range of clinical and metabolic

---

[21] Younger brother of Ernest Lawrence! In 1936, he founded UC Berkeley's Donner Laboratory, the world's first institute devoted to medical applications of nuclear science. It is often regarded as the birthplace of nuclear medicine.

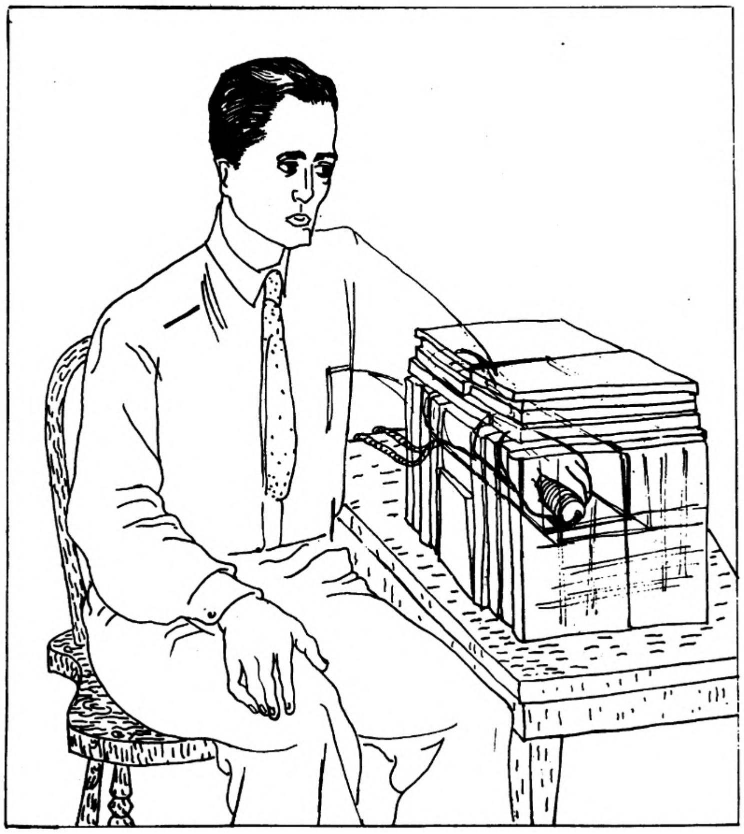

Figure 1.14: Illustration of the apparatus used by the Berkeley group for whole-body counts [71]. It is interesting to consider how the visual language of science communication has varied over time.

studies, marking the beginning of modern hematology and iron metabolism research [73, 74, 75]. Studies used radioactive iron to quantify a variety of medically significant processes, including the biological half-time of iron in plasma, the turnover rate of red blood cells, and direct confirmation that human iron metabolism is a closed cycle, without a direct excretory mechanism. The use of iron isotope tracers to label red blood cells, a crucial technique for later studies, was pioneered in 1941 by researchers at the University of Rochester [76]. The following year, the Rochester group quantified iron absorption in both healthy subjects and in those who are pregnant, anemic, or have hemochromatosis[22]: subjects overloaded with iron had very little iron uptake, while those with anemia had the highest uptake, suggesting that iron absorption is affected by physiological needs [77]. One of the earliest population nutrition studies measured the absorption of orally administered radioactive iron in schoolchildren in 1947 [78]. In the 1950s and 1960s, the US Public Health Service, the University of Wisconsin, and Harvard University conducted landmark studies in pediatric nutrition using radioactive ^{55}Fe and ^{59}Fe. This work directly led to an understanding of the variability of iron absorption depending on iron status, diet, and age. It also was instrumental in setting daily iron intake requirements for infants and small children [79, 80, 81].

However, a cavalier approach to risk and patient consent in isotope tracer research during this period resulted in notorious and sometimes absurd case studies in unethical research practices, such as a 1949 study funded by the Quaker Oats Corporation and the Atomic Energy Comission, in which unsuspecting boys who joined the "science club" of a Masachusetts institution for developmentally disabled children were fed oatmeal dosed with ^{55}Fe and ^{59}Fe, with the major goal being to demonstrate that Quaker Oats oatmeal is as nutritious a source of dietary iron as its direct competitor, Cream of Wheat [81, 82, 83]. This incident, and others like it, were re-evaluated by the Advisory Committee on Human Radiation Experiments (ACHRE) in 1995 [84]. The ACHRE review highlighted prenatal and pediatric exposures lacking direct medical benefit; this helped to establish the current principle that ionizing tracers should not be administered to children unless absolutely medically necessary, and no other viable options are available. In the late 1980s to 1990s, the wider availability of mass spectrometry allowed stable isotope tracers to replace the use of radioisotopes in most metabolic studies, particularly those involving children [85, 86, 87].

---

[22] A genetic disorder in which the body absorbs and stores excessive quantities of iron.

1.3 Iron and iron deficiency

Iron is one of the most essential trace elements in human nutrition, playing a critical role in a wide range of processes, including oxygen transport, immune response, neurotransmitter synthesis and brain function, as well as DNA synthesis and repair. It is also one of the most functionally versatile trace elements in biology, partly due to its ability to readily interconvert between Fe^{2+} (ferrous) and Fe^{3+} (ferric) oxidation states, and partly because it can be incorporated into biological cofactors with many different geometries, electronic properties, and reactivities. Some representative examples of iron's multifaceted biological role are briefly outlined in this section.

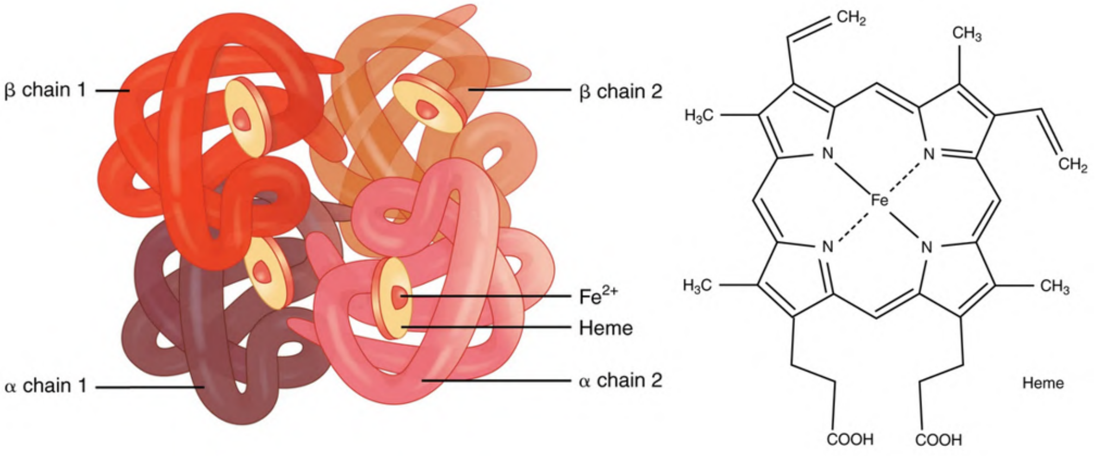

Figure 1.15: Structure of hemoglobin molecule [88].

Each molecule of hemoglobin has four heme groups, with a central Fe^{2+} ion that binds oxygen reversibly, allowing efficient oxygen uptake in the lungs and delivery to tissues[89]. Iron is embedded in several crucial cofactors of the mitochondrial electron transport chain (ETC), which are critical to the oxidative steps by which mitochondria produce ATP, the energy-carrying molecule present in all known forms of life [89]. Iron acts as a catalytic cofactor in many enzymes across metabolic pathways; for example, catalase and peroxidases decompose hydrogen peroxide molecules, protecting cells from oxidative damage [89]; cytochrome P450 enzymes are involved in steroid synthesis, drug detoxification, and fatty acid metabolism[90]; ribonucleotide reductase (RNR) is an iron-dependent enzyme that generates deoxyribonucleotides from ribonucleotides, the rate-limiting step in DNA synthesis [91]. Iron is thus critical for cell division, growth, and tissue repair.

Iron is also central to the immune response process known as oxidative burst, in which macrophages produce reactive oxygen species (ROS) to kill engulfed pathogens such as bacteria and fungi [92]. In a process called nutritional immunity, the body attempts to withhold iron from pathogens. During infection, iron is sequestered by proteins such as lactoferrin and transferrin, while hepcidin increases to reduce iron export, starving pathogens of iron [93]. Iron is an essential cofactor in the biosynthesis of key neurotransmitters: dopamine, norepinephrine, and serotonin require Fe^{2+} cofactors. Iron deficiency can result in reduced dopamine and serotonin levels, contributing to cognitive impairment, movement disorders, and mood disturbances [94].

Plainly, the role of iron is not confined to a single metabolic pathway: it is simultaneously an oxygen carrier, energy mediator, catalytic cofactor, DNA synthesis enabler, immune system effector, and signaling regulator. This variety of roles helps explain why iron deficiency can cause such wide-ranging symptoms[23], and why iron overload leads to multisystem damage, including organ failure.

1.3.1 Effects of pediatric iron deficiency

Iron deficiency in childhood has wide-ranging physiological, developmental, and cognitive consequences. Because iron is central to oxygen transport, energy metabolism, neurotransmitter function, and DNA synthesis, iron deficiency during periods of rapid growth, such as infancy and early childhood, can have especially negative effects. The most vulnerable period occurs in the first 1000 days from conception through the second year of life, when iron deficiency can cause permanent

---

[23] Fatigue, immune weakness, impaired cognition, and developmental delays, among others.

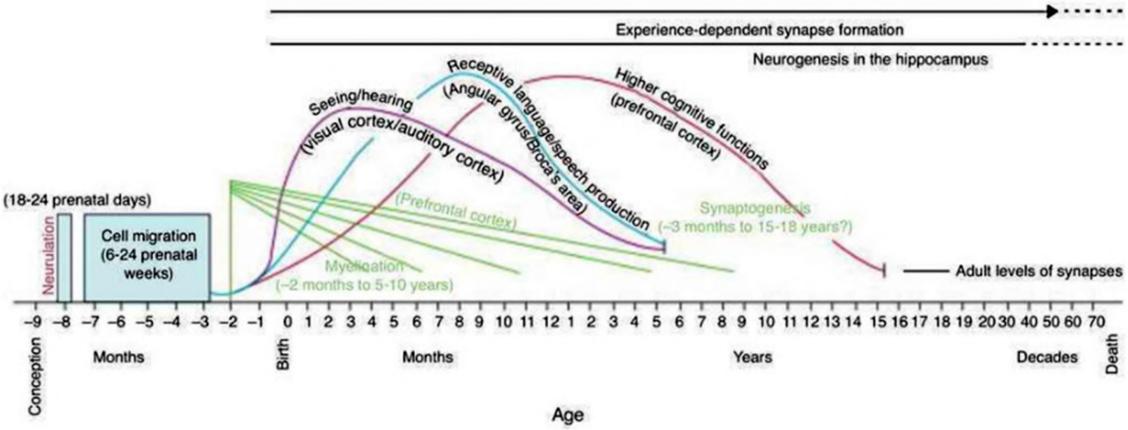

Figure 1.16: Timeline of neurological development. Note the clustering of critical processes during the first 1000 days of life. Image credit: [95].

alterations in brain structure and function. The effects of iron deficiency in later childhood and adolescence are more reversible, though persistent learning difficulties may result if early deficiency is untreated [96, 97]. Children with chronic iron deficiency often have lower height-for-age and weight-for-age z-scores. This reflects the reduced energy available for growth due to impaired oxygen delivery, and limited cell division in cartilage and bone growth plates [98]. Catch-up growth is possible with iron supplementation, but the treatment effectiveness depends on when the deficit occurred. Individuals whose iron deficits occurred during the critical growth window from early infancy to toddlerhood are less likely to have fully normalized growth.

Sitting, crawling, standing, and walking often occur later in iron-deficient infants. This is because iron is a cofactor for enzymes involved in the process of nerve myelination, where oligodendrocytes in the central nervous system and Schwann cells in the peripheral nervous system wrap nerve axons with myelin, which is a lipid sheath that enables rapid and efficient nerve impulse conduction. Iron is indispensable for proper brain maturation, especially during the first two years of life, when myelination, synaptogenesis, and neurotransmitter regulation are at their peak [99]. Early iron shortages can cause structural and functional alterations that may not be fully reversible: infants with iron deficiency anemia show altered white matter structure on MRIs, as well as deficits in tests of cognitive, motor, and social development [100]. Structural and functional changes occur in the hippocampus, a brain region governing learning, memory, and spatial processing, and which has particularly high iron demand. Animal models show reduced dendritic branching and synaptic plasticity [101]. Even if the iron deficiency is treated later on, these impairments may not be fully reversed: studies following up with anemic infants more than 10 years later continued to show worse school performance and motor coordination, despite normalization of hemoglobin [102].

1.3.2 Iron deficiency and public health

Iron deficiency is the world's most prevalent nutritional disorder, affecting populations in both developed and developing countries. Its public health impact spans growth and cognitive development, productivity, pregnancy outcomes, and infection susceptibility, making it a major contributor to the global burden of disease. The World Health Organization (WHO) estimates that more than 30% of the global population suffers from anemia, and about half of these cases are due to the more severe iron deficiency (IDA) [103]. Worldwide, around two billion people are affected by anemia, including nearly one-third all women of reproductive age and children younger than 5 years old [103, 104]. When including individuals with low iron levels who are not yet anemic, the total number affected likely exceeds three billion people. Though iron deficiency affects every country and socioeconomic group, its severity and causes differ between high-income and low-income regions. Regional inequality is stark: the prevalence of anemia in sub-Saharan Africa is roughly five times that in North America.

The greatest absolute burden of iron deficiency is in South Asia due to its high population density; India alone accounts for nearly one-quarter of global IDA cases. Around 40% of South Asian women of reproductive age[24] and 50% of children are

---

[24] Aged 15-49, for the purposes of WHO-reported statistics.

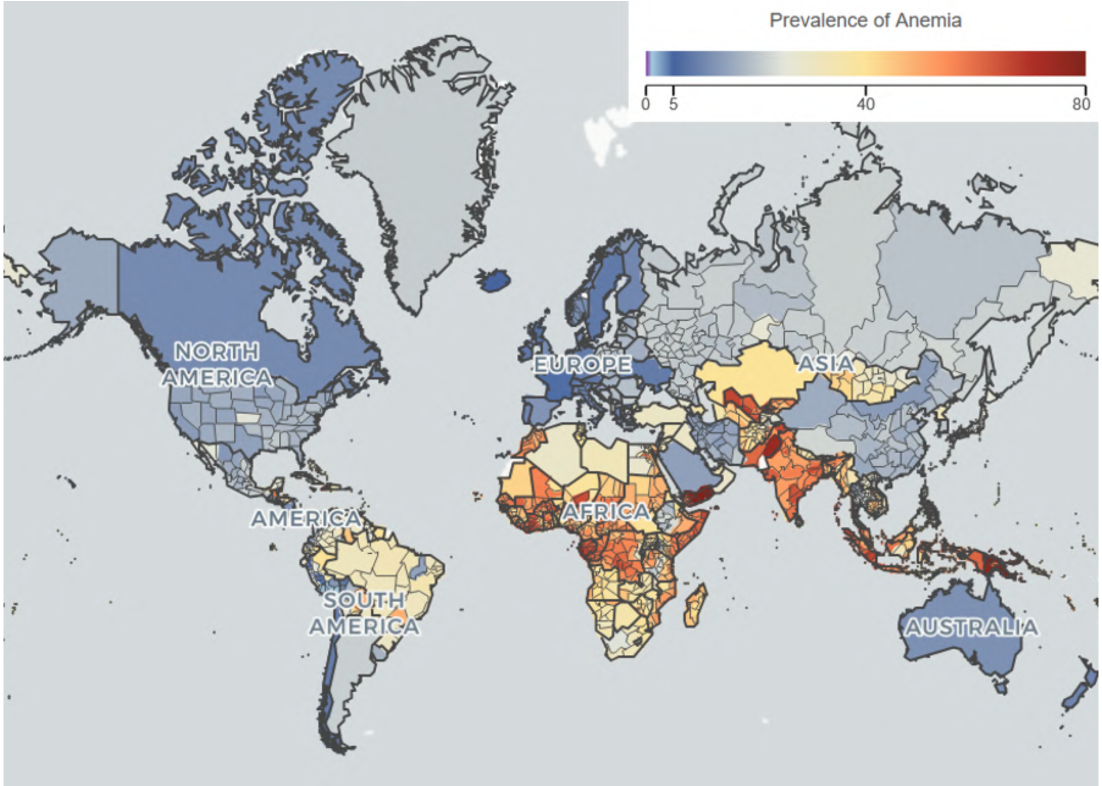

Figure 1.17: Global anemia prevalence (%) for women aged 15-49 in 2019. [105].

affected by anemia. The highest global prevalence of anemia is in sub-Saharan Africa, where about 55% of women of reproductive age and 60% of preschool children are anemic. The prevalence of anemia in high-income nations is comparatively low, around $8 - 12\%$ of women and less than 5% of children. However, iron deficiency without anemia is still common, affecting up to 25% of women of reproductive age and 10% of toddlers. Even in a high-income nation like the United States, anemia disproportionately affects low-income and economically marginalized populations, reflecting deep nutritional and health-care inequities. About 15% of low income[25] American children and 18% of low-income women are anemic, roughly twice the incidence among higher-income Americans [106, 107].

---

[25] Defined as $\leq 130\%$ of the federal poverty level.

Iron deficiency is also tremendously economically costly [108]. The WHO and World Bank identify iron deficiency among the top ten causes of global disability and a major barrier to achieving Sustainable Development Goals (SDGs) related to education, gender equality, and economic development [109]. Economic losses are estimated at 2-3% of GDP in the worst-affected low- and middle-income countries (LMICs) [110]. Globally, the annual economic cost is estimated at roughly $\$70-\$90$ billion (USD) in lost productivity and health expenditure. Iron deficiency reduces hemoglobin concentration, limiting oxygen delivery to muscles and impairing endurance. For economies reliant on physical labor in agriculture and manufacturing, the macroeconomic impact can be significant. One study of iron-deficient Sri Lankan rubber-plantation workers showed $10-20\%$ lower physical work output compared with their non-iron-deficient peers. Iron therapy significantly improved endurance and productivity [111].

As discussed in the previous section, iron deficiency in infancy and early childhood impairs myelination, synaptic pruning, and neurotransmitter metabolism. These effects translate into poorer school performance, and lower educational attainment, reducing lifetime earnings and national human capital. Iron-deficiency anemia increases the risk of preterm birth, low birth weight, and maternal mortality. One study has estimated that in LMICs, 19% of preterm births, 12% of low birth-weight births, and 18% of maternal deaths in the weeks before and after birth are attributable to maternal anemia [112].

1.3.3 Bioavailability studies

For these reasons, preventing iron deficiency is of great interest to both clinical physicians and those concerned with public health, particularly in LMICs. Although iron is abundant in nature, it can be difficult to absorb from food, especially for young children. This makes the use of iron fortificants a critical part of a strategy to address iron deficiency. Fortification of flour, rice, or salt with iron is one of the most cost-effective public-health interventions known, with studies finding a cost-benefit ratio between $1:6$ and $1:35$, meaning every dollar spent yields up to \$35 in economic benefit [108]. For example, flour fortification programs in some Latin American countries, such as Venezuela, significantly reduced anemia incidence at a cost of around \$0.12 (USD) per person per year [113].

Many different iron fortificants are available, including ferrous salts and molecular complexes such as iron polymaltose. Unfortunately, the bioavailability of a given fortificant formulation can vary in ways that are difficult to predict in advance. The WHO, FAO, and the Global Alliance for Improved Nutrition (GAIN) all emphasize that bioavailability estimates must be context-specific; absorption fractions of a single fortificant have been found to vary from 2% to 20%, depending on the population [114]. This variance in absorption can be attributed to a range of factors, including consumption of certain staple foods rich in molecules which inhibit iron absorption, as well as chronic inflammation and infection burdens, both microbial and parasitic [114, 115, 116]. Thus, a fortificant that appears highly bioavailable in one controlled study may perform quite differently in real-world application.

Population-level bioavailability studies using stable isotope tracers are indispensable for bridging the crucial knowledge gap between precise metabolic tracer results in individuals and the impact of iron fortification programs on community health outcomes. They can also inform analyses of cost-effectiveness and sustainability for national programs, because population-level isotope studies provide a direct quantitative measure of effectiveness. For example, population-level isotope data demonstrated that the fortificant ferric sodium EDTA (NaFeEDTA) can be absorbed with double or triple the efficiency of ferrous sulfate ($FeSO_4$) among people with primarily cereal-based diets, because NaFeEDTA is stable and soluble in the intestinal lumen, protecting iron from phytate binding and improving uptake in phytate-rich cereal or legume meals [117]. When inhibitors are low, this advantage disappears, illustrating the food matrix dependence of iron bioavailability [118]. These findings led the WHO and the United Nations Food and Agriculture Organization (FAO) to recommend the use of NaFeEDTA when phytate levels are high, despite its significantly higher material cost, because it is far less expensive in terms of per-dollar effect on iron levels [119].

Two well-known stable iron isotope case studies from Mexico and Morocco illustrate the importance of selecting an effective fortificant, the potentially critical impact that dietary and other factors can have on bioavailability, and the utility of stable isotope methods for answering such research questions. In 1999, roughly two-thirds of Mexican children under two years of age were iron deficient, and about half were anemic [120, 121]. The PROGRESA program in Mexico (later renamed Oportunidades, then Prospera, and now largely replaced by the Becas para el Bienestar Benito Juárez scholarship programs) is widely cited in global nutrition literature as a demonstration of both the potential and pitfalls of iron fortification and supplementation in large-scale poverty alleviation programs. While PROGRESA was primarily a conditional cash-transfer program for households whose children attended school and health checkups, its nutrition component supplied fortified foods for low-income women and children, providing a real-world test of whether anemia and developmental outcomes could be improved at the population level by a large-scale iron fortification program.

However, the initial iron fortificant chosen for the fortified beverage Nutrisano turned out to be chemically inappropriate for the food matrix, resulting in poor iron absorption. This problem, which was identified and analyzed by Prof. Steven Abrams and colleagues, is a textbook example of how fortificant selection, even in a large and well-funded program, can determine success or failure [123]. Beginning in 1999, Nutrisano, a powdered milk-based fortified complementary food[26], was given to infants and small children less than 2 years old in the PROGRESA program. Nutrisano contained added vitamins and minerals, including a 10 mg/day dose of iron. The fortificant initially selected was reduced iron powder, chosen mainly for its low cost and ease of blending with the dry powder. However, as Abrams and others

---

[26] A food given as a supplement to infant formula or breast milk.

Figure 1.18: Nutrisano beverage and supplements.[122].

later demonstrated using stable isotope methods, this form of iron is poorly soluble and biologically unavailable, especially in milk-based foods that lack strong enhancers such as ascorbic acid [124]. Following these findings, Nutrisano was reformulated with a more bioavailable iron fortificant, as well as added ascorbic acid for enhanced iron absorption. Subsequent evaluations showed measurable improvements in the hemoglobin and ferritin of children fed the revised formula [125].

In 2004, Morocco implemented a national wheat-flour fortification program as part of a regional initiative to combat widespread iron deficiency and anemia. The program used elemental iron as a fortificant, with an average fortification level of 45 mg Fe/kg flour [126]. The program objective was to reduce anemia prevalence among women and children, which exceeded 30% at the time the program was implemented [127]. Wheat bread is a Moroccan dietary staple, being consumed at nearly every meal, making it an ideal fortification vehicle.

Yet, despite the fortification of virtually all wheat flour available in the market and consumed by the population, anemia prevalence remained high [127]. Stable

Figure 1.19: Moroccan tea.[128].

iron isotope studies demonstrated that the culprit was, interestingly, tea. Tea is a very important part of the Moroccan diet, where the average consumption is nearly two kilograms of tea per person per year [129]. However, tannins and polyphenols, compounds found in high amounts in tea and coffee, are potent inhibitors of iron absorption, which can be reduced by more than 85% when consumed with strong tea [127, 130]. Researchers concluded that the inhibitory effect of high levels of tea consumption effectively nullified the bioavailability of the fortificant iron from wheat flour, providing nominal iron intake without meaningful absorption. In 2018, a change of fortificant from elemental iron to NaFeEDTA was mandated by the Moroccan government, with stable isotope studies underpinning the decision [131].

1.3.4 Scarcity of pediatric data

Infants and toddlers are among the groups most vulnerable to iron deficiency [98]. Infants have a high nutritional need for iron owing to their rapid growth. Fetal iron stores are depleted after the first 4-6 months of life, and solid foods for infants are often plant-based and low in bioavailable iron. This has made iron fortification and supplementation for infants a public health priority. Yet, despite decades of research on iron fortification in adults and women of reproductive age, there remains a marked scarcity of robust, population-level studies assessing the real-world effectiveness of iron fortificants for infants and children younger than 2 years old [98]. Most national fortification programs target wheat or maize flour, but infants consume too little flour-based food to meaningfully benefit [132, 133]. While there are many short-term studies of iron-fortified complementary foods or micronutrient powders (MNPs), studies with population scale or long-term follow-up to assess sustainability and unintended effects, such as gut infection risks, are relatively few. This research gap is noted by major reviews: the WHO, UNICEF, and NIH highlight “uncertainties, knowledge gaps, and research needs” for iron supplementation in children less than two years old [134, 135, 136]. In addition, infants may respond differently to iron fortificants and supplements than older children or adults: immature hepcidin control may make infants more susceptible to iron overload [137, 138]; increased iron intake in malaria-endemic regions has been demonstrated to increase infection risk [139, 140]; and many infants in LICs exhibit chronic inflammation, making ferritin a poor marker of anemia in some cases [141, 142].

The economic justification for infant-specific formulations remains uncertain without robust population data. However, large-scale, population-representative isotope studies in infants are very technically challenging due to the very small permissible blood volumes and the requirement for specialized analytical infrastructure, including a suitable mass spectrometer and lab personnel trained in performing isotope ratio analysis on medical samples. The goal of this project is to provide an alternative approach. Optical spectroscopy offers an ultra-sensitive analytical method that bypasses the technical bottleneck, while being scalable and cost-effective.

Chapter 2: Experimental / Technical Background

2.1 Protocol for stable isotope tracer studies

Medical studies using stable iron isotopes often make use of an experimentally convenient fact: the human body's store of iron is largely carried in erythrocytes (red blood cells). The storage of iron in the body is sometimes described in medical sources as having three compartments: functional, storage, and transport [143]. About two-thirds of the iron in the human body is found in hemoglobin, the protein that red blood cells use to bind and transport oxygen through the body. The storage compartment is ferritin/hemosiderin, which are biomolecules that can hold around $4,500$ Fe^{3+} ions apiece in their hollow cores, and which are found particularly in the liver, spleen, and bone marrow. The functional compartment is myoglobin, the oxygen-carrying protein equivalent of hemoglobin which is found in muscle tissue. There are sex-related differences in iron stores, both in terms of amount of iron stored, and in where the balance of iron is stored. The average adult woman has a total body iron of about 2.8 grams, and the average adult man has a total body iron of 4 grams. Adult women tend to have less of their total body iron stored in ferritin/hemosiderin than men, due to menstrual losses: on average, men have around 23% of their total iron stored in ferritin, while for women the percentage is closer to 10% [144]. The hemoglobin content of whole blood is about 150 g/L for men, and 135 g/L for women. In terms of the iron content of blood, this translates to about 470 mg Fe/L for women, and 520 mg Fe/L for men [145, 146].

Pediatric blood iron content differs from that of adults in scientifically interesting ways. Newborns initially have much higher blood iron than adults (as high as 700 mg Fe/L), due to the presence of fetal hemoglobin (HbF). Fetal hemoglobin has higher oxygen affinity than regular hemoglobin, helping deliver oxygen in utero from the maternal bloodstream [148]. However, this declines in infants to a nadir

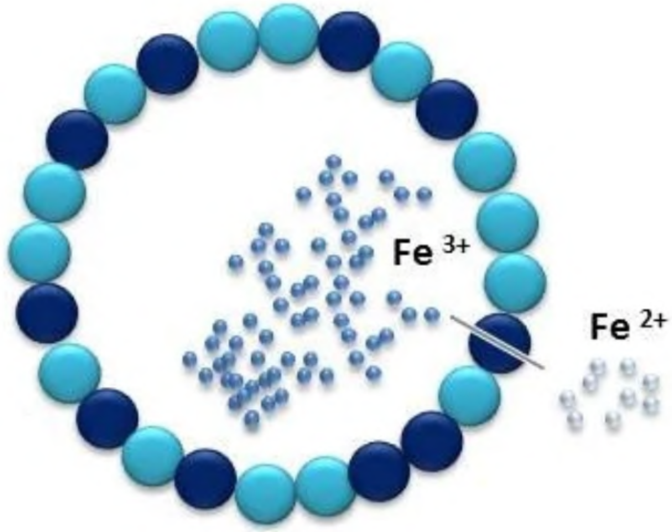

Figure 2.1: Ferritin storing Fe^{3+} ions. Image credit: [147].

of only around 350 mg Fe/L. This is known as physiological anemia[1], because it is the result of physiological changes as the newborn transitions from the intrauterine environment to the outside world. The initial high oxygenation from HbF suppresses erythropoietin (EPO) production in the kidneys, slowing red-cell production in the bone marrow. The fetal hemoglobin is gradually replaced by regular hemoglobin. As children grow, their hemoglobin levels gradually rise to around $380-450$ mg Fe/L, reaching typical adult levels of blood iron during adolescence [149].

2.1.1 Sequence for analysis

The standard protocol for stable isotope tracer studies is to administer a dose in which one or more of the naturally occurring isotopes have been significantly enriched. For iron the enriched isotopes are typically ^{57}Fe and/or ^{58}Fe, because their low natural abundance gives a good signal-to-noise ratio. The dose is delivered with a standardized test meal, which is often the tracer dissolved in orange juice or fruit

---

[1] In distinction to *pathological* anemia.

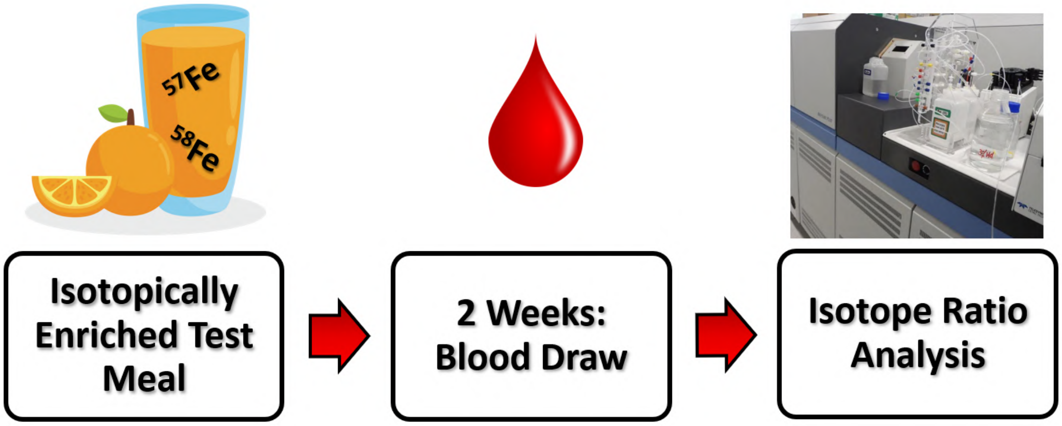

Figure 2.2: Protocol for stable iron isotope tracer studies [150].

syrup [151]. Ascorbate (vitamin C) in the juice helps keep iron in the ferrous $\left(\mathrm{Fe}^{2+}\right)$ state, which is soluble, and helps enhance absorption by forming a chelate with ferric iron in the acidic environment of the stomach, which remains soluble in the alkaline environment of the small intestine [152, 153]. In some studies, the test meal is also given in the form of an isotopically enriched wheat bread roll [154].

Typical doses of elemental iron per test meal are about 5 mg for adults and young children, and $2-2.5$ mg for infants [155, 156, 157, 158]. The doses for children are smaller because their blood volumes are substantially less than that of an adult, so even milligram tracer quantities cause a measurable isotopic enrichment in red blood cells[2]. The goal is isotope ratio enrichment, not supplementing iron intake; the tracer isotope quantity is negligible compared to daily dietary requirements, typically $< 10\%$ of recommended daily allowance (RDA). It is also possible to make use of double or triple stable isotope labeling, by giving some combination of $^{54}\mathrm{Fe}$, $^{57}\mathrm{Fe}$, and $^{58}\mathrm{Fe}$ in different test meals given over several days [159, 160]. The double-labeling approach is most common, however. Multi-isotope labeling allows within-subject comparisons and corrections for red blood cell incorporation, making the measurement of fractional

---

[2] For reference, the typical blood volume of adults is $4-6$ L, while that of a 7 kg infant is 0.5 L.

iron absorption more accurate.

Around two weeks after the tracer was administered, a sample of blood is drawn, and isotope ratios are analyzed to evaluate how much of the dose was absorbed and incorporated into red blood cells [161, 162, 163]. The reason for this timing is that the red cell incorporation of the iron isotope tracer plateaus around 14 days [164]. Earlier or later blood draws are possible, depending on research focus and the population being studied. An initial pre-dose blood draw is used to establish the baseline whole blood isotope ratio for the tracer isotope τ vs. ^{56}Fe :

$$R_{\text{pre}} = \left.\frac{n_\tau}{n_{56}}\right|_{\text{pre}} \tag{2.1}$$

where n_τ represents moles of tracer isotope τ. The post dose ratio is then measured ~ 14 days later:

$$R_{\text{post}} = \left.\frac{n_\tau}{n_{56}}\right|_{\text{post}} \tag{2.2}$$

The dose of tracer iron isotope(s), n_{τ_0}, is known. Denoting the set of stable iron isotopes $k \in \{54, 56, 57, 58\}$, the ratio of a given isotope to the reference isotope can be written:

$$R_k \equiv \frac{n_k}{n_{\text{ref}}}, \qquad \text{with } R_{\text{ref}} \equiv 1 \tag{2.3}$$

As the most abundant isotope, and consequently the strongest signal by far, it is often convenient to choose ^{56}Fe as the reference isotope. Using this convention, the measured fraction of tracer isotope τ, computed in terms of isotope ratios, can be given by:

$$x_\tau = \frac{R_\tau}{\sum_k R_k} = \frac{R_\tau}{1 + \sum_{k \neq 56} R_k}. \tag{2.4}$$

Because only the tracer isotope(s) changes appreciably after dosing, the post-dose "atom excess" of tracer isotope τ can be expressed as the following fraction, A_τ:

$$A_\tau = x_{\tau,\text{post}} - x_{\tau,\text{pre}} = \frac{R_\text{post} - R_\text{pre}}{1 + \sum_{k\neq 56} R_{k,\text{nat}}} \tag{2.5}$$

Here, the term $R_{k,\text{ nat}}$ in the denominator is computed using the naturally occurring, unenriched isotope ratios.

Calculating the fraction of tracer iron incorporated into red blood cells requires estimating the total amount of iron circulating in red cells at the time the blood is drawn. This estimate is based on two quantities: the subject's total blood volume, and the hemoglobin content per unit of blood volume. Blood volume estimates for adults are performed with empirical formulas known as the Nadler equations:

$$\begin{aligned} V_\text{men} &= 0.3669 \times H^3 + 0.03219 \times W + 0.6041 \\ V_\text{women} &= 0.3561 \times H^3 + 0.03308 \times W + 0.1833 \end{aligned} \tag{2.6}$$

where H is height in meters and W is weight in kilograms [165]. The Nadler equations were derived from studies of adults, so for children and infants a different set of empirical relations between body mass and total blood volume are used: newborns typically have blood volume of $80 - 90$ mL/kg, infants $1 - 12$ months old $75 - 85$ mL/kg, and children less than 13 years old $70 - 80$ mL/kg [166, 167].

The amount of hemoglobin per unit volume of whole blood can be determined by a complete blood count (CBC), one of the most standardized clinical lab tests. Modern CBCs are usually performed by automated hematology analyzers, whose operating principles are based either on electrical impedance, or on flow cytometry with lasers. Prior to the introduction of automated systems in the mid-1960s, manual cell counts required 15-30 minutes per patient, whereas with an automated system a CBC can be performed in about 1 minute of instrument time, with vastly higher counts [168]. The underlying physics is surprisingly interesting and applicable, so we will discuss it very briefly. Impedance-based analyzers operate on the Coulter principle, named after electrical engineer and inventor Wallace Coulter, who invented a method to count small particles suspended in fluid in 1953 [169, 170]. Red blood cells suspended in an electrically conductive fluid are drawn through a small aperture with electrodes on either side. As the red cells pass through the aperture, they displace the electrolyte in the aperture. Since the red blood cells are electrically insulating compared to the solution, their passage through the aperture causes brief spikes in electrical impedance, which the instrument registers as a cell count. The pulse height can be correlated to cell volume.

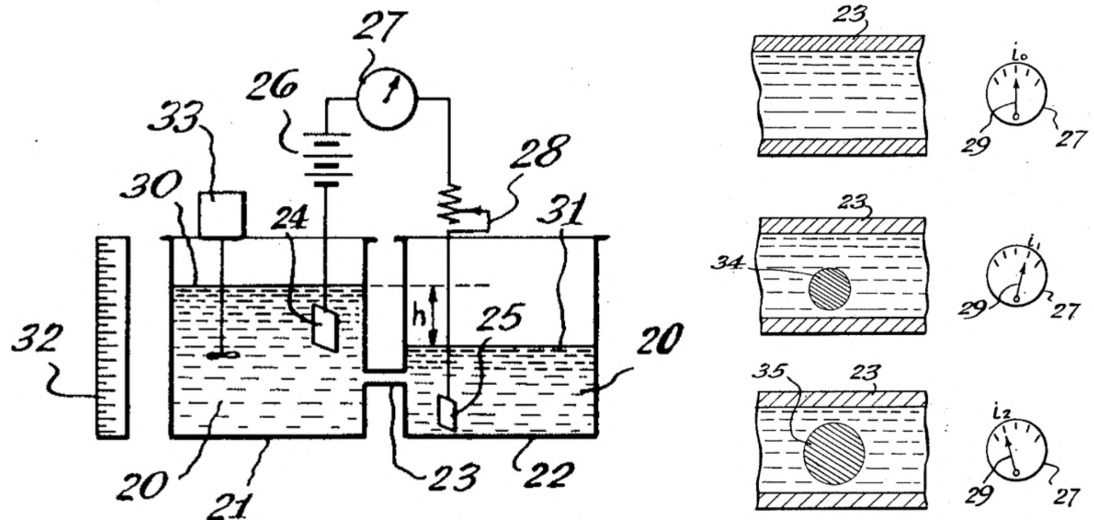

Figure 2.3: Schematics from Coulter's 1953 patent for his counting device [169].

In flow cytometry-based hematology analyzers, cells are injected into a fast-moving saline stream, which forms a "sheath" around the slower-moving sample stream, ensuring laminar flow of the sample stream. The sheath stream hydrodynamically focuses the sample stream so cells pass one by one through the laser interrogation point, which is typically either blue at 488 nm, or red at 633 nm [171]. The historical reason for these wavelength choices is that flow cytometers built before the development of solid-state diode lasers were usually equipped with 488 nm argon-ion or 633 nm HeNe lasers, and these wavelengths became standard, particularly the 488 nm blue laser [172]. As cells pass through the laser beam, the forward-scattered

(FSC) and 90° side-scattered (SSC) light is split by dichroic mirrors and collected on photomultiplier tubes (PMTs).

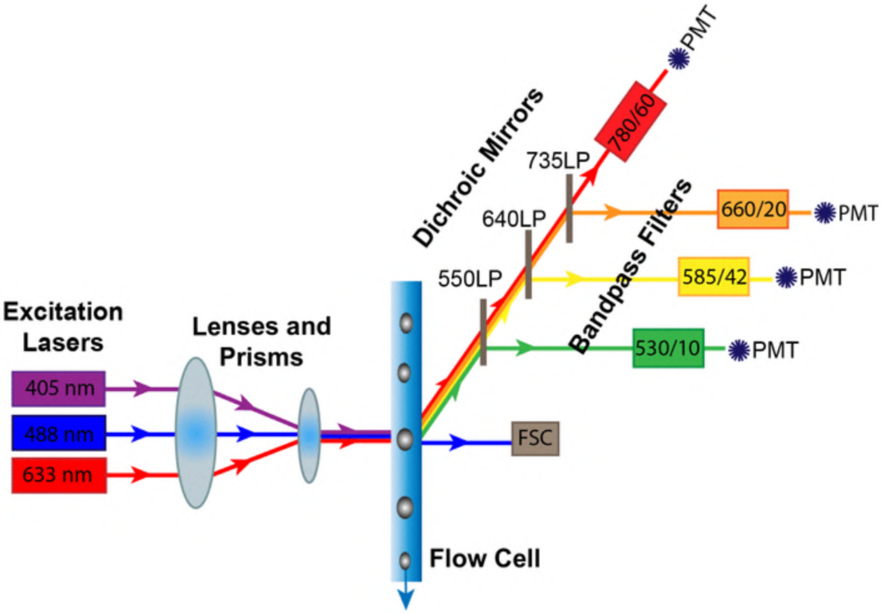

Figure 2.4: Modern flow cytometer [173].

The intensity of the forward-scattered light is proportional to the square of the cell diameter d [174]:

$$I_{\text{FSC}} \propto d^2 \tag{2.7}$$

At the large scattering angles of the side-scattered light, scattering intensity is sensitive to the internal structure of the cells, with the intensity varying as

$$I_{\text{SSC}} \propto (\Delta n)^2 \times N_{\text{substructures}} \tag{2.8}$$

where Δn is the refractive index difference between cellular substructures and their surrounding cellular cytoplasm, and $N_{\text{substructures}}$ is the number of those structures. In the case of cells, this is referred to as "granularity," and is due to subcellular structures such as nuclei, vesicles, and membranes. This provides a signature allowing identification of the cell type. For example, granulocytes, a type of white blood cell, are (unsurprisingly) highly granular. Lymphocytes, a different type of white blood cell, are largely simple cytoplasm and have low granularity.

From the above measurements, the iron contained in circulating hemoglobin can be found from:

$$n_{\mathrm{Fe(Hb)}} = \underbrace{V \times [\mathrm{Hb}]}_{\text{grams Hb in blood}} \times \left(6.21 \times 10^{-5}\ \frac{\text{mol Fe}}{\text{g Hb}}\right) \tag{2.9}$$

Here V is the total estimated blood volume, and [Hb] is the measured concentration of hemoglobin. The quantity of isotope tracer in red blood cells is given by:

$$n_{\tau(\mathrm{RBC})} = \mathrm{A}_{\tau} \times n_{\mathrm{Fe(Hb)}} \tag{2.10}$$

The fractional absorption of the tracer is, of course, given by the ratio of the tracer in the red blood cells divided by the original tracer dose n_{τ_0} :

$$\mathrm{F}_{\tau} = \frac{n_{\tau(\mathrm{RBC})}}{n_{\tau_0}} \tag{2.11}$$

For double-isotope studies, the relative absorption of two different test meals dosed with tracer isotopes τ_1 and τ_2 is given by:

$$\text{Relative absorption } = \frac{\mathrm{F}_{\tau_1}}{\mathrm{F}_{\tau_2}} \tag{2.12}$$

Some fraction of tracer isotope iron is incorporated into stores in the liver or myoglobin in muscle, instead of making its way into red blood cells. However, it is possible to experimentally correct for the loss of tracer into other iron compartments. If a small dose of an isotope different from the tracer isotope(s) of interest is given intravenously around the time that the test meal is given, then this provides a quantitative measure of red blood cell incorporation efficiency, helping to correct oral absorption calculations [162]. Because the IV tracer is injected directly into the bloodstream and bypasses gut absorption processes, its "absorption factor" is essentially 100%. Measuring the ratio of this IV microtracer that is incorporated in red blood cells allows calculation of a correction factor representing the fraction of absorbed iron which a particular individual's metabolic process directs to red blood cells:

$$f_{\mathrm{RBC}} = \frac{n_{\mathrm{IV(RBC)}}}{n_{\mathrm{IV(dose)}}} \tag{2.13}$$

The corrected fractional absorption becomes:

$$\mathrm{F}_{\tau} = \frac{n_{\tau(\mathrm{RBC})}}{n_{\tau_0}} \times \frac{1}{f_{\mathrm{RBC}}} \tag{2.14}$$

The remaining piece of the puzzle is the determination of isotope ratios, which we turn to in the next section.

2.1.2 Alternative to mass spectrometry

The analytical portion of stable isotope studies usually relies on mass spectrometry, which is a sensitive and powerful method. However, the practical sample throughput for isotope ratio analysis is limited to dozens of samples per day. Additionally, the equipment and personnel overhead is immense: both a million-dollar mass spectroscopy device and laboratory personnel with the specialized training to prepare biological samples for analysis are needed [175]. Perhaps the most significant obstacle to large-scale iron isotope tracer studies is complex, time-consuming sample preparation.

Before isotopic analysis, iron must be separated from isobars[3], whose mass signature interferes with that of the iron tracer isotopes. For example, ^{54}Cr interferes with measurements of ^{54}Fe, and ^{58}Ni interferes with ^{58}Fe. Sample preparation requires

---

[3] Isotopes of different elements with the same atomic mass.

at least a couple of days for a well-equipped lab [176, 177]. For blood samples, the procedure requires $16-24$ hours of drying and heating in a muffle furnace, 2-3 hours to prepare the sample in concentrated hydrochloric acid for anion-exchange chromatography, around 2 hours for the purification process, then another hour to dry and reconstitute the purified samples [178, 179, 180]. This procedure is not well-suited to processing hundreds or thousands of samples. Subsequent sections discuss our sample processing methods in detail; it is worth noting here that we have been able to reduce sample preparation time to around 2.5 hours, from whole blood to analysis-ready sample; these methods can be performed by laboratory technicians without special training, and are plausibly scalable to hundreds or more samples per day. Additionally, the most expensive hardware required is a narrow-linewidth external cavity diode laser (ECDL) costing two orders of magnitude less than a mass spectrometer.

2.1.3 Pediatric blood draw

Studying pediatric iron deficiency requires working with very small blood samples, typically on the order of a few hundred microliters, and presents significant technical challenges [181, 182]. The difficulty arises from physiological factors compounded by stringent limits on sample volume, as well as ethical constraints on pain and risk. Infant phlebotomy requires specific training, and novice collectors have a first-attempt success rate of $< 50\%$ [183]. The total blood volume in a newborn is only about $250-300$ mL, so even small samples of 1-2 mL represent a significant fraction of circulating blood [184]. In addition, infant veins are small, mobile, and collapsible. They lack the connective tissue stabilization seen in older children, making venipuncture technically difficult [185]. The subcutaneous fat layer can obscure veins, especially in healthy term infants. Prolonged bleeding can occur after puncture because platelet function and coagulation factors are not yet at adult levels [186].

The preferred methods for drawing blood samples from young children and infants are a heel stick with a lancet, drawing blood by capillary tube or onto a filter paper spot card. Capillary tubes for pediatric blood sampling are typically anticoagulant-coated glass or plastic with a $70 - 100$ μL capacity [185]. They enable the safe collection, transport, and analysis of blood microsamples from infants. There is a difference in the composition of blood drawn by capillary tube from a heelstick in comparison to blood drawn by venipuncture. Capillary blood consists of a mixture of arterial blood, venous blood, and interstitial fluid, with the proportions varying depending on collection site and sampling technique [185]. The red blood cell (RBC) count of capillary blood is equal to or slightly higher than that of venous blood, by about 6% [187]. For some applications, this difference in blood composition could complicate analysis, but should not adversely affect iron isotope ratio measurement.

Figure 2.5: Left: Dried blood spot card. Right: Capillary tube sampling. [188, 189]

Blood spot cards are one of the most widely used sampling devices in pediatric medicine, making newborn screening feasible worldwide, and allowing accurate biochemical, genetic, and elemental testing from very small volumes of blood [190]. The cards were developed by American microbiologist Robert Guthrie in the early 1960s for phenylketonuria[4] (PKU) screening [191]. Dried blood spot (DBS) sampling is now used globally to screen newborns for more than 50 metabolic, endocrine,

---

[4] An inherited disorder causing decreased metabolism of the amino acid phenylalanine. Early diagnosis allows a normal lifespan and development, while untreated PKU can cause intellectual disability and seizures.

and genetic disorders [192]. DBS methods have been adapted to a wide range of other research and screening purposes as well, including pharmacokinetic studies, infectious disease testing for HIV, hepatitis, and malaria, and trace-element studies [193, 194, 195, 196, 197]. DBS sampling involves collecting a few drops of blood from a heel puncture onto a specially prepared filter paper card. Once dried, the blood forms uniform circular spots that can be stored, transported, and analyzed later. Each spot on a DBS card holds $50 - 75$ μL of blood. With 4-5 printed circles per card, the total blood volume a single card can accommodate is roughly 300 μL.

2.2 Sample preparation

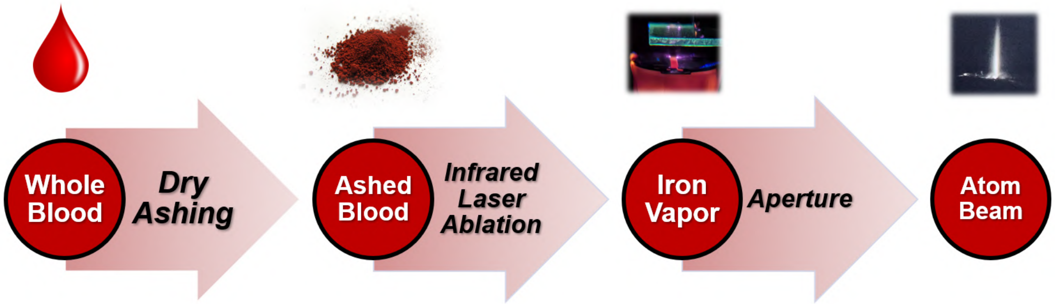

Figure 2.6: Chain of blood sample processing.

Pictured in Figure 2.6 is a schematic of the sample processing chain, which begins with whole blood and ends with a beam of atomic iron vapor. Blood samples are prepared for spectroscopic analysis by a process called dry ashing, which reduces the sample to mineral oxide powder. This powder sample is vaporized by an infrared (IR) laser in vacuum. An aperture is used to select only the components of the flux of vaporized iron with velocity components which are nearly perpendicular to the laser probe beam. The small rightmost image is a photo of the 372 nm fluorescence from the collimated iron beam crossed at right angles by the excitation laser.

2.2.1 Wet/dry methods: capillary tubes and blood spot cards

Capillary tube samples and dried blood spot (DBS) cards have significantly different handling, storage, and transport requirements. Capillary tubes preserve liquid blood for immediate laboratory analysis but require more controlled handling and cold storage, while DBS cards render liquid blood into a stable, dry, low-risk material suitable for shipping and long-term storage. Liquid capillary blood samples generally require continuous refrigeration at $2 - 8$ °C and have a storage stability of weeks for trace element analysis [198, 199]. By contrast, DBS cards are stable for months in climate-controlled storage, and if refrigerated or frozen, can be stored for years [200]. Additionally, the biosafety requirements are different: after drying for 3-4 hours, DBS cards can be placed in a gas-permeable envelope with desiccant and conveniently shipped at ambient temperature to a laboratory for analysis, whereas liquid blood samples are subject to restrictions on potentially infectious materials, requiring secondary containment and biohazard labeling [185, 201, 202, 203].

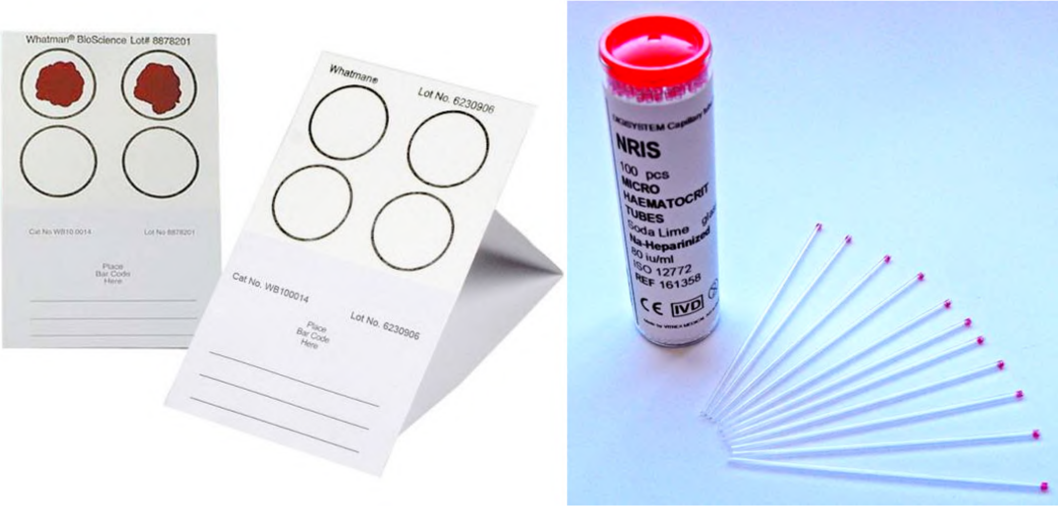

Figure 2.7: Left: Dried blood spot cards. Right: Capillary sampling tubes [204, 205].

Isotope ratio analysis is a technically challenging application for DBS methods, but there are circumstances for which their reduced storage and handling requirements would be invaluable, particularly for studies conducted in low- and middle-income countries (LMICs). For researchers contending with limited refrigeration or electricity, remote field sites without nearby analytical labs, or difficulties transporting biohazardous materials across borders, DBS cards may be the best option. The distribution of blood within a dried blood spot is not perfectly uniform, and this non-uniformity is one of the key analytical challenges of DBS card sampling [206]. Although the spots produced on a card are visually uniform, the concentration of analytes varies across the spot, with radial and vertical concentration gradients, primarily caused by wicking effects. Even with ideal spotting technique, cellular and plasma components separate microscopically as the drop wicks outward in the porous cellulose, resulting in analyte concentration gradients. Quantitative studies show a 5-20% concentration difference between the center and edge of a spot for many analytes such as amino acids, and greater than 30% variation of analyte is possible if hematocrit[5] and punch location are not controlled [207]. Consistent technique, controlled drying, and standardized punching are essential to constrain experimental error.

Capillary blood samples are straightforward by comparison: methods we have developed can rapidly render a liquid whole blood sample into an analysis-ready mineral oxide powder with minimal equipment and preparation time required. Adaptation of these methods to DBS cards was found to require adjustments to the procedure to avoid significant volatilization losses during the sample ashing step. The isotopic ratio analysis method discussed here is largely focused on the use of whole blood microsamples, intended to be used with capillary blood sampling. This is a sensible initial phase, as all analytical methods downstream of the ashing step are identical for capillary and DBS card samples.

---

[5] The fraction of total blood volume occupied by red blood cells.

2.2.2 Dry ashing

Dry ashing is one of the oldest and simplest approaches for extracting the inorganic fraction of organic materials and is a standard method for isotope ratio analysis of biological samples such as blood, urine, or tissue. Dry ashing involves heating an organic sample at elevated temperature, typically $450-600$ °C, until all organic matter is destroyed, leaving a powdered ash containing the elements of interest. The earliest account of dry ashing small biological samples for isotope tracer analysis is from George de Hevesy [208]. In a 1923 paper, de Hevesy investigated the uptake of lead by fava bean plants, using the lead radioisotope discussed in Section 1.2.1 as an isotopic tracer. The paper describes taking small plant samples, ashing them, and then measuring the ^{210}Pb tracer signal directly from the ash, which avoids the attenuation of β-decay signal that would occur in solution. de Hevesy's methods were extended by John Lawrence and his collaborators at UC Berkeley for their ^{59}Fe tracer studies. In a 1940 paper, Berkeley researchers discuss standardizing a dry ashing method for iron radioisotope tracers in tissue samples from rats [209]. Having established that dry ashing is needed to avoid the "enormous" absorption of β-particles in solution, they reported that sample loss during the ashing process can be "minimized by carrying out the early heating at a low temperature ($350-400$ °C) and increasing it not to exceed 700 °C. An experimental test of this procedure with labeled iron showed that, if the early heating is carried out at low temperature, the iron can then be strongly heated without any loss." This early finding is consistent with results from the research in this dissertation.

Dry ashing is ideal for our optical methods of isotope ratio measurement, because high-sensitivity laser-induced fluorescence (LIF) spectroscopy requires a high vacuum (HV) environment, and therefore a dry powder sample. As discussed in Section 2.1.3, optical spectroscopy lacks mass spectroscopy's significant laboratory overhead for removing isobars from samples before analysis. One of the key analytical benefits of LIF spectroscopy is how much more time- and cost-efficient sample preparation becomes: there is no need to purify samples or perform separation before analysis, since the measurement is keyed to a specific atomic transition of iron, and is inherently blind to all contaminants. This allows the LIF approach to focus on making sample processing as rapid as possible. Because the chemical purification steps for mass spectroscopy can be largely sidestepped, the primary constraint on sample preparation is avoiding sample loss due to evaporation.

When whole blood is dry ashed in a muffle furnace, organic molecules such as proteins, lipids, and carbohydrates are oxidized to gaseous carbon dioxide, water, and nitrogen. What remains is a small quantity of inorganic mineral residue, a complex mixture of metal oxides, phosphates, and sulfates derived from the mineral constituents of blood [210]. The mass yield of ashed whole blood is about 1.1% of the original blood mass after heating at 450 °C for 8 hours in air [211]. Whole blood is approximately 80% water, which suggests the mass of mineral ash is roughly 6% of the mass of the dry weight of blood solids. Whole blood ash contains about 700 μg of iron oxide in the form of hematite, Fe_2O_3, per mL of blood sample, assuming minimal losses. For the work discussed here, we used human whole blood samples purchased from Innovative Research [212]. The single-donor samples were drawn from healthy adults and screened for bloodborne pathogens at the supplier's partner collection facilities, then shipped to us. The anticoagulant used for the samples was K2 EDTA. Pediatric blood samples were available as well, but we determined that consuming specialized samples during the building and calibration phase of the instrument would be wasteful. Our ashing furnace was a 3-liter Carbolite Gero AAF 11/3 [213].

Whole blood microsamples, with volumes between 50 μL and 250 μL, were pipetted into conical sample holders using fixed-volume micropipettes from McMaster-Carr [214]. The sample holders were fabricated from machinable Macor glass-ceramic rods; Macor was chosen because of its stability at temperatures up to 1000 °C, and because its machinability with standard tools simplifies the prototyping process significantly compared to ordering custom parts [215]. Both sample and holder were

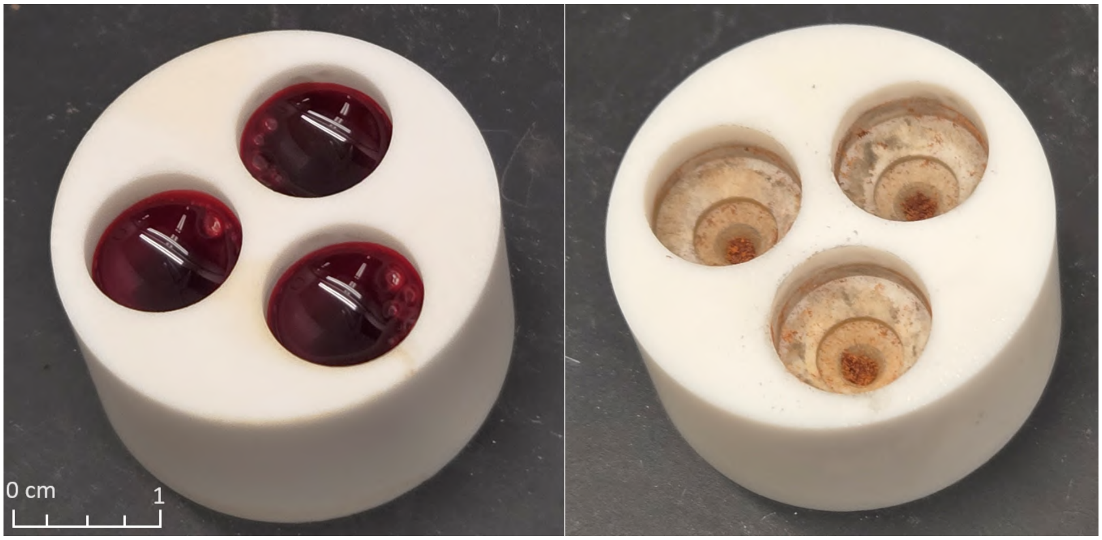

Figure 2.8: Left: 3×150 μL whole blood samples. Right: samples after ashing.

initially placed into the Carbolite muffle furnace cold. The principal concern during the ashing process is minimizing sample loss. Prior studies have demonstrated that losses of iron during the dry ashing of biological samples can be negligible, with enough care over temperature control [216]. Because of the high water content of whole blood samples, there is common concern in the literature over the bumping or boiling of the sample, with losses due to spatter [211]. Dry ashed blood samples are typically pre-treated on a laboratory hot plate or similar at $100 - 105$ °C to dry and thicken the sample before furnace heating; some protocols char the sample over a $300 - 350$ °C Bunsen burner flame until the sample ceases to smoke [217, 218]. We found that, when handling microliter instead of milliliter samples, the pre-heating step can be skipped without measurable sample loss. The smaller samples have significant surface area relative to their volume, over which a hard dark surface rapidly forms, preventing spatter.

Typical dry ashing protocols call for a muffle furnace temperature ramp of $50 - 100$ °C/h from room temperature to 450 °C, then held at this temperature for $8 - 12$ hours [219, 220]. After experimentation with temperature parameters, we found that the ashing time can be dramatically reduced for LIF spectroscopy. As

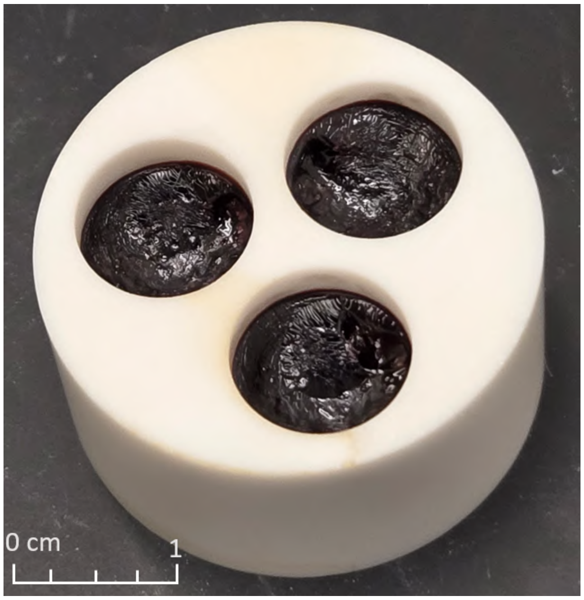

Figure 2.9: 150 μL samples with hardened surface after heating at 80 °C for 15 minutes on a hot plate.

discussed above, the standard ashing time for a whole blood sample is roughly 12 to 21 hours, not including several hours of pretreatment; we found that microliter-scale whole blood samples can be reduced to analysis-ready dry powder in 2 hours. Placing samples in the cold muffle furnace with a temperature ramp of 10 °C/min from room temperature to 550 °C, followed by a 1 hour hold at this temperature, then removal from the oven to cool at laboratory temperature produced repeatable results without significant sample loss.

2.2.3 Sample compaction

The earliest phase of our project used 25 mg samples of iron oxide powder[6] from Sigma-Aldrich to test the process of producing a flux of neutral atomic iron from ablation via a 1064 nm CW YAG laser subject to mechanical chopping at $40-200$ Hz [221]. Initial tests indicated that loose powder produces a highly variable

---

[6] Grain size < 5 μm.

flux, an effect described in light-induced breakdown spectroscopy (LIBS) and laser ablation inductively-coupled plasma mass spectrometry (LA-ICP-MS) literature [222, 223, 224]. There are several mechanisms underlying the unstable flux from ablation of loose powder. The powder has a large void fraction with significant spatial variation; ray tracing simulations demonstrate how laser photons incident on a powder bed are much more strongly absorbed than they are on a flat surface, because the photons undergo multiple scattering events between the grains [225, 226, 227]. Because of the spatial variance of the surface, neighboring spots can be in very different thermal regimes, causing instability in the flux of ablated material.

Poor thermal contact between powder grains is another cause of ablated flux instability; heat flows between the iron oxide grains almost entirely through tiny Hertzian[7] contacts, especially in vacuum [228, 229, 230]. In a loose powder the total contact area is small, which leads to low effective thermal conductivity k_{eff}. Small random differences in packing give rise to large differences in peak temperature. Additionally, water vapor and air trapped in the voids between powder grains can be suddenly released as the powder is heated, producing intermittent spikes in flux[8][231]. Because there is little mechanical integrity in loose powder, grains can also be ejected whole without being vaporized; simulation of laser powder-bed fusion shows that keyhole effects in melting powder can lead to spatter and the ejection of nearby grains [232, 233, 234].

One recognized solution to the instability of ablated flux from powder is to compress the sample. To understand the mechanisms for this, consider treating the chopped IR beam as a periodic surface heat flux. For a sinusoidal flux of amplitude q_0 at angular frequency $\omega = 2\pi f$, the amplitude of the temperature change is given by:

---

[7] Developed by Heinrich Hertz, the theory of Hertzian contacts describes the physics of interaction between two curved surfaces.

[8] Sometimes called "popcorning."

$$\Delta T_{\mathrm{surf,AC}} = \frac{q_0}{e\sqrt{\pi\omega}} \tag{2.15}$$

where $e = \sqrt{k\rho c_p}$ is the thermal effusivity, and k is the thermal conductivity of the powder material [235, 236]. For a unipolar (i.e., $0 \leftrightarrow 1$) square wave with 50% duty cycle, as for an optical chopper, the Fourier fundamental has amplitude $2/\pi$ relative to its DC-to-peak level [237]. Thus, the surface temperature oscillation at the chop frequency is the result above with $q_0 \rightarrow (2/\pi)q_{\mathrm{peak}}$. In a granular target the controlling property for periodic heating is the effusivity e. Compacting the powder increases the contact area between grains, increasing the thermal conductivity k, and hence the thermal effusivity. Similarly, compacting the powder increases the density ρ, and by extension, e. Because $\Delta T_S \propto 1/e$, pressed powder experiences smaller temperature swings, damping variability in ablated flux. In addition, the mechanical strength of pressed powder is far greater than for loose powder, so thermal stresses from heating are much less likely to result in spallation or whole-grain ejection.

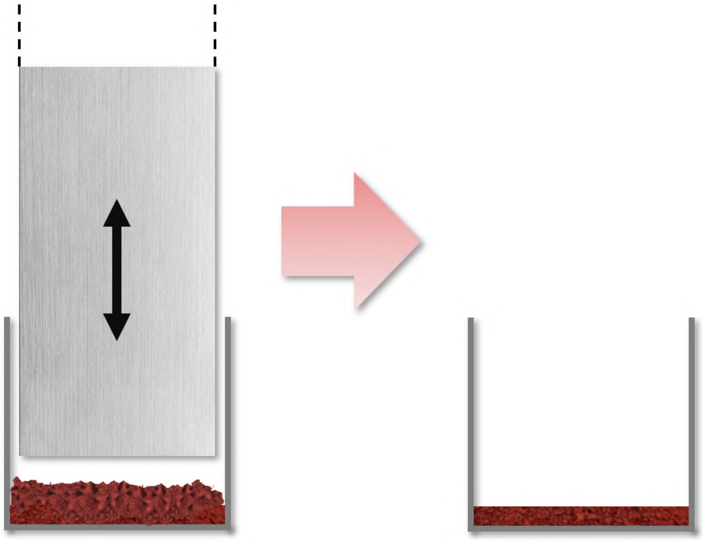

Figure 2.10: Manual tamping process for iron oxide powder samples.

Preparation of the iron powder test samples involved placing them into a 1″ × 1/2″ (H × D) alumina crucible from McMaster-Carr and compressing them to produce a uniform surface for exposure to the infrared ablation laser [238]. The powder was hand-pressed in the crucible using a flat-bottomed aluminum tamping rod with a diameter slightly less than the interior diameter of the crucible. Slow tamping of the powder was repeated until a visually uniform surface was produced, without cracking or cratering, and the powder volume could no longer be reduced. The smooth, densified surface produced is more reflective than the rough powder surface, and we found that the initial flux level could be lower than desired; this low flux was improved by a reduced-power[9] raster of the ablation laser over the surface. The physical process underlying this conditioning step is possibly the micro-texturing and effective "blackening" of the compressed powder surface, increasing its optical absorptivity; literature on laser surface texturing indicates that low- and moderate-power laser rastering creates tiny dimples, grooves, and ripples in surfaces, changing their optical and thermal coupling properties [239]. This "roughening" may also be due to the thermally driven change of the iron powder from hematite (Fe_2O_3) to magnetite (Fe_3O_4), coarsening the powder grains and changing their IR reflectivity; an effect that is noted in literature and observed in our experiments [240, 241, 242, 243].

2.2.4 Microsamples

In medicine, one "metric" drop of liquid is usually considered to be 50 μL [244]. This is a standardization of the early 19th century *minim*, the smallest unit in the apothecary measuring system [245]. Our sample processing renders a single-drop 50 μL sample of liquid blood or blood absorbed into filter paper to around 36 μg of dry iron oxide powder. Initial tests used a standard capillary sample size of 0.5 mL as a target; at current sample efficiency, we are able to produce reliable isotope spectra from "3-drop," or 150 μL, samples of whole blood. With more optimization, it should be feasible to perform reliable isotope ratio analysis with single-drop blood samples.

Fig.2.11 illustrates our current method for processing blood microsamples. The

---

[9] Typically, $\leq$ 800 mW.

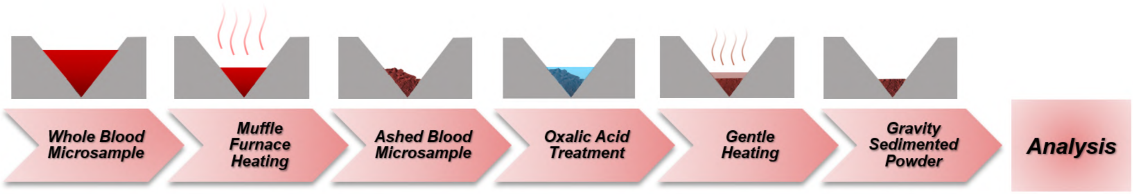

Figure 2.11: Microsample ashing procedure: whole blood is ashed, treated with oxalic acid, and gently heated to settle under gravity.

conical sample holder has large enough volume to hold the liquid whole blood sample, while allowing the ash to be collected and compacted at the tip of the cone. The prior method of preparing oxide powder samples with a flat-bottomed tamping rod is no longer practical for microgram samples; non-mechanical procedures for collecting and compacting the powder must be used. Iron oxide is somewhat soluble in oxalic acid, which we use to form a concentrated suspension of ash at the bottom of the cone. This suspension is gently heated, and the iron oxide sediments under gravity to a denser and more uniformly packed powder, with a smooth top surface. The sample holder used for these experiments was designed to fit on the end of a modified Accu-Glass UHV rotary vacuum feedthrough, and uses a stepper motor to automatically switch between samples in our vacuum chamber with the press of a button [246]. The collimating aperture is fixed in the chamber so that it stays in place while new samples rotate into place below it. At the time of writing[10], our prototype sample holders can accommodate three samples at once (see Figs. 2.8 and 2.12), which reflects a size constraint due to their being inserted and removed from the chamber through a 2.75″ CF flange. In later iterations, a vacuum load-lock system will accommodate a holder designed for many tens of samples at once.

Defining the solid volume fraction $\phi = V_{\text{solid}} / V_{\text{total}}$[11], the densest random packing for a powder composed of rigid monodisperse spheres is known as random close packing (RCP), with $\phi \approx 0.64$ [247]. Gravity-sedimented fine powders settle to

---

[10] Winter 2025.

[11] Porosity $\varepsilon = 1 - \phi$.

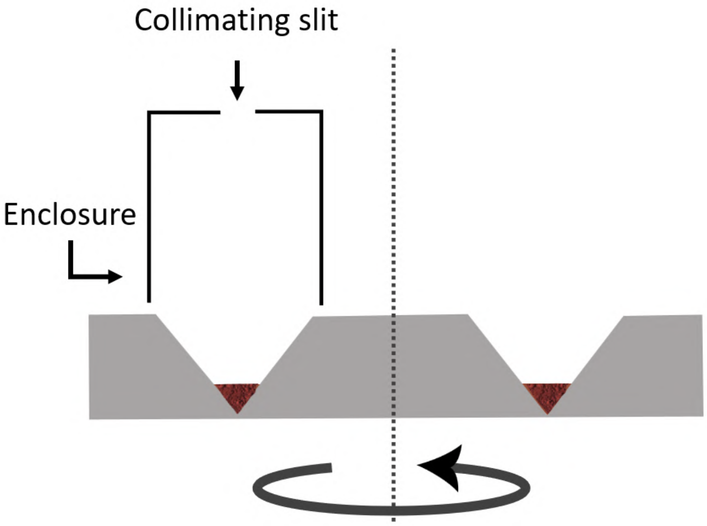

Figure 2.12: Rotary sample holder and collimator.

a grain arrangement close to RCP, with $\phi \approx 0.60 - 0.64$, and hence to similar density. The reason for this is that the capillary stress during drying is far greater than the force of gravity, and comparable to the force of centrifugation. When a wet porous bed of particles dries, liquid retreats into its pore network. The air-liquid menisci that form across the pore throats are curved. By the Young-Laplace equation, a curved meniscus has a pressure difference:

$$\Delta P = P_{\text{liquid}} - P_{\text{air}} = \frac{2\gamma \cos\theta}{r} \tag{2.16}$$

where γ is the liquid-air surface tension, θ is the contact angle of the liquid on the particle surface, and r is the effective radius of curvature of the meniscus [248]; r is usually considered to be approximately the pore throat radius. Since r is small for fine powder, ΔP is large. For example, for water, $\gamma \approx 0.072$ N/m, and $\cos\theta \approx 1$ on clean hydrophilic surfaces. Thus, as liquid leaves the pores, curved menisci pull grains together via Laplace pressure, which is significantly greater than gravity: for pore radius 1 μm, $\Delta P \approx 0.14 \times 10^5$ Pa, and for pore radius 0.1 μm, $\Delta P \approx 1.4 \times 10^6$ Pa. These values are comparable to the effect of a laboratory centrifuge.

Oxalic acid has been used since the 19th century to remove rust stains from artworks, such as paintings, ceramics, and sculptures [249]. The reason why iron oxide dissolves in oxalic acid, even though it is classified as a weak acid, is that the formation of Fe(III)-oxalate complexes is strongly favored. The stepwise equilibrium is given by:

$$\begin{gathered}
\mathrm{Fe^{3+}} + \mathrm{C_2O_4^{2-}} \rightleftharpoons \left[\mathrm{Fe}\left(\mathrm{C_2O_4}\right)\right]^{+} \\
\left[\mathrm{Fe}\left(\mathrm{C_2O_4}\right)\right]^{+} + \mathrm{C_2O_4^{2-}} \rightleftharpoons \left[\mathrm{Fe}\left(\mathrm{C_2O_4}\right)_2\right]^{-} \\
\left[\mathrm{Fe}\left(\mathrm{C_2O_4}\right)_2\right]^{-} + \mathrm{C_2O_4^{2-}} \rightleftharpoons \left[\mathrm{Fe}\left(\mathrm{C_2O_4}\right)_3\right]^{3-}
\end{gathered}$$

The stability constants are defined as:

$$\begin{aligned}
\beta_{11} &= \frac{\left[\mathrm{Fe}\left(\mathrm{C_2O_4}\right)\right]^{+}}{[\mathrm{Fe}]^{3+}\left[\mathrm{C_2O_4^{2-}}\right]} \\
\beta_{12} &= \frac{\left[\mathrm{Fe}\left(\mathrm{C_2O_4}\right)_2\right]^{-}}{[\mathrm{Fe}]^{3+}\left[\mathrm{C_2O_4^{2-}}\right]^2} \\
\beta_{13} &= \frac{\left[\mathrm{Fe}\left(\mathrm{C_2O_4}\right)_3\right]^{3-}}{\left[\mathrm{Fe^{3+}}\right]\left[\mathrm{C_2O_4^{2-}}\right]^3}
\end{aligned}$$

At room temperature and molarity of 0.1M, $\log \beta_{11} \approx 13.2, \log \beta_{12} \approx 23.7$, and $\log \beta_{13} \approx 30.8$. These are relatively large values, meaning that $\mathrm{Fe^{3+}}$ is very inclined to complex with oxalate. There is also a slower reaction, where the oxalate reduces $\mathrm{Fe^{3+}}$ to $\mathrm{Fe^{2+}}$, and precipitates crystalline ferrous oxalate dihydrate ($\mathrm{FeC_2O_4 \cdot 2H_2O}$). This is not desirable from our perspective because the iron comes out of solution, and because the IR ablation of the dihydrate does not produce significant neutral iron vapor. However, recent experiments have demonstrated that on the timescale of tens of minutes, as needed for sample preparation, the quantity of dihydrate formed is negligible. The small quantity of residue left after sample preparation does not appear to have negative downstream effects on isotope analysis, in terms of either ablated flux or Fe fluorescence.

2.3 Laser-induced fluorescence spectroscopy

Producing a flux of neutral atomic iron by IR laser ablation was the first experimental challenge of our project. When hematite (αFe_2O_3) is illuminated by an infrared (IR) laser in vacuum, the primary effect is photothermal heating: the iron oxide lattice absorbs energy, and the laser spot heats rapidly[250]. Under low oxygen partial pressure, iron oxide reduces to elemental iron in a stepwise series of thermally driven reactions. In vacuum, oxygen is removed as it forms, driving the reduction reaction forward. The sequence is: αFe_2O_3(hematite) → Fe_3O_4(magnetite) → FeO (wüstite) → Fe (iron), with O_2 desorbing at each step [251]. This cascade is the standard reduction pathway for iron oxides [251, 252, 253].

$$\begin{gathered} 6\mathrm{Fe_2O_3(s)} \rightarrow 4\mathrm{Fe_3O_4(s)} + \mathrm{O_2(g)} \\ 2\mathrm{Fe_3O_4(s)} \rightarrow 6\mathrm{FeO(s)} + \mathrm{O_2(g)} \\ 2\mathrm{FeO_4(s)} \rightarrow 2\mathrm{Fe(s)} + \mathrm{O_2(g)} \end{gathered} \tag{2.17}$$

Additionally, on cooling, wüstite (FeO) can decompose directly to elemental iron via:

$$4\mathrm{FeO} \rightarrow \mathrm{Fe_3O_4} + \mathrm{Fe} \tag{2.18}$$

so even without a strong external reductant, Fe atoms can appear once FeO forms.

Trace quantities of carbon are known to promote oxygen-vacancy formation and Fe (III) reduction on hematite surfaces in vacuum [257]. Thus, we have also experimented with "incomplete" ashing, in which blood samples are removed from the muffle furnace before carbonized blood components have been fully vaporized. The result is a significantly enhanced sensitivity to the IR ablation; lower laser power produces higher detected fluorescence peaks, in comparison to fully ashed samples. The tradeoff is that although the flux of neutral iron produced at a given ablation

Figure 2.13: Left: Hematite (αFe_2O_3). Middle: Magnetite (Fe_3O_4). Right: Wüstite (FeO) [254, 255, 256]

laser power is improved, the iron flux stability is worsened. Further work is needed to explore applications for this effect.

2.3.1 372 nm transition

The strong Fe I resonance line near 372 nm connects the ground state $3d^6\,4s^2\ a\,{}^5D_4$ to the odd-parity excited state $3d^6\,4s\,4p\ z\,{}^5F^\circ_5$. NIST data lists the upper level[12] at 26874.548 cm^{-1}, giving a vacuum wavelength $\lambda_{\mathrm{vac}} \approx 372.099$ nm [258]. The excited state lifetime is about 61.7 ns [259]. Using the lifetime-linewidth relation for a Lorentzian line,

$$\Delta\nu_{\mathrm{FWHM}} = \frac{1}{2\pi\tau}, \tag{2.19}$$

with $\tau = 61.7$ ns,

$$\Delta v = \frac{1}{2\pi \times 61.7 \times 10^{-9}} \approx 2.58 \times 10^6 \text{ Hz} \tag{2.20}$$

This transition is not closed, as the excited state has a small branching leak to metastable even-parity levels, meaning that the iron atoms can cycle over this

---

[12] The ground state is of course at 0 cm^{-1}.

transition an average of 244 times before falling into a dark state [260]. This leak can be reduced to 1 : 1398 with a 501 nm repump laser, but this step has been unnecessary for our analytical purposes so far [261, 262]. The saturation intensity of the transition is $I_{\text{sat}} = 6.57$ mW cm^{-2}. This line is one of the strongest Fe (I) resonances in the ultraviolet and has found significant technological application as the working line for Fe resonance lidar [263].

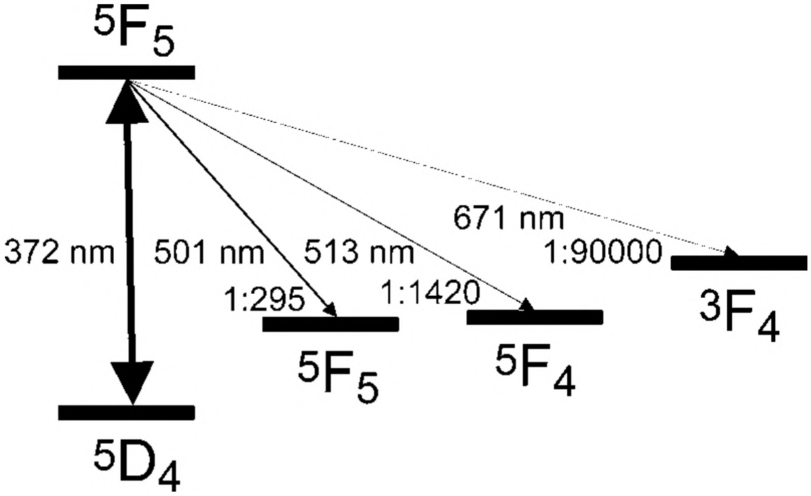

Figure 2.14: Level scheme of the 372 nm transition of atomic iron, including the three small branching leaks. Image credit: [262].

Fe resonance lidar is a remote-sensing technique that points a narrowband, frequency-tunable laser into the night sky to resonantly excite the naturally occurring layer of neutral iron atoms in the upper mesosphere/lower thermosphere[13]. The backscattered resonance fluorescence is collected by telescope, and provides measures of wind speed and temperature with kilometer-scale vertical resolution at integration times on the order of minutes [264]. Fe resonance lidar has been deployed to polar research stations and used to study gravity waves; there is current interest in developing spaceborne Fe lidar systems for global monitoring of wind and temperature

---

[13] At an altitude of $80 - 110$ km. The iron is primarily produced by the ablation of meteors.

[265, 266]. Measured frequency shifts in the captured fluorescence can be used to infer wind speed. At 372 nm, a velocity of 1 meter per second corresponds to a 2.69 MHz frequency shift. Fe Boltzmann temperature lidar infers temperature from the thermal Doppler width, which is of order 10^9 Hz (FWHM) for the approximately 200 K temperature of the mesosphere [267, 268]. We employ an analogous technique to estimate the temperature of iron atoms scattered from a surface in Section 4.3.

2.3.2 Isotope shifts

Isotopes of the same element exhibit small shifts in the frequencies of atomic transitions. These shifts arise from differences in nuclear mass and nuclear charge distribution between isotopes. For two isotopes A and A', the isotope shift can be attributed to two effects:

$$\delta v^{A,A'} = v^{A'} - v^{A} = \delta v_{\mathrm{MS}}^{A,A'} + \delta v_{\mathrm{FS}}^{A,A'} \tag{2.21}$$

Here, δv_{MS} is the mass shift, which is due to nuclear recoil and correlated electron motion, and δv_{FS} is the field shift, due to the finite nuclear volume and charge distribution [269]. The mass shift is further subdivided into the so-called normal mass shift (NMS) and specific mass shift (SMS). Because the nucleus has finite mass, the atom's center of mass moves, and the reduced mass modifies the electron kinetic energy. For a one-electron atom, the reduced mass correction gives:

$$E_n = -\frac{\mu e^4 Z^2}{2\hbar^2 n^2}, \qquad \text{where } \mu = \frac{m_e M}{m_e + M} \tag{2.22}$$

Expanding in $m_e/M \ll 1$, the normal mass shift is given by:

$$\delta v_{\mathrm{NMS}}^{A,A'} = v_0 m_e \left(\frac{1}{M_{A'}} - \frac{1}{M_A} \right) \tag{2.23}$$

which is proportional to the transition frequency itself. This term is usually small but can be significant for light atoms. In multi-electron atoms, the electrons' motions are correlated through the nuclear recoil operator:

$$H_{\text{recoil}} = \frac{1}{2M} \sum_{i,j} \mathbf{p}_i \cdot \mathbf{p}_j \tag{2.24}$$

The cross terms ($i \neq j$) lead to an additional specific mass shift:

$$\delta v_{\text{SMS}}^{A,A'} = \frac{K_{\text{SMS}}}{M_{A'}} - \frac{K_{\text{SMS}}}{M_A} \tag{2.25}$$

where $\mathrm{K_{SMS}}$ depends on the electronic configuration, particularly electron correlation. Unlike the NMS, the SMS cannot be inferred from the frequency alone and must be measured or computationally estimated. The total mass shift is:

$$\delta v_{\text{MS}}^{A,A'} = (K_{\text{NMS}} + K_{\text{SMS}}) \left(\frac{1}{M_{A'}} - \frac{1}{M_A} \right)$$

with $K_{\text{NMS}} = \nu_0 m_e$. The field shift arises because different isotopes have slightly different nuclear charge radii, $\langle r^2 \rangle$. To first order in perturbation theory:

$$\delta v_{\text{FS}}^{A,A'} = F\delta \left\langle r^2 \right\rangle^{A,A'} \tag{2.26}$$

where F is the field shift constant, which depends on electron density at the nucleus, and $\delta \left\langle r^2 \right\rangle^{A,A'} = \left\langle r^2 \right\rangle_{A'} - \left\langle r^2 \right\rangle_A$ [270]. Heavier isotopes generally have redshifted transitions, though the direction of shift can depend on the specific orbital mixing. King plots are made by plotting the isotope shifts of one transition against another:

$$\delta v_i^{A,A'} = a + b\delta v_j^{A,A'} \tag{2.27}$$

The plot's slope gives the ratio of field shift constants F_i/F_j, and its intercept gives the mass shift. The total frequency shift between isotopes A and A' can be expressed as:

$$\delta v^{A,A'} = \underbrace{(K_{\text{NMS}} + K_{\text{SMS}}) \left(\frac{1}{M_{A'}} - \frac{1}{M_A} \right)}_{\text{mass shift}} + \underbrace{F\delta \left\langle r^2 \right\rangle^{A,A'}}_{\text{field shift}} \tag{2.28}$$

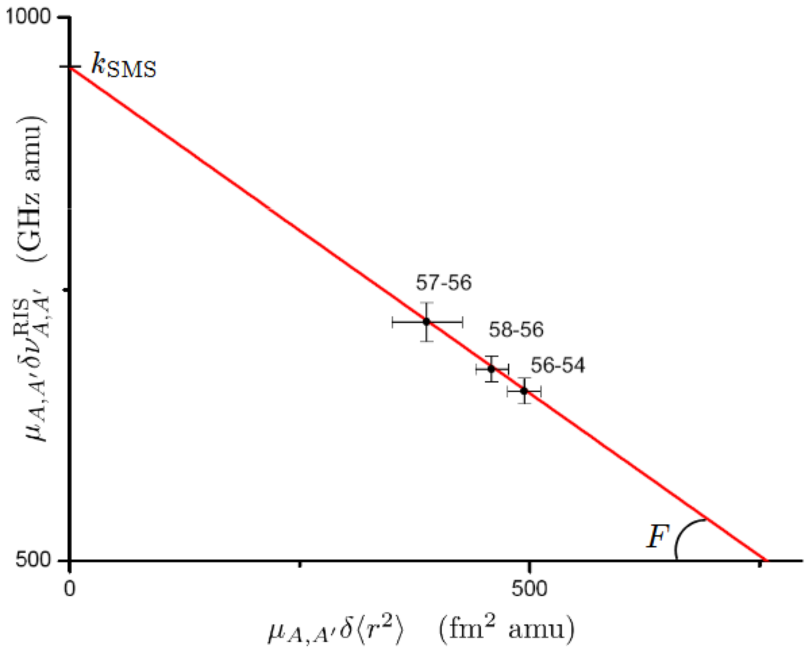

Figure 2.15: King plot for the 372 nm transition of iron. The origin value and slope of the linear regression line yield the specific mass shift K_{SMS} and field shift F coefficients, respectively [259].

For isotopes with nonzero nuclear spin, $I \neq 0$, additional hyperfine interactions appear in the Hamiltonian. These interactions split each fine-structure level into hyperfine sublevels labeled by $F = I + J,\ I + (J - 1),\ \ldots\ ,\ |I - J|$. The hyperfine energy splittings are given by:

$$E_{\mathrm{hfs}} = \frac{1}{2}AK + B\frac{3K(K+1) - 4I(I+1)J(J+1)}{8I(2I-1)J(2J-1)} \tag{2.29}$$

where K = $F(F+1) - I(I+1) - J(J+1)$. The constant A is given by:

$$A = \frac{\mu_0}{4\pi}\frac{2}{IJ}g_I\mu_N g_J\mu_B \left\langle r^{-3}\right\rangle_{n,l,j} \tag{2.30}$$

and B is proportional to the nuclear electric quadrupole moment Q. These terms depend explicitly on the nuclear spin and electromagnetic moments, not on M or

$\langle r^2 \rangle$. If two isotopes have different nuclear spins or moments, which they typically do, their hyperfine splittings differ and this produces additional isotope-dependent shifts of the hyperfine centroid. This is known as the Bohr-Weisskopf effect, or hyperfine anomaly.

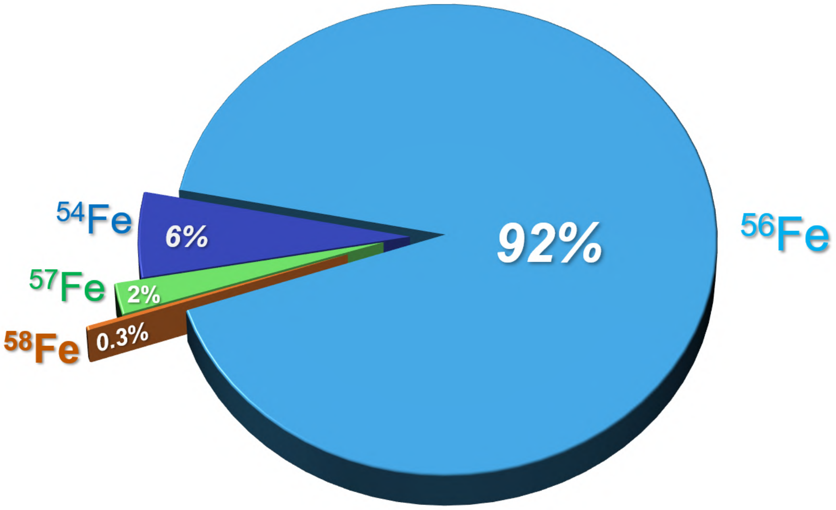

Figure 2.16: Relative abundances of the naturally-occurring stable isotopes of iron.

Iron has four naturally occurring stable isotopes: ^{54}Fe (5.82%, I = 0), ^{56}Fe (91.18%, I = 0), ^{57}Fe (2.1%, I = 1/2), ^{58}Fe (0.28%, I = 0). Only ^{57}Fe has hyperfine structure. The isotope shifts, relative to ^{56}Fe, are [259]:

$$\begin{aligned} \delta v_{58,56} &= 689.9 \text{ MHz} \\ \delta v_{57,56} &= 365.1 \text{ MHz} \\ \delta v_{54,56} &= -726.5 \text{ MHz} \end{aligned} \tag{2.31}$$

A King plot (see Fig. 2.15) gives the specific mass shift coefficient: $K_{\text{SMS}} = 950$ GHz · amu, and field shift coefficient $F = -0.60$ GHz/fm^2. For the 372 nm transition of iron, the specific mass shift is the largest contributor to the overall isotope shift. Only ^{57}Fe has non-zero nuclear spin, $I = \frac{1}{2}$, so its line is split into three hyperfine components, with relative intensities of 100 : 81.5 : 1.9 [259]:

$$
\begin{aligned}
&(1)\ F=\frac{9}{2}\rightarrow F'=\frac{11}{2}:+493.17\text{MHz}\\
&(2)\ F=\frac{7}{2}\rightarrow F'=\frac{9}{2}:+215.23\text{MHz}\\
&(3)\ F=\frac{9}{2}\rightarrow F'=\frac{9}{2}:+43.87\text{MHz}
\end{aligned}
\tag{2.32}
$$

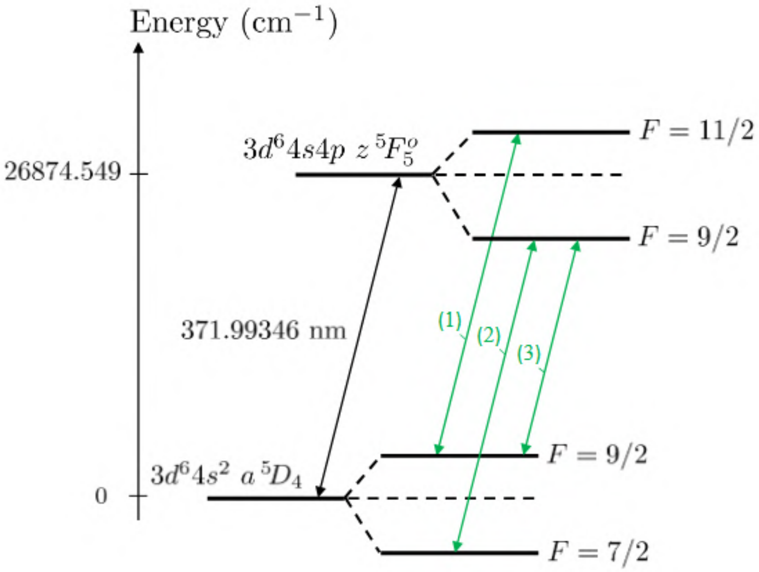

Figure 2.17: Hyperfine structure components (1), (2), and (3) of the $3d^64s^2a^5D_4 - 3d^64s4pz^5F_5^o$ Fe I transition at 372 nm for the isotope ^{57}Fe. Image credit: [259].

2.3.3 Collimation and Doppler broadening

Doppler broadening, the apparent widening of spectral lines due to atomic motion, is often the main factor limiting the resolution of laser spectroscopy. In laser isotope spectroscopy, the Doppler-broadened linewidth is typically substantially greater than the isotope shifts, obscuring individual isotope peaks. From:

$$\Delta v_{\text{FWHM}} = \frac{v_0}{c}\sqrt{\frac{8k_BT\ln 2}{m}} \tag{2.33}$$

for atomic iron at 1400 K, the thermally broadened 372 nm line is 2.89 GHz . As a point of comparison, the entire distribution of isotope peaks from ^{54}Fe to ^{58}Fe is less than 2 GHz; hence, the individual peaks become lost in the thermally broadened spectrum.

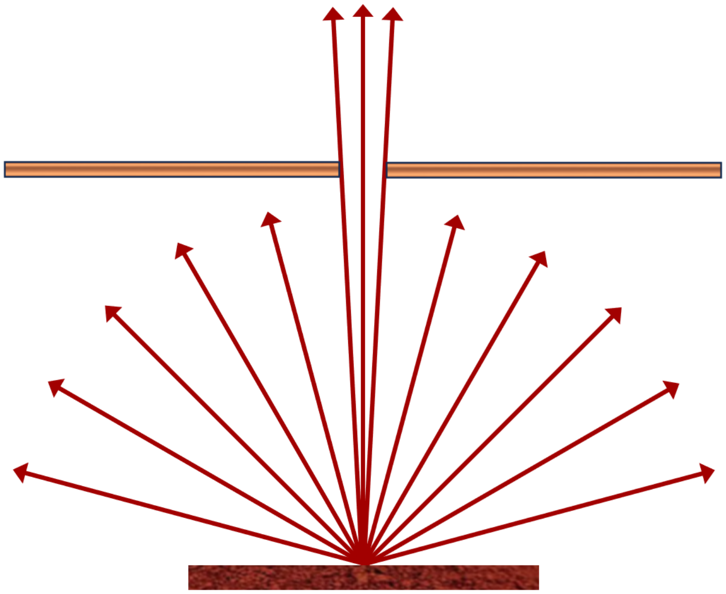

Figure 2.18: The velocity-selection effect of collimation on a point source.

This broadening is due to the distribution of atom velocity components transverse to the laser direction, producing shifts in the resonant frequency of the atoms in the laboratory frame. One of the simplest and most effective means for reducing Doppler broadening is collimation, which physically rejects trajectories with significant transverse velocity components. A thin circular aperture of radius a placed a distance d downstream of an effusive source accepts a cone of trajectories with half-angle

$$\theta_{\max} = \arctan(\frac{a}{d}) \approx \frac{a}{d} \qquad (a \ll d). \tag{2.34}$$

In angle space (θ_x, θ_y) this acceptance is a disk of radius $\theta_{\max}$ with uniform density. For a uniform disk, the variance of either component is

$$\left\langle \theta_x^2 \right\rangle = \left\langle \theta_y^2 \right\rangle = \frac{\theta_{\text{max}}^2}{4}. \tag{2.35}$$

For an effusive beam, $\left\langle v^2 \right\rangle = \frac{4kT}{m}$. Using the small angle approximation that speed v and angle θ_x are independent, the transverse component along the laser direction is:

$$\left\langle v_x^2 \right\rangle = \left\langle v^2 \right\rangle \left\langle \theta_x^2 \right\rangle = \frac{4kT}{m} \cdot \frac{\theta_{\text{max}}^2}{4} = \frac{kT}{m}\theta_{\text{max}}^2 \tag{2.36}$$

A probe laser crossing the atom beam at 90° is sensitive to v_x. Approximating the central line shape as Gaussian, the Doppler FWHM is

$$\Delta v_{\text{D},\perp} = 2\sqrt{2\ln 2}\frac{1}{\lambda}\sqrt{\frac{kT}{m}}\theta_{\text{max}} \tag{2.37}$$

and with $\theta_{\text{max}} \approx a/d$,

$$\Delta\nu_{\text{D},\perp} \approx 2\sqrt{2\ln 2}\frac{1}{\lambda}\sqrt{\frac{kT}{m}}\frac{a}{d}. \tag{2.38}$$

Collimation introduces a flux vs. SNR trade-off: For $\theta_{\text{max}} \ll 1$, the accepted solid angle is $\Omega \approx \pi\theta_{\text{max}}^2$. The transmitted fraction of flux f, compared to the total emission into a 2π radian hemisphere, is given by:

$$f \approx \frac{\Omega}{2\pi} \simeq \frac{\theta_{\text{max}}^2}{2} \propto \left(\frac{a}{d}\right)^2. \tag{2.39}$$

This illustrates that halving the Doppler broadening via changes in a or d reduces flux by approximately a factor of 4.

The collimating aperture for our LIF setup was created by mounting a thin copper plate with a 1 mm diameter through-hole or slit to the top of the crucible. The formula for the Doppler FWHM for a slit of width s is analogous to that for a circular aperture:

$$\Delta\nu_{\text{D,slit}} \approx \frac{2\sqrt{2\ln 2}}{\sqrt{3}}\frac{1}{\lambda}\sqrt{\frac{kT}{m}}\frac{s}{d} \tag{2.40}$$

For the geometry used in these experiments, the Doppler width of the collimated iron atom beam was $\Delta\nu_{D,\perp} \approx 57\text{MHz}$ (FWHM), small enough to resolve all of the isotope peaks.

2.3.4 Optical setup

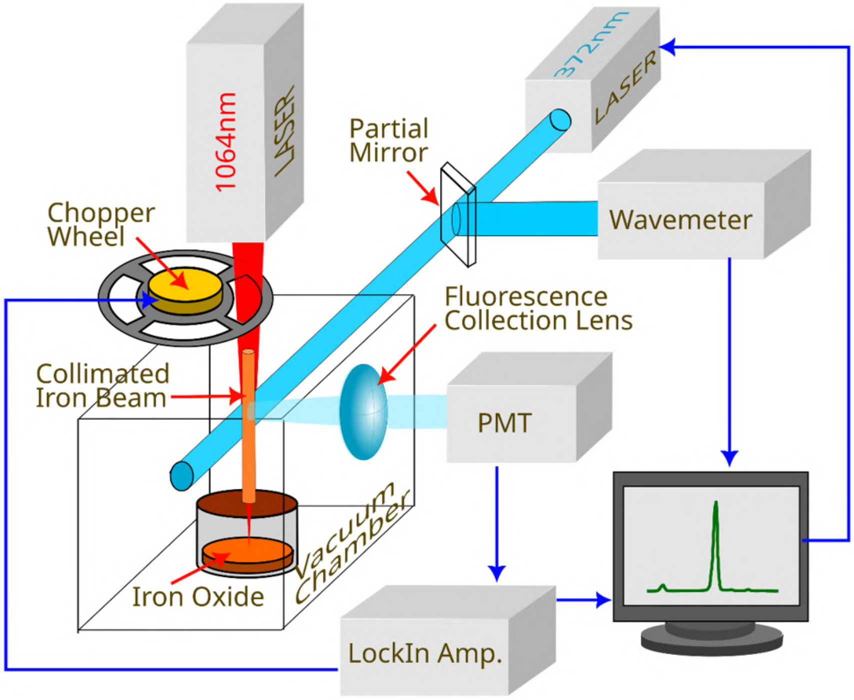

Figure 2.19: Optical setup for iron isotope spectroscopy.

Fig. 2.19 shows a schematic of optical setup of our iron isotope spectroscopy system.

The sample-containing crucible was placed in vacuum, and then ablated using an IPG CW fiber-coupled 1064 nm YAG at 1-2 W. The IR ablation laser was focused on the powder surface through an aperture in the top plate, and mechanically chopped, improving the stability of the fluorescence signal from the ablated iron. This collimated-angled beam was crossed perpendicularly by a CW probe laser, tuned to the 372 nm transition of iron $(a^5\text{D}_4 \rightarrow {}^5z\text{F}^\circ_5)$. The excitation laser was

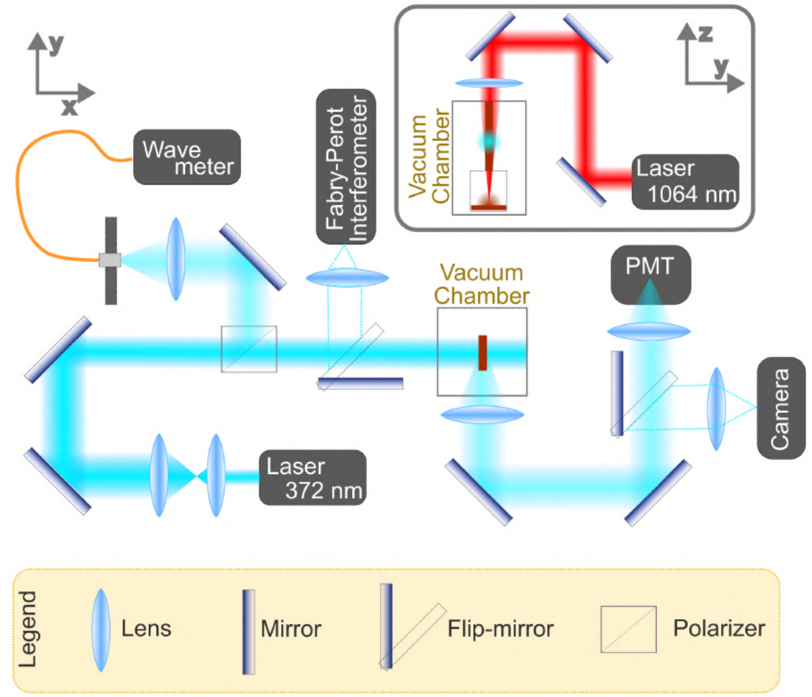

Figure 2.20: Optical diagram for iron isotope spectroscopy.

locked to a wavemeter, with computer control of the laser tuning parameters via a custom LabVIEW program. The resulting 372 nm fluorescence was collected and focused onto a photomultiplier tube (PMT), and the PMT signal was then fed into a lock-in amplifier using the chopper wheel as a reference.

Fig. 2.20 shows a schematic representation of the relay system for the spectroscopy setup. The 372 nm light from a Toptica external cavity diode laser (ECDL) is first expanded with a telescope. Afterwards, a small portion of light is picked off and fed to a HighFinesse wavemeter to lock the laser to the 372 nm transition. A Fabry-Perot interferometer can be toggled with a flip mirror, allowing imaging of the laser's mode shape. The laser induced fluorescence shows some sensitivity if the mode is not clean. The excitation laser passes through the vacuum chamber, crossing the iron atomic beam perpendicularly. At a right angle to the excitation laser's direction of travel, a collection lens gathers light from the iron atomic fluorescence, which is relayed along mirrors and focused onto the photomultiplier tube for analysis. A flip mirror in this section, which toggles a video camera and lens, facilitates the alignment of the optics. The camera is aligned so that it “sees” what is focused on the PMT; flipping to it greatly assists the correction of misalignment in the optical setup.

2.4 Results

Pictured in Fig. 2.21 is a recent spectrum from a 150 μg sample of whole blood, processed with our ashing techniques. All isotope signatures are resolved, including the hyperfine splitting of ^{57}Fe. Reading relative isotope abundances from peak height ratios, the results are in line with expected natural isotopic abundances. This spectrum was taken in a single rapid pass as a proof-of-principle, and future iterations will pass repeatedly over the isotope resonances to improve the accuracy of the measurement.

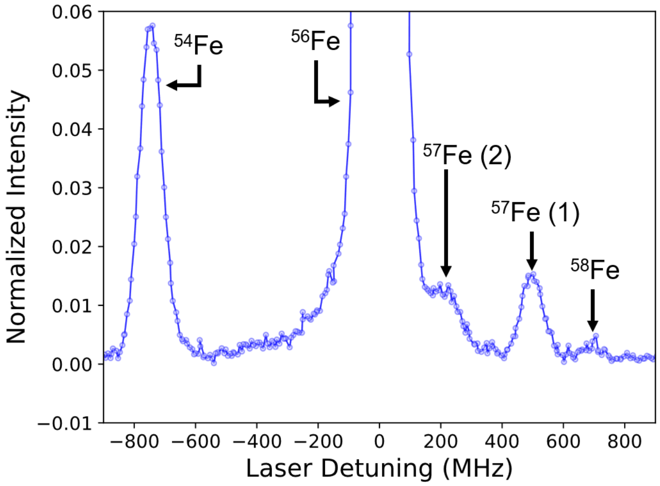

Isotopes	Abundance	Peak Analysis
^{54}Fe	5.8%	5.3%
^{56}Fe	91.8%	92.4%
^{57}Fe	2.1%	2.0% (0.6+1.4)
^{58}Fe	0.3%	0.3%

Figure 2.21: Iron isotope spectrum from 150 μg blood microsample.

Chapter 3: Stable Isotope Separation for Medicine

3.1 Calutrons: the old method

Figure 3.1: Calutron operators at the Y-12 plant, 1944. Sign: "*Do not visit with cubicle operators*" [271].

.

The main barrier to realizing the many applications of isotopes is the difficulty of separating them from each other. The two most widely employed devices for isotope separation are the gas centrifuge and the calutron. However, gas centrifuges can only be employed for the few elements in the periodic table that have gas-phase compounds at room temperature [272]. Calutrons, by contrast, are one of the most broadly applicable devices for separating isotopes.

3.1.1 The U.S. calutron program

Calutron separation is one of a group of methods known as electromagnetic isotope separation (EMIS). While EMIS methods are well-established, they are energy intensive, due to the large magnetic field they generally require over the entire ionization volume. In the United States, large-scale electromagnetic separation infrastructure was first built for uranium enrichment in the Manhattan Project. The Y-12 plant at Oak Ridge, Tennessee, used calutrons in racetrack arrangements to separate fissile ^{235}U from ^{238}U [273]. After the Manhattan Project ended in 1946, the newly formed US Atomic Energy Commission (AEC) retained Y-12 and Oak Ridge National Laboratory (ORNL) to carry out isotope separation and distribution. The AEC announced the "Isotope Distribution Program" that year, making both radioisotopes and stable isotopes available to qualified researchers. The operating group at Oak Ridge handling the non-radioactive separations was known internally as the Isotopes Section, with facilities in the Y-12 plant [274].

Figure 3.2: Calutron alpha "racetrack." Y-12 facility, 1944. [275].

.

By the early 1950s, isotope work had "become a permanent part of ORNL's scientific mission [276]." To reflect this, the Isotopes Section was formally retitled the Isotope Research and Production Division (IRPD), with dual isotope production and R&D roles. In addition to the task of isotope separation, ORNL developed isotope handling infrastructure, including hot cells, vacuum furnaces, purification labs, and chemical conversion labs to convert separated material into useful chemical forms, such as oxides and salts [276]. The stable isotope program at ORNL continued to expand; by the mid-1950s, the US was capable of producing enriched isotopes of all naturally occurring stable elements[1] via calutron [277]. The program was not high throughput, but production levels were sufficient for research and other specialized uses, from milligram up to kilogram scale for some isotopes [277]. The program offered over 230 distinct enriched stable nuclides between 1945 and 1998 [278]. Due to the substantial electrical power consumption of calutrons, heavier elements and highly enriched samples were expensive; prices for stable isotopes ranged from $\$1000$ to $\$4,000,000$ per gram [279]. In the 1960s, the Stable Isotope Program expanded, and separation campaigns[2] for multiple isotopes became routine; for example, in 1970, ORNL was producing kilogram quantities of $\sim 85\%$ enriched ^{57}Fe for neutron-polarizer crystals [273, 280].

3.1.2 Isotope supply issues

As US government support for the calutron program waned in the 1990s, stable isotope production declined. The stable isotope inventory that had been produced over the decades was stored and managed as a strategic reserve. As new separation runs became less frequent, those reserves were drawn down. Although the calutron program was unique in the range of isotopes produced, it was expensive to operate, energy-intensive, and limited in throughput. Operating costs increased over time due to aging magnets, recurring issues with vacuum seals, and infrastructure degradation.

---

[1] Except for osmium, which was added around 1960.

[2] Term of art for isotope production runs.

Figure 3.3: Calutrons used at ORNL for stable isotope separation through 1998 [281].

.

In 1998, ORNL calutron operations ceased altogether. The national repository of enriched stable isotopes gradually became depleted, and some isotopes became scarce or unavailable from US sources [277]. Foreign suppliers, most notably Russia, began supplying certain enriched stable isotopes at lower cost. Near total dependence on subsidized Russian machines created a fragile supply chain [282].

Following the shuttering of the US calutron program, stable isotopes were treated as a commodity, rather than a strategic resource. The Department of Energy (DOE) Isotope Program focused on radioisotope production for medical uses, rather than operating full-spectrum separation infrastructure. Private firms such as Cambridge Isotope Laboratories and ISOTEC largely supplied the market for stable isotopes, particularly labeled molecules and light elements, often sourcing feedstock internationally. DOE documents in the 2000s and 2010s highlighted vulnerabilities: some critical stable isotopes such as ^{98}Mo, ^{100}Mo, ^{76}Ge, and ^{96}Ru had no domestic suppliers, and US production capabilities were insufficient to replace them if needed [283, 284]. In response, DOE began limited investments in advanced isotope separation technologies, such as improved EMIS, small gas-centrifuge isotope separation (GCIS) for stable isotopes, and plasma separation processes (PSP) [285, 286, 287, 288].

In the past decade, recognizing geopolitical supply risks and increasing demand from medicine and quantum technology, the US has made concerted moves to regain stable isotope enrichment capability. DOE is building a modern facility, the Stable Isotope Production and Research Center (SIPRC), at ORNL. The formal contract for $88.8 million was awarded in November 2024; construction is expected to be completed in spring 2027 [289]. SIPRC is designed to allow the enrichment of stable isotopes from across the periodic table, using both EMIS and gas centrifuge separation. In parallel with SIPRC, ORNL has also created the Stable Isotope Production Facility (SIPF), which is intended to produce priority isotopes, such as ^{129}Xe for medical imaging, with the aim of reestablishing domestic production capacity [290, 291].

3.2 MAGIS/MRLIS

3.2.1 Failure of AVLIS to replace calutrons

The US government has invested in laser-based isotope separation schemes since the early 1970s, with the atomic vapor laser isotope separation (AVLIS) program being arguably the most prominent [293]. In the 1970s, laser-based separation emerged as a potentially energy-efficient, high-selectivity method: ^{235}U could be selectively ionized via laser, then separated via electromagnetic fields. This involves fewer stages than centrifugation or gaseous diffusion methods, uses much less power, reduces the complexity of material handling, and importantly, would be significantly cheaper [294, 295]. In addition to uranium enrichment, laser separation techniques could also be applied to other elements of interest, including plutonium, gadolinium,

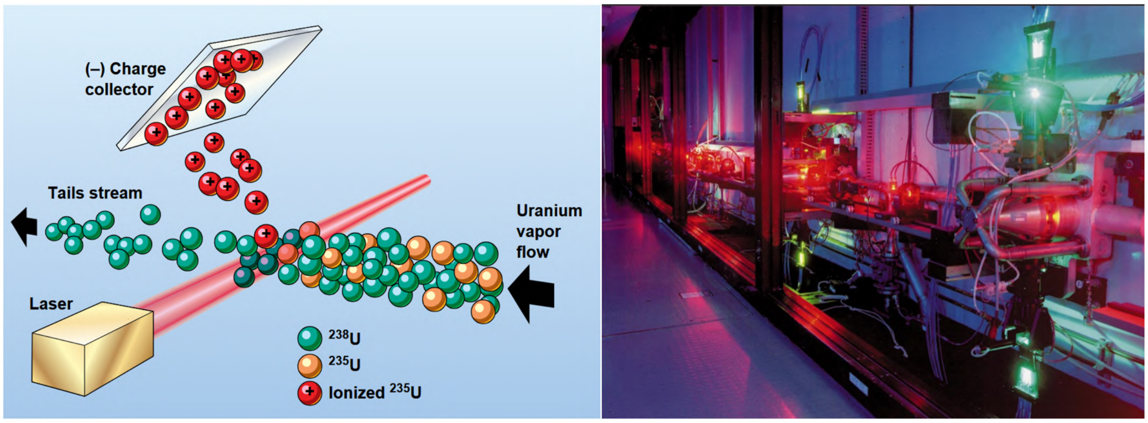

Figure 3.4: Left: schematic of U-AVLIS operation. Right: Dye laser corridor for a U-AVLIS setup at Lawrence Livermore National Laboratory (LLNL) in the 1990s. [292].

zirconium, and hafnium [296, 297, 298].

In June 1985, the US DOE formally selected U-AVLIS as its preferred advanced enrichment technology for the future [299]. The DOE envisioned that, after successful demonstration, production-scale AVLIS might begin as early as the mid-1990s. Plans were made for an AVLIS Production Plant at ORNL to integrate into the US enrichment infrastructure [300]. In 1992, under the Energy Policy Act, the US government established the United States Enrichment Corporation (USEC) to take over US uranium enrichment operations and future advanced technology development from DOE. In 1994, as part of a large federal technology transfer, the AVLIS process and associated rights were transferred to USEC for commercialization and deployment. After the privatization of USEC via IPO in 1998, the company became fully commercial, with responsibility for further development of AVLIS. However, the following year, USEC's board voted to indefinitely suspend further AVLIS development, largely due to projected marginal return on investment [301]. Even after the cancellation, USEC retained ownership of the AVLIS intellectual property. To date, the US has not operated AVLIS-based isotope production at commercial scale.

3.2.2 Difficulty of laser separation methods

Besides funding, the limiting technical factor in laser isotope separation technology has largely been the lasers themselves. Achieving the frequency stability, high power, and narrow linewidth needed for isotope separation at industrial scale is very difficult without loss of selectivity, efficiency, reliability, or prohibitive cost [302]. Previous work on laser separation of isotopes relied on multiphoton ionization with pulsed lasers [303]. In some variations, continuous-wave (CW) lasers were proposed and used to achieve isotopically selective optical pumping into metastable states, but the final step of laser-ionization was always accomplished with a pulsed nanosecond laser[304, 305, 306, 307]. However, there has recently been substantial progress in solid-state laser technology, providing robust platforms of tunable continuous-wave lasers at the several watt power levels. These include semiconductor diode lasers and vertical external cavity surface emitting (VECSEL) lasers [308, 309]. These new laser technologies offer possibilities for the development of alternative techniques of isotope separation that circumvent the astronomically high equipment and operating costs which have frustrated prior attempts to replace the calutron production of stable isotopes.

3.2.3 MAGIS

Magnetically activated and guided isotope separation (MAGIS), is a novel isotope separation technique developed by our group in earlier work, [310, 311]. It uses lasers to change how atoms respond to a magnetic field through a process known as magnetic-state optical pumping. Optical pumping is the process by which light acts on an atom to change its magnetic state, which determines how it will be affected by magnetic fields. The desired isotope can be optically pumped into either a "low- or high-field-seeking state" ($m_j > 0$ and $m_j < 0$, respectively). Desired isotopes are then separated using arrays of permanent magnets, which act as a guiding track. Because MAGIS relies on rare-earth permanent magnets, it does not consume

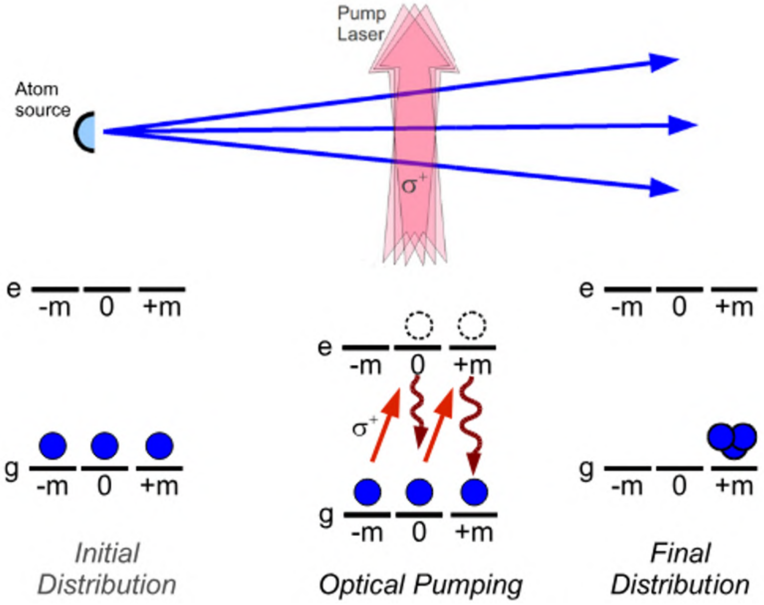

Figure 3.5: MAGIS magnetic-state optical pumping scheme. Here, atoms are being pumped into a low-field seeking state, ($m_j > 0$) [310].

much energy compared to the calutron. The principal energy requirements are for vaporization of the element in a crucible, and operation of the vacuum pumps and lasers[3][312, 313]. The MAGIS technique is currently being used to produce commercial quantities of ^{176}Yb at the high levels of enrichment needed for production of the radioisotope ^{177}Lu, which is used for cancer therapy [314].

The primary limitation of MAGIS is its dependence on the currently available strength of rare-earth permanent magnets. First, to reach the field strengths required for separation, the atoms must be collimated in one dimension to less than 20 mrad so that they may be aimed at grazing angles of incidence to the magnetic array. This collimation also reduces atomic flux. Laser cooling can brighten the beam considerably, but at the cost of much higher laser power [315, 316]. Second, scaling up production requires large magnetic arrays, precluding the application of MAGIS for

---

[3] Taken together, these are typically around three orders of magnitude smaller than electrical consumption by the calutron.

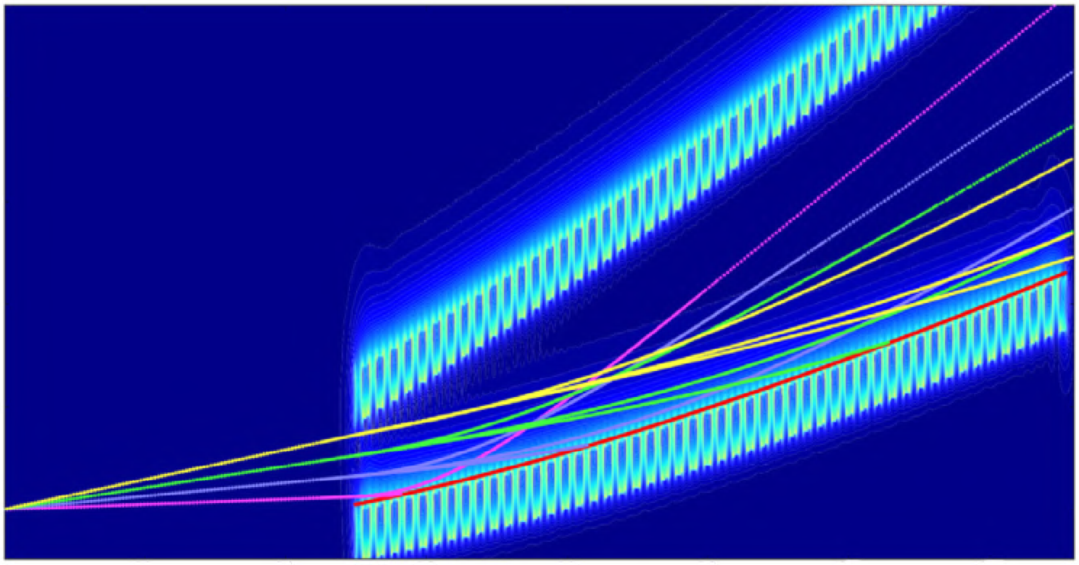

Figure 3.6: Simulation of MAGIS with trajectories from an effusive source, with atoms in low-field-seeking states. Velocities used are 500, 1000, and 1500 m s^{-1} [310].

separation of radioisotopes. The safe handling of radioisotopes, especially γ-emitters, requires a special enclosure that provides radiation shielding for operators together with robotic control, known as a hot cell [317]. The separation system would need to be containable within the interior dimensions of the hot cell.

3.2.4 MRLIS

We[4] have recently proposed a new method for isotope separation based on photoionization of atoms that should resolve the current limitations of AVLIS. The method, Multi-Resonant Laser Isotope Separation (MRLIS) is described in detail for a generic case, and then specifically for strontium isotope separation. Applications to both stable isotopes and radioisotopes, as an alternative to radiochemistry, are outlined. The overall sequence is not dissimilar to prior laser isotope separation methods: efficient ionization of the desired isotopes with lasers, followed by their

---

[4] This section adapts published work by Aaron Barr, Simon Rochester, Dmitry Budker, and Mark Raizen.

separation from the atomic beam with an electric field, and then collection. However, the approach used in the past for laser ionization relied on a fast sequence of high-intensity nanosecond pulsed lasers. The excitation of atoms from the ground state using resonant atomic transitions can be efficient, but the major limit on sample efficiency has been with the last step of photoionization. We propose to use continuous-wave lasers to drive atomic transitions, combined with long interaction time in ultra-large-volume resonant cavities. This new paradigm has many advantages, including the use of reliable solid-state lasers and very high predicted ionization efficiency. A schematic of the proposed setup is shown in Fig. 3.7. The first step in the process is excitation of the desired isotopes from their ground electronic state to an excited electronic state. This is not fundamentally different from what is done in AVLIS, especially with recent proposals to use CW lasers or time-delayed pulsed lasers to pump into a metastable atomic state [304, 305]. In some cases, a two-step excitation from the ground state should be employed, which can be driven efficiently using stimulated Raman adiabatic passage [318].

The last step is photoionization, which is typically non-resonant and requires a high-power pulsed laser. We propose to use an optical resonator to boost the laser power by a factor of at least 200. The experimental challenge with optical resonators is that the Gaussian waist scales as the product of cavity length and mirror radius of curvature to the 1/4 power [319]. The resulting beam waist is usually in the range of 100 microns, which would intersect only a small fraction of the atomic beam and result in low average ionization probability. One solution is to use a cavity with two flat mirrors and an intracavity lens, but the beam waist is on the order of several millimeters [320]. Alternatively, cavity mirrors with very large radius of curvature can be fabricated using thin-film deposition; a radius of curvature of 10 kilometers has been demonstrated in previous work [321]. However, by using flat mirrors, the radius of curvature can be made essentially infinite, for all practical purposes! Such a configuration is usually called an etalon, but in the past, it has been used with low-reflectivity coatings or none at all. Such a configuration with high-reflectivity

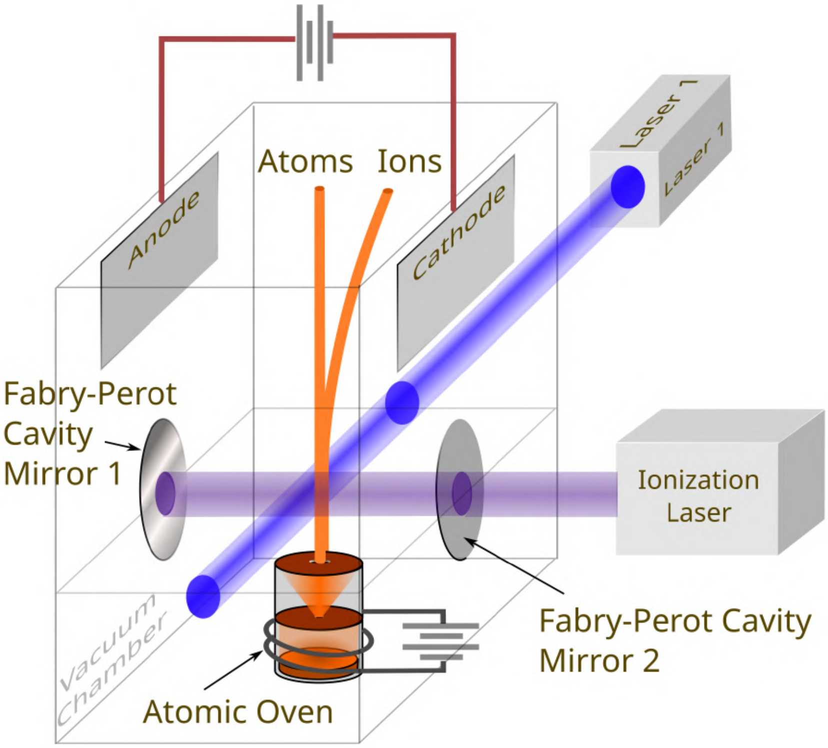

Figure 3.7: MRLIS schematic: an effusive atomic beam is produced by an atomic oven, with an excitation laser (shown here in blue) crossing the collimated atomic beam at right angles. The power of the CW ionizing laser (shown here in purple) is enhanced by a large mode-volume Fabry-Perot cavity. Ions of the desired isotope(s) are separated by an electrical field.

mirrors was first considered in [322], though applications to laser ionization were not proposed.

The only conditions for etalon cavity resonance is that there be a uniform phase front to the beam, and that the overall length of the cavity be an integer multiple of half-wavelengths. This can also be seen by the resonant frequencies of transverse modes, which are shifted from the fundamental resonances by integer multiples of $\cos^{-1}(1 - \frac{L}{R})$ where L is the cavity length and R is the radius of curvature. In the limit of infinite R, these frequency shifts are zero, so mode-matching is not required. High-finesse Fabry-Perot etalons effectively filter wavefront imperfections by rejecting spatial frequency components outside a narrow angular acceptance [323]. In practice, this means that fine-scale aberrations in the input laser beam are suppressed by the etalon, but, in exchange, the system requires precise control of mirror parallelism and alignment. The Rayleigh length of a laser beam is the distance over which the transverse radius increases by a factor of $\sqrt{2}$, and is proportional to the square of the minimum spot size divided by the wavelength. For example, a laser beam with a wavelength of 1 μm and a spot size of 6 cm has a Rayleigh length of about 3 km. If the mirror reflectivity is 99.9%, and the cavity length is 10 cm, then 1000 round-trips is only 100 m, and the beam does not expand significantly. A 10 W laser would produce an intracavity power of 10 kW. For comparison, the Laser Interferometer Gravitational-Wave Observatory (LIGO) routinely has a circulating power of that magnitude or higher [324]. To minimize absorption losses and heating of the coatings, near-infrared wavelengths longer than 800 nm are optimum.

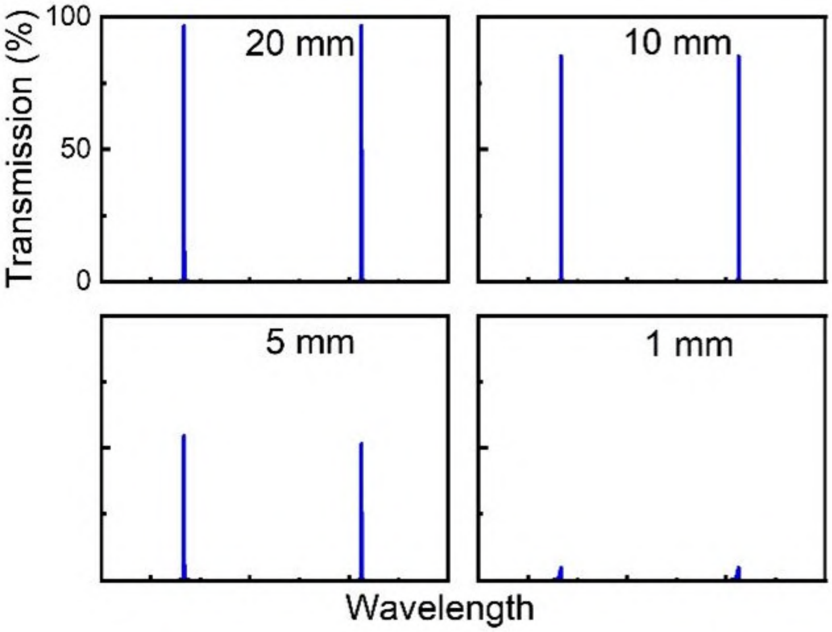

Figure 3.8: Numerical simulation of transmission coefficient of a cavity of 5 cm length and mirror reflectivity of 99.9%. The spot size is changed from 20 mm to 1 mm.

To test the above hypothesis, we performed numerical simulations and the results are shown in Fig. 3.8. The figures show the cavity transmission as the wavelength is scanned; alternatively, the length of the cavity can be changed, and resonances occur for a half-wavelength change. We assume that mirror transmission is $T = 1 - R$, which is justified when scatter and absorption losses are much smaller than transmission. A cavity transmission of unity is expected for a plane wave, and the intracavity circulating power is boosted by a factor of $1/T$. For mirrors with 99% reflectivity, transmission is not affected by the spot size unless it is less than 5 mm. In the case of mirrors with 99.9% reflectivity, the spot size must be larger than 20 mm. These numerical results agree with the heuristic arguments above. Further details on the method of numerical simulation are discussed in Sections 3.2.5 and 3.2.6.

3.2.5 Large mode volume cavity simulation

Cavity transmission for a Gaussian beam propagating in a Fabry-Perot etalon was numerically modeled using open-source MATLAB code [322]. The cavity mirror spacing was set at 50 mm, with incident beam spot sizes modeled in a range from 20 mm to 1 mm. Results are computed for both 99% and 99.9% etalon mirror reflectivity. Results for the propagation of incident plane waves in the etalon are also calculated. For a given etalon, transmission as a function of wavelength is characterized by its interferometer transfer function (ITF):

$$\mathrm{ITF}(\lambda) = \frac{I_{\text{out}}\left(\lambda\right)}{I_{\text{in}}\left(\lambda\right)}\,, \tag{3.1}$$

where I_{in} is the intensity of light incident on the etalon, and I_{out} is the intensity of light exiting the etalon. The outgoing intensity can be found by the spatial integration of the outgoing field

$$I_{\text{out}} = \int_0^\infty \left|U_{\text{out}}\left(r, z\right)\right|^2 2\pi r dr\,, \tag{3.2}$$

where r is the radial axis and z is the optical axis, in the direction of the incoming beam. The total outgoing field is the sum of contributions by exiting beams that have made m round trips between the cavity mirrors, where $m = 0, 1, 2, \ldots$ For incident plane waves, these partial beams are expressible as a geometric series, and their sum by an Airy function.

Incident Gaussian beams require a more general approach. Here, we use the method of ray transfer matrix analysis, which allows the performance of ray tracing calculations in cases where the paraxial approximation is valid. In this method, a 2×2 ray transfer matrix (sometimes called an ABCD matrix), operates on a vector representing an incoming light ray, yielding a new vector representing the outgoing ray

$$\begin{bmatrix} q_{\text{out}} \\ 1 \end{bmatrix} = k \begin{bmatrix} A & B \\ C & D \end{bmatrix} \begin{bmatrix} q_{\text{in}} \\ 1 \end{bmatrix} . \tag{3.3}$$

Here, k is a normalization constant, and q is the complex beam parameter defined by

$$\frac{1}{q} = \frac{1}{R} - i\frac{\lambda}{\pi n w^2} , \tag{3.4}$$

where R is the Gaussian beam radius of curvature, w is its Gaussian waist size, n is the index of refraction of the material through which the beam is passing, and λ is its wavelength. Because ABCD matrices are linear operators, matrices representing each optical element in a system can be multiplied together to give a single resultant matrix representing the system as a whole

$$M = M_N M_{N-1} \cdots M_2 M_1 . \tag{3.5}$$

Modeling a vacuum spaced etalon requires three different kinds of ABCD matrix. First is M_{refr}, representing the refraction of a ray either entering or exiting the etalon

$$M_{\text{refr}} = \begin{bmatrix} 1 & 0 \\ 0 & n_1/n_2 \end{bmatrix} , \tag{3.6}$$

where n_1 is the index of refraction in the initial medium and n_2 is the index of refraction in the final medium. The second ray-transfer matrix is M_{prop}, which represents the propagation of rays through a homogeneous medium

$$M_{\text{prop}} = \begin{bmatrix} 1 & h/n \\ 0 & 1 \end{bmatrix} , \tag{3.7}$$

here h is the distance propagated (in this case, the mirror-to-mirror distance), and n is the index of refraction of the medium propagated through (vacuum, so here $n = 1$). Third and last is M_{refl}, which gives the reflection of rays from a planar surface:

$$M_{\text{refl}} = \begin{bmatrix} 1 & 0 \\ 0 & 1 \end{bmatrix} . \tag{3.8}$$

Conceptually, it is natural to model the propagation of the beam through the etalon in three parts: M_{in}, in which a ray enters the etalon through the first mirror, M_{cav}, in which the ray bounces back and forth between the cavity mirrors, and finally M_{out}, in which the ray exits the etalon. M_{in} only involves refraction by the first mirror:

$$M_{\text{in}} = M_{\text{refr}} . \tag{3.9}$$

For M_{cav}, consider the constituent matrices of a round trip through the interior of the etalon: 1) propagation through the interior to the surface of the second mirror, 2) reflection from the second mirror's surface, 3) propagation back to the first mirror, and 4) reflection from the first mirror's surface. In matrix form:

$$M_{\text{cav}} = M_{\text{refl}}^{\leftarrow} \, M_{\text{prop}}^{\leftarrow} \, M_{\text{refl}} \, M_{\text{prop}} . \tag{3.10}$$

The matrix M_{out}, representing the ray transmitted through the cavity, is comparatively straightforward: propagation to the second mirror surface, followed by refraction through the second mirror to exit the etalon

$$M_{\text{out}} = M_{\text{refr}} \, M_{\text{prop}} . \tag{3.11}$$

Now, M_{in} and M_{out} occur exactly once for each transmitted ray, but the number m of round trips within the cavity can be any non-negative integer, so the overall system matrix for any possible transmitted ray has the form

$$M = M_{\text{out}} \left(M_{\text{cav}}\right)^m M_{\text{in}}. \tag{3.12}$$

From this system matrix, the transmitted field can be computed from the relation

$$U_{\text{out}}\left(r, z; M\right) = \frac{1}{A + B/q\left(z_{\text{in}}\right)} \exp\left(-ik \frac{r^2}{2q\left(z_{\text{out}}\right)}\right) , \tag{3.13}$$

where z_{in} and z_{out} are the axial positions at the entrance and exit of the etalon, respectively.

The ABCD ray-tracing model does not capture changes in field amplitude, so that must be included in the final summation of contributions to the field from all transmitted beams

$$U_{\text{out}}\left(r, z\right) = \sum_{m=0}^{\infty} A_m U_{\text{m}}, \quad A_m = t_1 t_2 \left(r_1 r_2\right)^m \ . \tag{3.14}$$

Here, t_1,t_2, and r_1,r_2 are the transmittivity and reflectivity coefficients of the first and second mirrors. The above provides a method to compute the ITF for any chosen wavelength, given the incoming beam spot and waist size, the indices of refraction for intra- and extracavity material, the mirror-to-mirror spacing, and the reflectivity of each mirror. While the number of cavity round trips m used in computing the transmitted field ranges from zero to infinity, because the partial field contribution becomes smaller and smaller for higher-m terms, the number of computed round trips can be truncated at a finite value. This truncation was chosen by considering the output ITF values to have converged once the most recent term changes the overall transmitted field amplitude by $< 0.001\%$, typically $m \sim 100$. To capture fine details, 10^3 points/nm were computed in the vicinity of the transmission peaks, with 10^2 points/nm in the inter-peak region. The plane wave computations were performed by setting the spot size to several orders of magnitude larger than the cavity dimensions.

3.2.6 Non-parallelism/incidence angle effects

If the input laser beam is tilted at an angle θ_t relative to the etalon, each successive reflection inside the etalon is slightly displaced. This displacement is called walk-off. The walk-off per round trip is

$$\Delta_{\text{walk}} = 2d \tan\theta_t \, . \tag{3.15}$$

As the beam is displaced by Δ_{walk} relative to the previous pass, the overlap between the two profiles is reduced. The normalized field overlap between $u(r)$ and a displaced

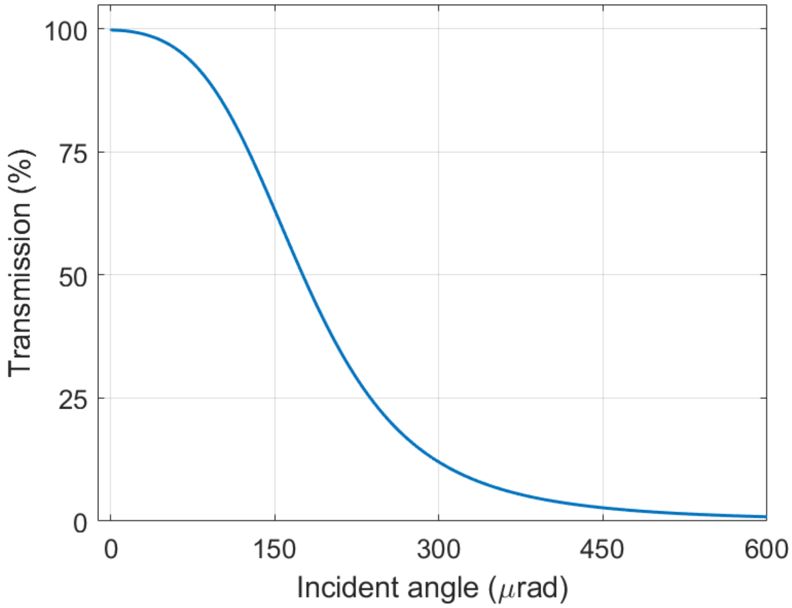

Figure 3.9: Numerical simulation of the effect of laser beam incidence angle on cavity transmission. Cavity is 5 cm in length, mirror reflectivity is 99%, and laser spot size is 10 mm.

copy $u(r-\Delta)$ is given by:

$$\eta_{\text{overlap}}\,(\Delta)=\frac{\left|\iint u(\mathbf{r})u(\mathbf{r}-\Delta)d^2r\right|}{\sqrt{\iint|u(\mathbf{r})|^2d^2r\iint|u(\mathbf{r}-\Delta)|^2d^2r}}\,, \tag{3.16}$$

where

$$u(\mathbf{r})=\exp\left(-\frac{r^2}{w_0^2}\right) \tag{3.17}$$

and w_0 is the beam waist. Making the reasonable assumption that both beams have the same width and power, the above simplifies to

$$\eta_{\text{overlap}}(\Delta)=\exp\left(-\frac{\Delta_{walk}^2}{2w_0^2}\right)\,. \tag{3.18}$$

For the m-th round trip, this amplitude field factor becomes

$$a_{\text{mode}}\,(m)=\exp\left(-\frac{\left(m\Delta_{\text{walk}}\,\right)^2}{2w_0^2}\right)\,. \tag{3.19}$$

After a number of round trips, the beam will begin to walk off the mirror entirely. The power fraction of an offset 2D Gaussian that passes through a circular aperture of radius a is given by the formula

$$P_{\text{pass}}\left(\Delta\right) = \frac{2\pi}{\pi w_0^2/2} \int_0^a r e^{-\frac{2\left(r^2+\Delta^2\right)}{w_0^2}} I_0\left(\frac{4r\Delta}{w_0^2}\right) dr \,, \tag{3.20}$$

where I_0 is a modified Bessel function [325]. The corresponding field amplitude factor is $a_{\text{ap}}(\Delta) = \sqrt{P_{\text{pass}}(\Delta)}$. The transmitted field summed over m round trips is

$$E_{\text{out}}\left(\lambda, \theta\right) = t^2 \sum_{m=0}^{m_{\max}} a_m \left(r^2 e^{i\delta}\right)^m \,, \tag{3.21}$$

where $t = \sqrt{1-R}$ is the transmission amplitude, $r = \sqrt{R}$ is the reflection amplitude, $a_m = a_{\text{mode}}\left(m\right) \cdot a_{\text{ap}}\left(m\right)$ is the combined Gaussian overlap and aperture loss factors, and $m_{\max}$ is chosen so that additional round trips no longer significantly contribute to the sum. δ is the single round-trip optical phase shift

$$\delta = \frac{2\pi}{\lambda} \cdot \left(2nd\cos\theta_t\right) , \tag{3.22}$$

where n is the refractive index of the intracavity medium and d is the physical distance between the etalon mirrors. The transmission T is given by

$$T(\lambda, \theta) = \left|E_{\text{out}}\right|^2 . \tag{3.23}$$

If the input laser beam is instead normally incident on the etalon, but one of the mirrors has a small tilt θ relative to the other in an azimuthal direction ϕ, the gap between mirrors is given by

$$d(x, y) = d_0 + \theta(x\cos\phi + y\sin\phi). \tag{3.24}$$

x, y are coordinates in the mirror plane, with the beam center at $(0, 0)$. The round-trip phase varies across the beam footprint as

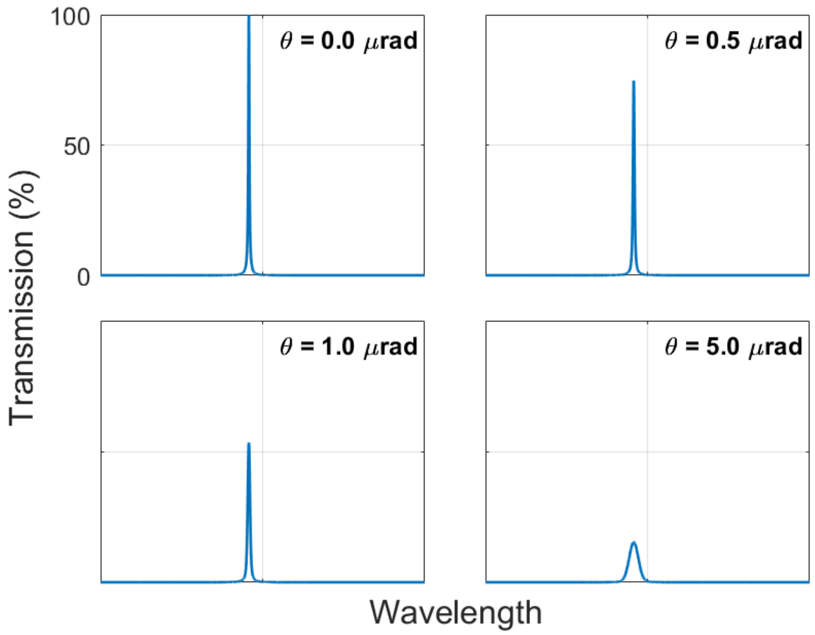

Figure 3.10: Numerical simulation of the effect of mirror non-parallelism on cavity transmission. Cavity is 5 cm in length, mirror reflectivity is 99%, and laser spot size is 10 mm. θ is the mirror wedge angle.

$$\delta(x, y; \lambda) = \frac{4\pi n d(x, y)}{\lambda}\,. \tag{3.25}$$

The resonance condition is $\delta = 2m\pi$, so different parts of the beam see different resonances, leading to inhomogeneous broadening. The Airy transmission is

$$T(\lambda) = \frac{1}{1 + F\sin^2\left(\frac{\delta}{2}\right)}\,, \tag{3.26}$$

where

$$F = \frac{4R}{(1-R)^2}\,. \tag{3.27}$$

The effective ITF can be modeled as the Gaussian-weighted average of the local transmissions:

$$T_{\text{avg}}(\lambda) = \frac{\iint_{\text{aperture}} I(x, y) T(\lambda; x, y) dx dy}{\iint_{\text{aperture}} I(x, y) dx dy}\,, \tag{3.28}$$

where the beam $I(x,y)$ is given by

$$I(x,y) = \exp\left[-\frac{2\left(x^2+y^2\right)}{w^2}\right] . \tag{3.29}$$

We use a discrete $N_{xy} \times N_{xy}$ grid with normalized weights $W(x,y)$ given by

$$W_{ij} = \frac{I_{ij}}{\sum_{m,n} I_{mn}} , \tag{3.30}$$

where $I(x,y) = 0$ for points outside the etalon mirrors.

3.2.7 Advantages of CW lasers

For CW laser excitation, each atom with longitudinal velocity v that enters the light beam effectively sees a laser pulse of length equal to the transit time $\tau_\mathrm{t} = d/v$, where d is the width of the laser beam. Here, for simplicity, we are neglecting the dependence on transverse velocity and on the shape of the laser beam profile.

Consider an atomic beam with density n_0 subject to two overlapping laser fields with intensities I_{12} and I_{2i}, respectively, driving transitions from the ground state 1 to an excited state 2 and then ionizing via an autoionizing state i. The level population densities n_1 and n_2 of atoms subject to laser light can be described by the rate equations

$$\begin{aligned}\frac{dn_1}{dt} &= -B_{12}n_1 + \left(A_{21}+B_{21}\right)n_2 \\ \frac{dn_2}{dt} &= B_{12}n_1 - \left(A_{21}+B_{21}+B_{2i}\right)n_2 \,,\end{aligned} \tag{3.31}$$

where A_{21} is the rate of spontaneous decay from state 2 to 1, $B_{mm'}$ are the stimulated transition rates from $m \to m'$, and γ is the atomic transit rate through the laser beam. In general, the populations n_m and transition rates $B_{mm'}$ are each functions of longitudinal atomic velocity v. However, if autoionizing transition is broad, B_{2i} can be considered effectively velocity independent [326]. If the pump transition is narrower than the transverse Doppler distribution, the pump laser can be spectrally broadened, or high enough intensity used to address the entire Doppler distribution. Thus, Eq. 3.31 can be taken to describe the entire transverse velocity distribution, with all quantities considered velocity independent.

Now, consider a group of atoms with longitudinal velocity v that all enter the beam at the same time. If we assume saturation conditions for the $1 \to 2$ transition, i.e., $B_{12} = B_{21} \gg A_{21}, B_{2i}$, then over short time scales we have a quasi-steady-state condition in which we can set $dn_1/dt = dn_2/dt = 0$ and neglect A_{21} and B_{2i}, so that Eq. 3.31 reduces to $n_2 = n_1$. In other words, light field 1 continuously equilibrates the level populations so that at any given time, half of the atoms are in state 1 and half are in state 2. Over longer time scales (but still shorter than the transit time), the total number of atoms decreases as atoms are ionized. Adding the two equations (3.31), we find an expression for the rate of increase of ion density n_i, equal to the decrease of the atomic population $n = n_1 + n_2$

$$\frac{dn_i}{dt} = -\frac{dn}{dt} = B_{2i} n_2 = B_{2i} n/2 \,, \tag{3.32}$$

or, since $n + n_i = n_0$,

$$\frac{dn_i}{dt} = B_{2i} \left(n_0 - n_i \right) /2 \,. \tag{3.33}$$

Integrating Eq. 3.33 over the transit time, we can find the ionization fraction n_i/n_0 for these atoms. For numerical evaluation and plotting it is more convenient to work with the quantity $\eta = 1 - n_i/n_0$, i.e., the fraction of atoms that are not ionized. We find

$$\eta_{cw} = \exp\left(- \int_0^{\tau_t} B_{2i} dt/2 \right) \,. \tag{3.34}$$

The ionization transition rate is given in terms of the photoionization cross section σ_{2i} by $B_{2i} = \sigma_{2i}\Phi_{2i}$, where $\Phi_{2i} = I_{2i}/(\hbar\omega_{2i})$ is the flux of ionizing photons. Thus the integral in Eq. 3.34 is given by

$$\int_0^{\tau_t} \frac{1}{2} B_{2i} dt = \frac{\sigma_{2i} I_{2i} \tau_t}{2\hbar\omega_{2i}} = \frac{\sigma_{2i} P_{2i}}{2\hbar\omega_{2i} v d} \,, \tag{3.35}$$

where we have used the definition of τ_t and written the light intensity in terms of the light power $P_{2i} = I_{2i}d^2$. Defining the saturation parameter

$$\kappa_{cw} = \frac{\sigma_{2i} P_{2i}}{2\hbar\omega_{2i} v_0 d}\,, \tag{3.36}$$

where v_0 is the most probable atomic speed in the oven from the Maxwell-Boltzmann distribution, we have for the un-ionized fraction of atoms with velocity v:

$$\eta_{cw}(v) = \exp\left(-\kappa_{cw} v_0 / v\right)\,. \tag{3.37}$$

Now, the longitudinal velocity distribution $f(v)$ in a thermal atomic beam produced by an oven at temperature T is given by [327]:

$$f(v)dv = 2\frac{v^3}{v_0^4} e^{-v^2/v_0^2} dv\,. \tag{3.38}$$

It is convenient to write the velocity distribution in terms of a dimensionless velocity $\xi = v/v_0$

$$f(\xi)d\xi = 2\xi^3 e^{-\xi^2} d\xi\,. \tag{3.39}$$

To find the total un-ionized fraction, we multiply Eq. 3.37 by the velocity distribution $f(\xi)$, and integrate over velocity. This gives

$$\eta_{cw} = \int_0^\infty f(\xi)\eta_{cw}(\xi) d\xi = \int_0^\infty 2\xi^3 e^{-\xi^2} e^{-\kappa_{cw}/\xi} d\xi = \frac{\kappa_{cw}^4}{16\sqrt{\pi}} G_{0,3}^{3,0}\left(-2, -\frac{3}{2}, 0 \,\middle|\, \frac{\kappa_{cw}^2}{4}\right) \tag{3.40}$$

where G is the Meijer G-function. We are interested in the regime $\kappa_{cw} > 1$. Expanding this function in a power series, we find within 1% accuracy in this range,

$$\eta_{cw} \approx e^{-3(\kappa_{cw}/2)^{2/3}} \left(0.383\kappa_{cw}^{-1/3} + 1.579\kappa_{cw}^{1/3} + 1.023\kappa_{cw}\right)\,. \tag{3.41}$$

3.2.8 Comparison with pulsed lasers

Now consider the case of pulsed excitation, with laser pulses of length τ_p at a repetition rate f_{rep}. We assume that the pulse length is much shorter than the characteristic atomic transit time, i.e., $\tau_p \ll d/v_0$, but still much longer than the equilibration time for optical pumping on the $1 \to 2$ transition. Then the development proceeds as for the CW case, except that each atom sees an integer number of pulses, the number depending on its velocity and the time that it enters the interaction region. The number of light pulses that a given atom may be subject to is determined by the ratio of its transit time τ_t through the light beam to the pulse repetition period $1/f_{rep}$, i.e., the quantity $\beta = \tau_t f_{rep} = f_{rep} d/v$. Writing $\beta = m + r$, where m is the integer part of β and r is the remainder, a given atom with transit parameter β will be subject to either m or $m+1$ pulses, depending on the time that the atom enters the interaction region; i.e., for $0 < \beta < 1$, an atom will see either 0 or 1 pulses, for $1 < \beta < 2$, either 1 or 2 pulses, etc. The fraction of atoms that see the higher number of pulses is r. Thus, the un-ionized fraction for atoms with velocity v is

$$\eta_p(v) = (1-r)e^{-m\kappa_p} + re^{-(m+1)\kappa_p} \,, \tag{3.42}$$

where m and r both depend on v, and we have obtained the saturation parameter κ_p for the pulsed case,

$$\kappa_p = \frac{\sigma_{2i} P_{2i} \tau_p}{2\hbar\omega_{2i} d^2} = \frac{\sigma_{2i} \bar{P}_{2i}}{2\hbar\omega_{2i} f_{rep} d^2} \,, \tag{3.43}$$

from κ_{cw} by replacing the characteristic transit time with the laser pulse time and writing the peak laser power P_{2i} in terms of the average light power

$$\bar{P}_{2i} = P_{2i} \tau_p f_{\text{rep}} \ . \tag{3.44}$$

Multiplying by the atomic velocity distribution and changing variables from v to β gives the integral for the total un-ionized fraction

$$\eta_p = \int_0^\infty 2\frac{\beta_0^4}{\beta^5} e^{-\beta_0^2/\beta^2} \left[(1-r)e^{-m\kappa_p} + re^{-(m+1)\kappa_p}\right] d\beta \,, \tag{3.45}$$

where $\beta_0 = f_{rep} d/v_0$ is the characteristic transit-time parameter for the velocity distribution. Using the substitution $\beta = m + r$, we can break up this integral into a sum of integrals over r for each value of m, each integral running from $r = 0$ to 1

$$\eta_p = \sum_{m=0}^{\infty} \int_0^1 \frac{\beta_0^4}{(m+r)^5} e^{-\beta_0^2/(m+r)^2} \left[(1-r)e^{-m\kappa_p} + re^{-(m+1)\kappa_p}\right] dr \,. \tag{3.46}$$

Evaluating the integrals, we find that the series can be written as

$$\begin{aligned}
\eta_p = \quad & e^{-{\beta_0}^2} - \frac{1}{2}\sqrt{\pi}\beta_0 \left(1 - \operatorname{erf}\beta_0\right) \\
&+ e^{-\kappa_p}\left[\frac{\sqrt{\pi}}{2}\beta_0\left(1 - 2\operatorname{erf}\beta_0 + \operatorname{erf}\left(\frac{\beta_0}{2}\right)\right) + 2e^{-\frac{{\beta_0}^2}{4}} - 2e^{-{\beta_0}^2}\right] \\
&+ \sum_{m=2}^{\infty} e^{-m\kappa_p}\left[\frac{\sqrt{\pi}}{2}\beta_0\left(\operatorname{erf}\left(\frac{\beta_0}{m-1}\right) - 2\operatorname{erf}\left(\frac{\beta_0}{m}\right) + \operatorname{erf}\left(\frac{\beta_0}{m+1}\right)\right)\right. \\
&\left. +(m-1)e^{-\frac{{\beta_0}^2}{(m-1)^2}} - 2me^{-\frac{{\beta_0}^2}{m^2}} + (m+1)e^{-\frac{{\beta_0}^2}{(m+1)^2}}\right] \,,
\end{aligned} \tag{3.47}$$

where "erf" is the error function. The terms on the first and second lines describe atoms that are subject to 0 and 1 laser pulses, respectively, while each term of the sum from $m = 2$ to ∞ describes atoms that are subject to m laser pulses. For accurate numerical evaluation, the series can be truncated after a small number of terms. For large enough κ_p, all terms except those on the first line are negligible; in this regime η_p is independent of κ_p.

3.2.9 Applications

In this section we discuss an application of MRLIS to strontium, which has a rare isotope, ^{84}Sr, that can be used as a tracer for bone absorption to detect the onset of osteoporosis [328]. This same isotope can also be used to produce the radioisotope ^{85}Sr, which we have proposed for a new test of quantum mechanics [329, 330]. A rate-equation model is presented and used to make estimates of ionization fraction in the pulsed and CW cases as a function of ionizing laser power, beam diameter, repetition rate (in the pulsed case) and oven temperature. Saturated optical pumping on the transition to the intermediate state is assumed. The magnitude of expected AC Stark shifts of the transition is also discussed. We estimate that the combination of high intracavity power and long transit time leads to near unity in ionization probability, and we expect MRLIS to significantly facilitate new and existing applications of isotopes in medicine. Perhaps the most exciting future application of MRLIS is towards production of radioisotopes as an alternative to radiochemistry, due to the small footprint of the system's vacuum chamber, which fits into standard hot cells. One particularly compelling case is production of the radioisotope ^{177}Lu from stable ^{176}Lu due to the much larger ($\sim 700\times$) neutron cross section of ^{176}Lu compared with ^{176}Yb [331]. The latter stable isotope is currently used to produce ^{177}Lu, which is then separated using radiochemistry methods [317].

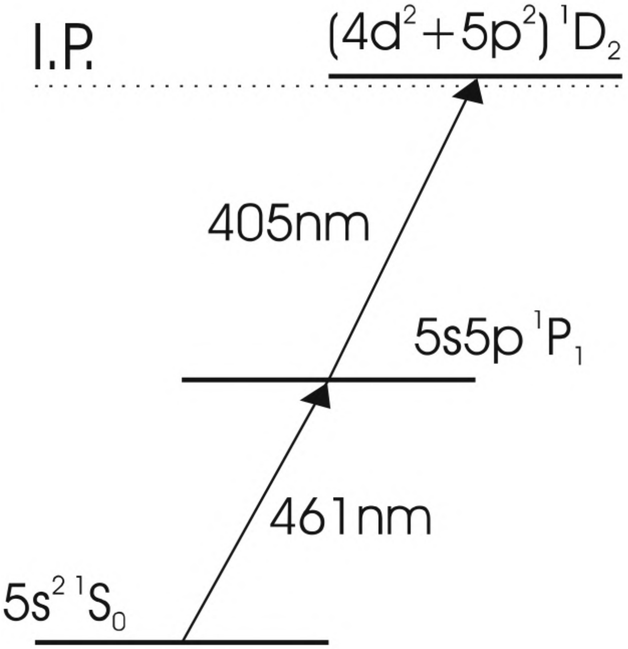

Figure 3.11: Optical pumping scheme for photoionization via intermediate state $5s5p\,^1P_1$ and autoionizing state $5p^2\,^1D_2$. The dotted line represents the strontium ionization potential. Image credit: [332].

Experimental parameters for the numerical results are given in Table 3.1, and a schematic of the relevant energy levels in atomic strontium is shown in Fig. 3.11. The ionization limit of Sr is 5.695 eV. The ground $^1S_0$ state would first be excited by a laser near 461 nm to the $^1P_1$ state which has a decay rate of 2.01×10^8 s^{-1}. A second laser near 405 nm would then excite atoms from the $^1P_1$ state to the $^1D_2$ autoionizing state [333]. The ionization cross section in Table 3.1 is the isotropic cross section σ_{iso}, appropriate for excitation with unpolarized light [334]. For linearly polarized light the cross section depends on the angle θ between the pump and ionizing laser polarization axes. Assuming that ionization is due to a $J = 1 \rightarrow J = 2$ transition, the dependence is given by:

$$\sigma_{2i} = \frac{3}{10}\left(3 + \cos^2\theta\right)\sigma_{iso}\,, \tag{3.48}$$

or $\sigma_{2\text{i}} = 1.2\sigma_{\text{iso}}$ for parallel polarizations [335]. The laser will be scanned just above the ionization limit to optimize ionization with an autoionizing state, but it may be simpler to find a convenient high-power laser that is above the ionization threshold. Positive ions will be accelerated by an electric field that will remove the desired isotopes from the beam and collect them on a cathode plate.

Ionization cross section	σ_{2i}	$1.2 \times 5450\,\text{Mb}$
Ionization photon energy	$\hbar\omega_{2i}$	$4.9 \times 10^{-19}\,\text{J}$
Atomic mass	m_a	88 amu
Pulse repetition rate	f_{rep}	1 to 10 kHz
Oven temperature	T	690 to 930 K
Most probable atomic speed in oven	v_0	360 to 420 m/s
Mean longitudinal atomic beam velocity	$\bar{v}$	480 to 560 m/s
Laser beam diameter	d	1 to 5 cm
Circulating ionizing laser power (CW)	P_{2i}	$\leq 5\,\text{W} \times 100$ (build-up)
Average ionizing laser power (pulsed)	$\bar{P}_{2i}$	$\leq 25\,\text{W}$

Table 3.1: Parameters used for the numerical estimates.

Here we employ the rate-equation model discussed in prior sections, valid for CW excitation or when laser pulses are much longer than the excited state lifetime [303, 336, 337, 338, 339]. We assume that the atomic density is low enough that the medium can be considered optically thin. For a uniform atomic beam of density n, interaction cross-section $\sigma(\nu)$, and laser interaction path length L, the atomic beam can be considered optically thin if

$$n \ll \frac{1}{L\sigma(\nu)} \tag{3.49}$$

[340]. For the 405 nm transition of strontium, values from Table 3.1 suggest that atomic beam densities $n \ll 10^{13}$ cm^{-3} are optically thin. Typical densities for collimated atomic beams from thermal oven sources are in the range $10^7 - 10^{10}$ cm^{-3}, satisfying the criterion for optical thinness.

Our proposed method for efficient isotope separation based on laser ionization can be usefully compared with the prior method of laser ionization by simple scaling. In that case, pulsed lasers were utilized, with a typical pulse duration of 100 ns and a pulse repetition rate of 10 kHz [341]. The average laser power was in the range of 20 W as typical with pulsed dye lasers. The enhancement of the ionizing laser in MRLIS with a 1000 finesse cavity, and use of continuous-wave solid state lasers with a power of 5-10 W, would provide a comparable average laser intensity to that of the pulsed laser, assuming similar focusing. The interaction time would be about 1000 times longer in the case of MRLIS, addressing all the desired isotopes in the atomic beam, and bringing the ionization probability to near unity. In addition, the use of narrow-band continuous-wave lasers would enable high isotopic purity, unlike the previous method where the excitation lasers had large linewidths on the order of 100 MHz, limiting isotopic purity. Pulsed lasers operating in the neighborhood of 405 nm capable of matching the ionization efficiency of a cavity-enhanced CW system do not appear to be widely available. For example, a 15 mW pulsed laser with a 10 MHz repetition rate, available from Thorlabs [342], provides an ionization efficiency of 0.04%. Quantel and Ekspla offer OPO-based systems at this wavelength with average power approaching 1 W, but repetition rates in the 10-100 Hz range and consequently very low ionization rates, below 1% [343, 344].

Substituting numerical parameters from Table 3.1 into the expression for κ_{cw} from Section 3.2.7, we find:

$$\kappa_{cw} \approx 4.85 \frac{P_{2i}[\mathrm{W}]}{d[\mathrm{cm}]\sqrt{T[\mathrm{K}]}}\,, \tag{3.50}$$

with an upper range of $\kappa_{cw} \leq 90$. The un-ionized fraction η_{cw} is plotted for a range of

κ_{cw} in Fig. 3.12(a). For a cavity with an enhancement factor of 200, an input power of at least 1.1 W would achieve ionization efficiency $> 99\%$.

Substituting numerical parameters into the expressions for κ_p and β_0 from Section 3.2.8, we find:

$$\kappa_p \approx 6.67 \frac{\bar{P}_{2i}[\text{ W}]}{d^2 [\text{ cm}^2]\, f_{rep}[\text{kHz}]}\,, \tag{3.51}$$

and

$$\beta_0 \approx 0.727 \frac{d[\text{cm}] f_{\text{rep}}\,[\text{kHz}]}{\sqrt{T}[\text{K}]}\,, \tag{3.52}$$

with typical values $\kappa_p \leq 45$ and $\beta_0 \leq 2$. The un-ionized fraction η_p is plotted for a range of κ_p and β_0 in Fig. 3.12(b).

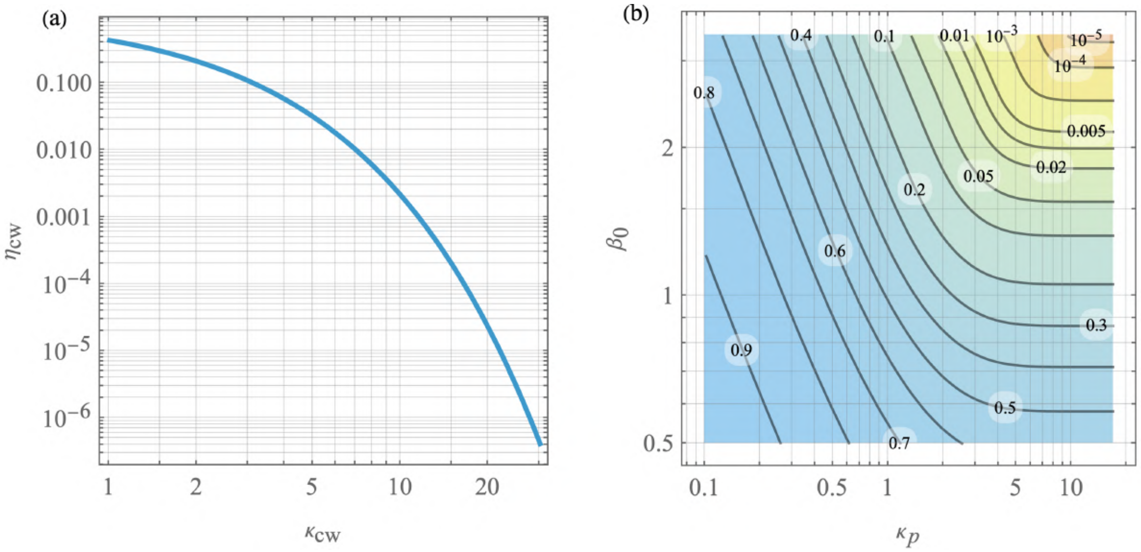

Figure 3.12: (a) CW un-ionized fraction η_{cw} and (b) pulsed un-ionized fraction η_p as a function of dimensionless parameters κ_{cw}, κ_p and β_0. The "useful" range of the saturation parameters κ_{cw} and κ_p are plotted, above which further improvement in ionization fraction is negligible.

The AC Stark shift of a state due to light interacting with a given transition is of the order of Ω^2/Δ, where Δ is the light detuning from resonance, $\Omega = dE/\hbar$ is the Rabi frequency, d is the dipole matrix element and E is the light electric field amplitude. Writing d in terms of the natural width Γ and wavelength λ of the transition and E in terms of the light intensity I and neglecting numerical factors of order unity [345], we have

$$\Omega = \frac{1}{\pi}\sqrt{\frac{\Gamma I \lambda^3}{\hbar c}}\,, \tag{3.53}$$

resulting in a Stark shift

$$\frac{\Gamma I \lambda^3}{\pi^2 \Delta \hbar c}\,. \tag{3.54}$$

A significant contribution to the AC Stark shifts of the ground and excited state of the 461 nm transition due to the 405 nm light is likely to come from the 405 nm light interacting with the 461 nm transition itself. Using $\lambda = 460.9$ nm, $I = (100\ \mathrm{W})/(3\ \mathrm{cm})^2$, $\Gamma = 1/(5.2\ \mathrm{ns})$, and $\Delta = 2\pi c/(405.2\ \mathrm{nm}) - 2\pi c/(460.9\ \mathrm{nm}) = 5.6 \times 10^{14}/\mathrm{s}$, we can estimate a Stark shift on the order of 10 kHz. Thus we can conclude that for this case the AC Stark shifts are negligible.

Chapter 4: Atomic Thermalization by Weak Adsorption on Polymer Films

While experimenting with techniques to improve the detection efficiency of our iron isotope spectroscopy, we[1] encountered an unexpected and potentially useful property of micron-thickness silane polymer coatings, in particular polydimethylsiloxane (PDMS). When hot atoms strike such surfaces, they are diffusely scattered, and the scattered atoms are observed to fully thermalize with the polymer surface. However, thin PDMS films proved exceedingly resistant to accumulating any significant quantity of the impinging atoms used in our experiments, even when placed directly in the beamline produced by an atomic oven for hours. Physically, this suggests an interesting balance: because the scattered atoms assume the surface's temperature, they are presumably adsorbed long enough to thermally equilibrate with the polymer coating, yet they are bound to the surface so weakly that essentially all atoms are eventually desorbed.

Long-chain polymers like paraffin and PDMS have long been used as anti-spin relaxation coatings on the interior surfaces of vapor cells[2]][347, 348, 349]; however, because of the very application-specific nature of these coatings, at least as far as atomic physics is concerned, their literature almost exclusively concerns interactions with alkali metals [350, 351, 352]. In fact, much of the literature investigating the remarkable "nonstick" behavior of PDMS for atomic physics applications relates desorption mechanisms to properties of alkali metals, particularly rubidium [347, 348, 353, 354]. Our observations strongly suggest that these favorable properties of PDMS, and possibly other silane coatings, are applicable to a far broader range of atomic species than were previously suspected, including transition metals and rare earth metals.

---

[1] This chapter is adapted from published work by V.J. Ajith, Aaron Barr, and Mark Raizen.

[2] These coatings help minimize the loss of atomic spin polarization during atomic collisions with the chamber walls.

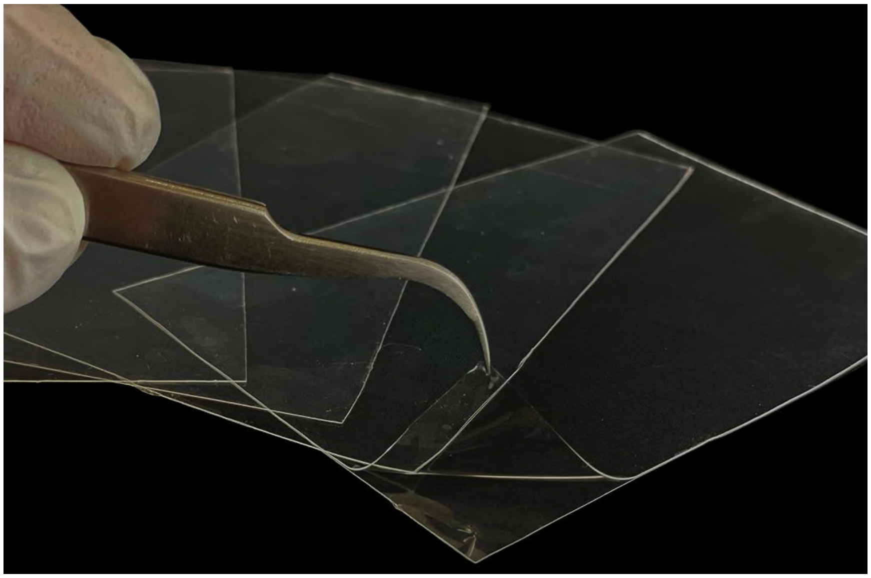

Figure 4.1: 100 μm-thickness PDMS film [346]

Thin PDMS coatings have potential application as a novel method of atom cooling via surface scattering, without loss of flux. This could be useful for enhancing the laser fluorescence detection of trace elements, because cooler atoms have increased transit times across the excitation laser. The longer the transit time, the more excitation-emission cycles occur, improving the fluorescence signal. For example, atoms from an iron effusion oven operating at 1970 K have a most probable velocity v_{mp} of 758 m/s, while the same iron atoms at 298 K have v_{mp} of 298 m/s, potentially doubling transit time and fluorescence photons emitted [355]. Atom trapping, used in optical clocks, quantum computing, and quantum sensing, is another possible area of application [350, 356, 357, 358].

While this finding is very promising, there are significant caveats. Chief among these is that the achievable temperature reduction by surface scattering is highly dependent on material properties. PDMS becomes brittle and loses its surface scattering properties at temperatures below around 200 K; producing a true cold atom source with this method would require a polymer with glass transition temperature lower than currently known.

4.1 Producing thin polymer films

Polydimethylsiloxane (PDMS) is a silicon-based organic polymer, consisting of a linear chain of repeating $-\mathrm{Si}\left(\mathrm{CH}_3\right)_2-\mathrm{O}-$ units: $\left(\mathrm{C}_2\mathrm{H}_6\mathrm{OSi}\right)_n$. The molecule has a backbone of alternating $\mathrm{Si}-\mathrm{O}-\mathrm{Si}$ linkages with a 143° bond angle, giving it a flexible open chain structure. The methyl side groups can rotate freely, and consequently PDMS has a very low glass transition temperature of -120°C,and low surface energy of 20-24 mN m^{-1}. The result is a polymer with unusual chain flexibility, chemical inertness, and very low intermolecular forces [359].

The scattering surfaces for our experiments were produced by spin-coating and subsequently curing a thin layer of Dow Sylgard 184 onto substrates made from microscope slides, or INFICON thickness monitor crystals. Sylgard is a trade name for a self-curing PDMS formulation produced by Dow Chemical Company [360]. Undiluted PDMS has viscosity of 3900 cP, making spin-coating of thin uniform films difficult [361, 362]. Diluting PDMS in a volatile solvent reduces its viscosity, allowing uniform spreading and controlled thinning by centrifugal forces and solvent evaporation; this enables the reliable production of thin films with thicknesses from micrometers to tens of nanometers by carefully adjusting the ratio of solvent to PDMS. The solvent must be volatile enough to evaporate cleanly during spinning, able to dissolve PDMS sufficiently, and compatible with the substrate. The solvent evaporation rate is critical; if it evaporates too quickly, as can occur with hexane, then the spun PDMS surface may develop striations or "orange-peel" texture. If the solvent evaporation rate is too slow, then the film will continue to flow after spinning. Toluene's in-between volatility yielded good uniformity in our experiments.

For this study, liquid PDMS was diluted with toluene in a $10:1$ solvent/polymer ratio. This solution was transferred to the substrate via micropipette and spun at 3000 rpm for 60 seconds. The solvent rapidly evaporates during the spinning process, leaving a visually uniform spot. Curing the film was accomplished by placing the coated substrate into a dish on a laboratory hotplate, and warmed at 65 °C for ~ 2

hours. Earlier studies using a similar protocol with the polymer PMMA measured the resulting film thickness at roughly 1 μm [363]. Quartz crystal monitor estimates of the thickness of the PDMS films we produced were consistent with this value. The surface morphology of thin PDMS films has been well characterized in prior studies, and are consistent with our observations of the films produced (see Fig. 4.2 [364]).

Figure 4.2: PDMS surface viewed under optical microscopy (~ 1 mm $\times\, 1$ mm). The coating contains sparse micron-sized impurities or imperfections, separated by more than $0.5 - 1$ mm. [365]

4.1.1 Theory

The physical theory of how a layer of viscous liquid on a spinning disk thins and spreads radially under centrifugal forces was described in a landmark 1958 paper by Alfred Emslie, Francis Bonner, and Leslie Peck [366]. It models the radial outflow of an incompressible Newtonian fluid with constant density ρ, viscosity η, and thickness $h(r,t)$ on a disk rotating with constant angular velocity ω. The fluid is assumed to be incompressible and axisymmetric, with film thickness $h \ll$ disk radius, so vertical velocities are small. Evaporation is considered negligible, so there is no mass loss of fluid. Secondary forces such as gravity and surface tension are not included in the model. In cylindrical coordinates (r, z), the Navier-Stokes equations reduce to:

$$0 = -\frac{\partial p}{\partial r} + \eta \frac{\partial^2 u}{\partial z^2} + \rho \omega^2 r \tag{4.1}$$

where $u(r, z, t)$ is the radial velocity in the liquid. The boundary conditions are given by:

$$\begin{aligned} &u(r, z = 0, t) = 0 \quad \text{(no slip at disk surface)} \\ &\frac{\partial u}{\partial z}(r, z = h, t) = 0 \text{ (no shear at free surface)} \end{aligned} \tag{4.2}$$

Integrating twice with respect to z, one obtains the radial velocity profile:

$$u(r, z, t) = \frac{\rho \omega^2 r}{2\eta} \left(z^2 - 2hz\right) \tag{4.3}$$

The continuity equation for an incompressible fluid in axisymmetric coordinates is:

$$\frac{\partial h}{\partial t} + \frac{1}{r} \frac{\partial}{\partial r}(r \bar{u} h) = 0 \tag{4.4}$$

where $\bar{u}$ is the height-averaged radial velocity, obtained by integrating u across z :

$$\bar{u}(r, t) = \frac{1}{h} \int_0^h u dz = -\frac{\rho \omega^2 r h^2}{3\eta} \tag{4.5}$$

Substituting into the continuity equation gives the Emslie-Bonner-Peck (EBP) film-thickness equation:

$$\frac{\partial h}{\partial t} = -\frac{\omega^2}{3v} \left(h^3 + r \frac{\partial h^3}{\partial r}\right) \tag{4.6}$$

where $v = \eta/\rho$ is the kinematic viscosity. For many practical cases, the radial derivative term is small compared to the first term, so the thickness can be approximated as spatially uniform:

$$\frac{\partial h}{\partial t} = -\frac{\omega^2 h^3}{3v} \tag{4.7}$$

which integrates to:

$$h(t) = \frac{h_0}{\sqrt{1 + \frac{2\omega^2 h_0^2 t}{3v}}} \tag{4.8}$$

Here h_0 is the initial film thickness at $t = 0$. The final steady-state thickness depends on the film's viscosity η, density ρ, and spin speed ω. Since h decreases as its own cube, most thinning occurs early. The film eventually becomes so thin that viscous drag nearly halts further thinning.

However, the EBP model does not capture the full dynamics that occurs with solvent/polymer systems. During the early spin-up stage, the EBP model is approximately valid, as the toluene-diluted PDMS is a nearly Newtonian fluid, and its thinning roughly follows the EBP model. However, as the solvent evaporates and viscosity rises, the process transitions into an evaporation-controlled regime, which is not modeled by EBP. In 1978, Dietrich Meyerhofer extended the EBP framework to films produced from solution, describing how film thickness $h(t)$ and solute volume fraction $C(t)$ evolve, and how the final dry thickness depends on spin speed, solute concentration, and solvent evaporation rate. A solution of initial concentration C_0 and initial thickness h_0 is deposited on a rotating substrate with angular speed ω. Two coupled processes occur simultaneously in Meyerhofer's model: the first process is radial outflow and thinning governed by viscous flow, as in EBP; the second process is mass loss via solvent evaporation, which causes the total volume to decrease and the solute fraction to increase. Thus, the total rate of thickness change is the sum of hydrodynamic thinning and evaporation loss. Meyerhofer proposed the phenomenological equation:

$$\frac{dh}{dt} = -\left(\frac{\omega^2 h^3}{3\upsilon} + E\right) \tag{4.9}$$

where E is an effective evaporation rate. The first term is the EBP viscous thinning, and the second term accounts for solvent volume loss by evaporation. The solution's viscosity rises rapidly with solute fraction. Meyerhofer adopted an empirical exponential relation to model this:

$$\eta(C) = \eta_s e^{\beta C} \tag{4.10}$$

where η_s is the solvent viscosity and β is an empirical parameter. Initially, C and viscosity can both be considered low, and evaporation a small effect. The EBP term dominates:

$$\frac{dh}{dt} \approx -\frac{\omega^2 h^3}{3\nu} \quad \Rightarrow \quad h(t) \propto t^{-1/2} \tag{4.11}$$

At later times, viscosity grows large enough that the flow term becomes negligible, and a "crossover" point is reached where the film thickness decreases linearly with time due to evaporation:

$$\frac{dh}{dt} \approx -E \quad \Rightarrow \quad h(t) \approx h_{\text{cross}} - E\left(t - t_{\text{cross}}\right) \tag{4.12}$$

The following empirical relation for final film thickness can be derived from the above:

$$h_f \propto C_0^{\alpha} \omega^{-\beta} \tag{4.13}$$

with parameters $\alpha \approx 1$ and $\beta \approx 0.6 - 1.0$ depending on solvent volatility, polymer viscosity, and temperature. The theoretical prediction for ideal Newtonian liquids with constant evaporation rate is $\beta = 2/3$. For viscoelastic fluids like PDMS, $\beta \approx 0.8 - 1$.

4.1.2 Apparatus

Figure 4.3: Instras spin-coater of the type used in this experiment [367]

The spin coater we used is a model SCK-300S from Instras Scientific, an Arduino-based spin-coater, rated for speeds from 500 to 5,000 RPM. The range of speeds was very helpful in finding solvent/spin parameters that yielded consistent thin films [367]. We usually worked with substrates significantly smaller than a glass slide, and found that mounting them on a slide with double-sided SEM carbon tape from Ted Pella, and then anchoring the whole assembly with the vacuum chuck [368]. Solvent/PDMS coating samples were produced using serial dilution and an adjustable micropipette.

4.1.3 Thickness estimation

Our 1 micron estimate of spun film thickness is consistent with the value predicted by empirical results from prior literature [363]. We directly measured the film thickness produced with our solvent and spin parameters by coating a quartz crystal

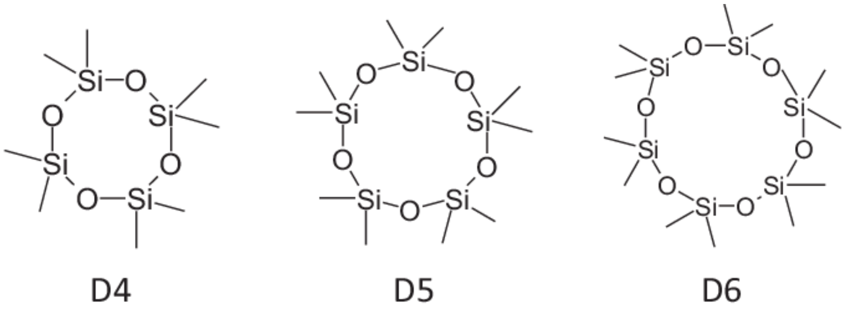

Figure 4.4: Molecular structure of D4, D5, and D6. [369]

microbalance (CQM) crystal with PDMS and measuring in-chamber at atmosphere. In vacuum, however, we found that the CQM registered a slow mass loss that interfered with direct CQM measurements of atom coating rate[3]. Initially, we believed this to be due to residual solvent, but extended gentle bakeout at 60°C – 80°C failed to measurably change the troublesome mass loss signal. More aggressive bakeout, at or above 100°C, was found to damage the crystals to the point of inoperability. With the benefit of experimental hindsight, it seems likely that the culprit was not residual solvent, but rather the outgassing of volatile siloxane rings, called D4, D5, and D6. PDMS itself has very low vapor pressure, in the mPa range at 25°C. Cyclic volatile methylsiloxanes (cVMS) are low molecular weight (MW) ring molecules present in most PDMS, and a known contaminant in UHV work [370]. These small species are quite volatile even at 25°C : 130 Pa for D4, 33 Pa for D5, and 4 Pa for D6 [371]. NASA data indicates measurable quantities of cVMS in Sylgard 184 [372, 373]. The room temperature mass loss we observed was almost certainly from this low-MW tail.

4.2 Polymer scattering of Fe / Yb

The surface scattering experiments were performed using two sources: an iron atomic beam produced by laser ablation, and an ytterbium beam produced by an

---

[3] See Section 4.2.2.

effusion oven. The relatively stable higher flux that can be achieved with an effusive oven was beneficial for some measurements, and the combination of high melting point and low vapor pressure of iron make it an interesting test case for novel atom cooling techniques [355].

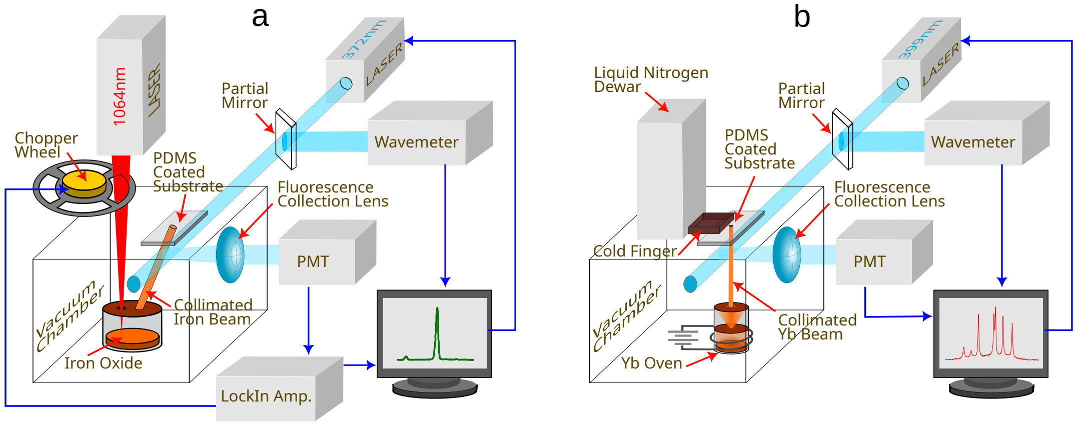

Figure 4.5: (a): Fe scattering setup. (b): Yb scattering setup.

For the iron scattering experiment, shown in Fig. 4.5(a), the IR ablation laser was focused on the powder surface through one of the two apertures in the top plate on the sample holder. The resulting collimated beam of atomic iron exited the opposite aperture at a 15° angle relative to the ablated powder surface. The 372 nm excitation laser was aligned adjacent to where the atom beam impacts the PDMS coating. Thus, both incoming collimated atoms and scattered atoms from the PDMS surface are excited by the 372 nm laser. Fig. 4.5(b) illustrates the experimental setup for the surface scattering of ytterbium atoms. The oven produces an atomic beam of ytterbium, which is collimated by a sequence of razor-edge slits. The atoms strike a surface downstream, which can be either fixed, or a QCM sensor attached to a long-travel screw and bellows arrangement, allowing the sensor to be maneuvered into the beamline or withdrawn from the chamber. A probe laser tuned to the 399 nm transition of ytterbium crosses the beamline at right angles, slightly upstream from the surface position. A PDMS-coated substrate was attached to a feedthrough on the vacuum chamber and positioned just above the observation volume, where the excitation laser and collimated atom beam intersect, as shown in Fig.4.5. Depending on the experiment, the substrate was mounted either on a liquid nitrogen cold finger or a quartz crystal thickness monitor.

The two-section ytterbium oven used in this experiment was inherited from a prior experiment by former group member Igal Bucay [374, 375]. The two sections consist of a reservoir for granules of ytterbium metal, and a nozzle which was originally intended to hold an array of capillary tubes. The oven is designed to operate continuously at temperatures up to 750°C. Because ConFlat (CF) flanges with copper gaskets have a maximum acceptable temperature of 450°C, the oven and its heater cables are enclosed inside the vacuum chamber and thermally isolated using Macor ceramic standoffs [376].

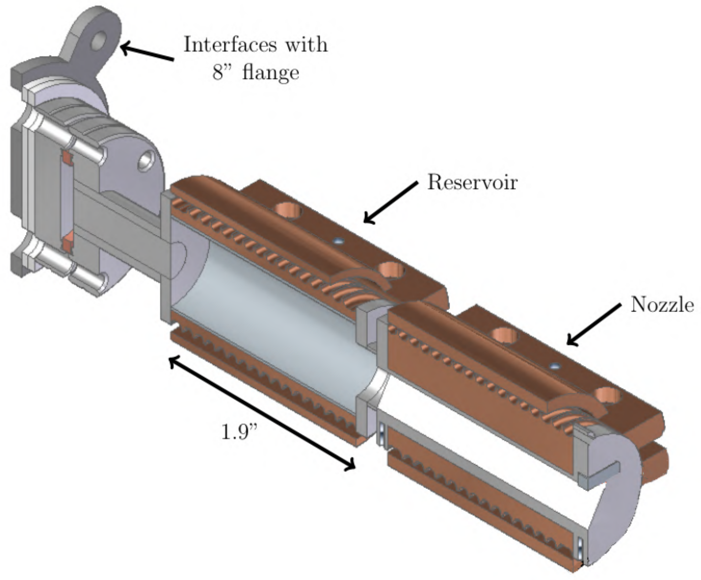

Figure 4.6: Cross-section view of ytterbium oven. Image adapted from [375].

The body of the oven consists of custom-machined 0.025″-thick stainless steel. Oxygen-free copper sleeves are press-fitted onto the stainless-steel body for a nearly

23-fold increase in thermal conductivity [377]. Sixteen round trenches with a radius of 0.045″ are threaded over about 1.8″ on the copper sleeves to support custom aero-rod heater cables from ARi Industries. These heater cables consist of heating wires enclosed in an Inconel sheath and insulated with magnesium oxide. The heater cables for the reservoir and nozzle are identical, with a length of about 5 ft and a diameter of 0.093″ so that they fit tightly in the 0.045″-radius grooves. Each heater cable is wrapped around the reservoir or nozzle and held tightly in place by copper clamps. One type-K thermocouple was attached to each heater cable powered by separate transformers to maintain an approximate 100 °C temperature difference between the reservoir and nozzle to prevent clogging [375].

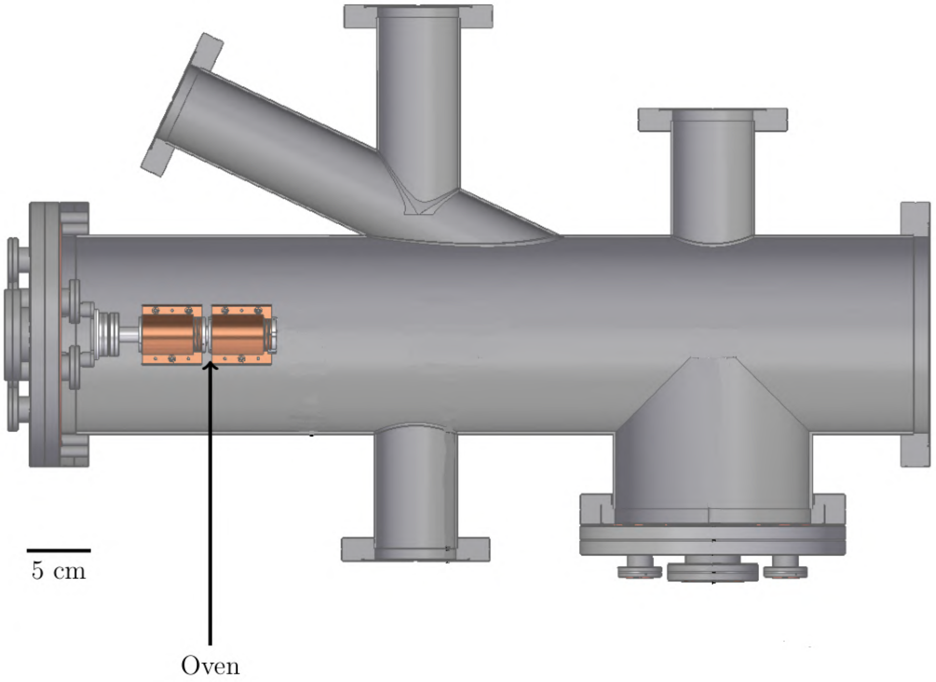

Figure 4.7: Ytterbium oven and chamber used in scattering experiment. Image adapted from [375].

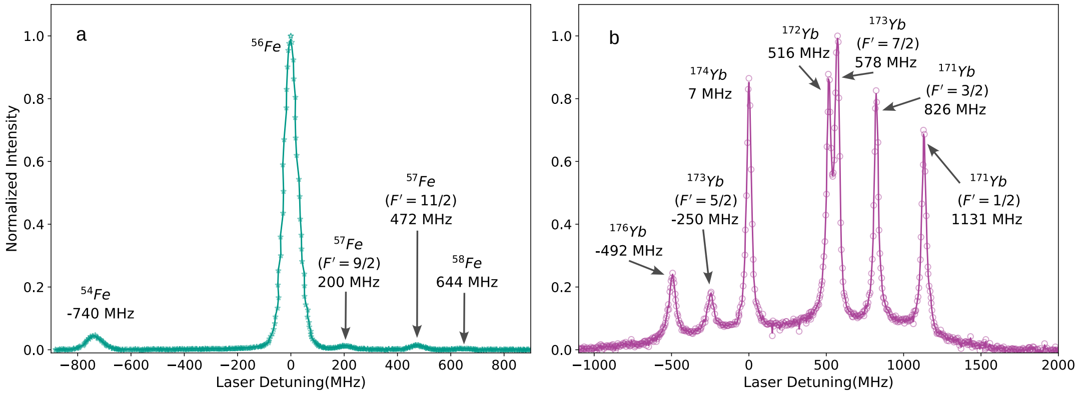

Figure 4.8: Fluorescence spectra for: (a) Fe, and (b) Yb [365].

4.2.1 Estimation of scattered atom temperature

The excitation beam was tuned across a range of roughly 2 GHz while measuring the intensity of fluorescence, producing spectra in which peaks corresponding to each of the stable iron isotopes, ^{54}Fe, ^{56}Fe, ^{57}Fe, and ^{58}Fe, appear. Fig. 4.8 (a) shows a spectrum from the iron atom beam for a collimation ratio of 0.021. We define the collimation ratio as the radius of the collimating aperture divided by the distance the aperture have from the ablation point. The LIF spectrum for an atomic iron beam scattered from a PDMS surface is shown in Fig.**??**, with data points represented by blue circles. The spectrum captures both the inbound collimated atomic beam and the diffusely scattered atoms from the surface; the sharp peaks in the spectrum are due to the collimated atoms and the broad background is due to the scattered atoms. Induced fluorescence from the glass substrate or PDMS coating can be discounted, as they would be filtered by the lock-in amplifier.

Ytterbium's optical transition near 399 nm $(6s^{2\,1}S_0 \rightarrow 6s6p^1P_1)$ was used to probe the atomic flux. The lifetime of the 399 nm transition is $\tau = 5.464$ ns, so the natural linewidth is $\Gamma/2\pi \approx 29.1$ MHz [378]. This transition is nearly closed; the $^1P_1$ state has a very small leak on the order of 10^{-7}, so repumping is unnecessary for LIF spectroscopy [378]. The saturation intensity is given by $I_{\text{sat}} = \pi h c \Gamma / (3\lambda^3) \approx 60$ mW/cm^2. Ytterbium has seven naturally-occurring isotopes, and

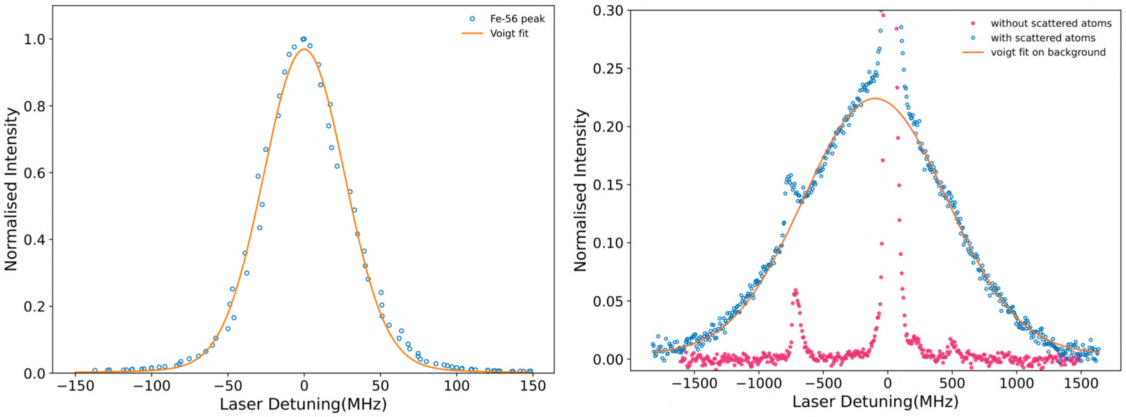

Figure 4.9: Left: Voigt fit to collimated atom beam. Right: Scattered fluorescence spectrum for Fe with Voigt fit to background [365].

thus a more complex isotopic spectrum than iron[4]. Yb^{171} and Yb^{173} have hyperfine structure [379]. Fig. 4.8(b) shows a plot of the Yb spectrum for this transition taken using our experimental setup.

The temperature of the collimated beam and scattered atoms are estimated by fitting Voigt functions to the spectra, shown in Fig.4.9. A Voigt profile is the convolution of a Gaussian (Doppler) component and a Lorentzian (natural linewidth) component:

$$V(\nu) = \int_{-\infty}^{\infty} G(\nu')\, L(\nu - \nu')\, d\nu' \tag{4.14}$$

where $G(\nu) = \frac{1}{\sigma\sqrt{2\pi}} \exp\left[-\left(\nu - \nu_0\right)^2 / \left(2\sigma^2\right)\right]$ describes Doppler broadening due to the velocity distribution of the atoms, and $L(\nu) = \frac{\gamma/\pi}{(\nu-\nu_0)^2+\gamma^2}$, describes homogeneous broadening (natural linewidth, collisional, power broadening, etc.). The Voigt width depends on both Gaussian width σ and Lorentzian half-width γ. For an atom of mass m emitting or absorbing at central frequency ν_0, the Doppler broadening due to thermal motion along the laser/observation axis is:

---

[4] $Yb^{174}(31.8\%), Yb^{172}(21.9\%), Yb^{173}(16.1\%), Yb^{171}(14.3\%), Yb^{176}(12.7\%), Yb^{170}(3.05\%), Yb^{168}(0.13\%)$.

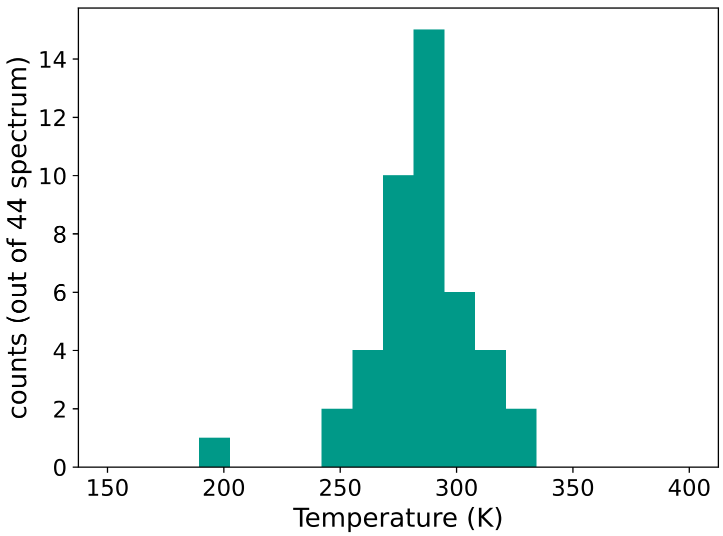

Figure 4.10: Histogram of the estimated temperatures from 44 independent spectra of scattered atoms from PDMS coated glass slides. [365].

$$\Delta\nu_D = \nu_0\sqrt{\frac{8k_BT\ln 2}{mc^2}} \tag{4.15}$$

Here $\Delta\nu_D$ is the full width at half-maximum (FWHM) of the Gaussian component. Thus, extracting $\Delta\nu_D$ from a numerical Voigt profile fit, the temperature can be determined from:

$$T = \frac{mc^2}{8k_B\ln(2)}\left(\frac{\Delta\nu_D}{\nu_0}\right)^2 \tag{4.16}$$

The temperature estimate from this fit indicates that the incoming atoms are at a temperature of around 1418 ± 130 K. Uncertainty in the temperature comes from the uncertainty in the collimation ratio. The fit is repeated over multiple data sets as the substrate is moved to expose different areas of the PDMS coating to interact with the atom beam. The temperature estimates of the scattered atoms thus obtained from these fits are shown as a histogram in Fig.4.10. We find that the mean temperature value of the scattered atoms is 285 K, and the standard deviation is 22 K. We expect the substrate to be equilibrated to the laboratory temperature, which is maintained at 293 K. Our measurement of the temperature of scattered atoms is close to the temperature of the surface from which the atoms scattered. This temperature, around 293 K, is lower than the original atom temperature of 1400 K by almost a factor of 5, and the most probable velocity of the atoms is halved.

4.2.2 Coated/uncoated QCM crystals

The quartz crystal microbalance (QCM) is a type of ultrasensitive mass sensor that can be used to measure minute changes in mass, thickness, or viscoelastic properties by monitoring shifts in the resonant frequency of a piezoelectric quartz crystal. Their operating principle is based on the inverse piezoelectric effect in quartz, SiO_2. Quartz is piezoelectric; when mechanically strained, it produces an electric potential. Conversely, when an electric field is applied, it deforms mechanically. At specific frequencies, the deformation is resonantly amplified, and the crystal vibrates in its fundamental thickness-shear mode, where layers of quartz slide parallel to the faces in opposite directions. The fundamental frequency, f_0, depends primarily on the crystal's thickness t_q and the shear-wave velocity v_q :

$$f_0 = \frac{v_q}{2t_q} \tag{4.17}$$

The shear-wave velocity is a fundamental material property determined by the elastic stiffness, mass density and crystallographic orientation of the crystal. For an isotropic solid, the shear-wave velocity is given by

$$v_s = \sqrt{\frac{G}{\rho}} \tag{4.18}$$

where G is the shear modulus, and ρ is the density. Quartz is anisotropic, so the value of G depends on the direction within the crystal lattice; its stiffness is described by a tensor C_{ij} with components:

$$\begin{aligned}
C_{11} &= 8.676 \times 10^{10} \text{ Pa} \\
C_{12} &= 6.948 \times 10^{9} \text{ Pa} \\
C_{13} &= 1.174 \times 10^{10} \text{ Pa} \\
C_{14} &= -1.794 \times 10^{10} \text{ Pa} \\
C_{33} &= 1.059 \times 10^{11} \text{ Pa} \\
C_{44} &= 5.793 \times 10^{10} \text{ Pa}
\end{aligned} \tag{4.19}$$

The direction of the applied field and the crystal's cut orientation relative to its crystallographic axes determine the type of vibration mode, the temperature coefficient of the resonant frequency, and the sensitivity to mechanical or thermal stresses. CQM crystals typically use what is called an "AT-cut," orientation, which has two major benefits: the frequency-temperature curve has a turning point near 25°C, minimizing drift with temperature, and the AT-cut supports pure thickness-shear vibrations, which couple efficiently to surface-bound mass but minimally to the surrounding air or liquid. AT-cut crystals have low internal losses, providing high stability and sensitivity [380]. The AT-cut is obtained by slicing the quartz crystal at an angle of about 35.25° relative to the optical Z-axis, which is the principal symmetry axis of the crystal. This rotation mixes components of C_{44}, C_{14}, and C_{66} (where $C_{66} = (C_{11} - C_{12})/2$). The resulting effective shear modulus for the thickness-shear mode is:

$$\mu_{\mathrm{AT}} = C'_{66} \approx 2.95 \times 10^{10} \text{ Pa} \tag{4.20}$$

Using quartz density 2.648×10^3 kg/m^3 gives:

$$v_s = \sqrt{\frac{\mu_{\mathrm{AT}}}{\rho_q}} = \sqrt{\frac{2.95 \times 10^{10}}{2.648 \times 10^3}} \approx 3.34 \times 10^3 \text{ m/s} \tag{4.21}$$

The thickness for a crystal with a 5 MHz fundamental frequency, as used in the experiments of this dissertation is ~ 330 μm. When a small, rigid, and uniformly distributed mass Δm adheres to the crystal surface, it effectively increases the oscillating system's inertia, lowering the resonance frequency. For thin films, this frequency shift is given by the Sauerbrey equation [381]:

$$\Delta f = -\frac{2f_0^2}{A\sqrt{\rho_q \mu_q}}\Delta m \tag{4.22}$$

where Δf is the frequency shift, f_0 is the fundamental frequency of the unloaded crystal, A is the active electrode area, ρ_q is the density of quartz, and μ_q is the shear modulus of AT-cut quartz. This can be simplified to a calibration constant

$$\Delta f = -C_f \Delta m \tag{4.23}$$

For a 5 MHz crystal,

$$C_f \approx 56.6 \text{ Hz cm}^2 \mu \text{ g}^{-1} \tag{4.24}$$

An INFICON quartz crystal microbalance (QCM) was used to estimate the coating rate and deposited film thickness for an ytterbium atomic beam incident on both PDMS-coated and bare monitor crystals, which have a thin matte coating of gold. The mass change due to the deposition of ytterbium from the atomic beam= shifts the crystal's resonant frequency in a predictable way, providing a sensitive measurement of the coating thickness on the crystal. Normalized before-and-after measurements of the resonant frequency shift for both coated and bare crystals allow a direct comparison of the fraction of atoms scattered by coated and uncoated surfaces.

Next, a PDMS-coated surface was exposed to an atom beam flux for an extended period, and the degree of coating was measured. The laser ablation of iron powder does not yield the large stable iron atom flux needed to measure such a slow coating rate. An ytterbium beam produced by an atomic oven was used instead[5]

---

[5] For more details, see earlier in Chapter 4.2.

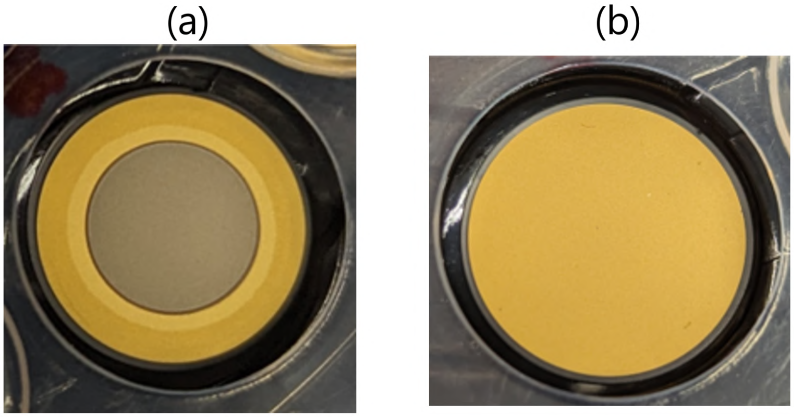

Figure 4.11: Gold-coated QCM crystals exposed to Yb atomic beam. (a) Bare crystal after 100 minutes of exposure: 162 nm film. (b) PDMS-coated crystal after 200 minutes of exposure: no measurable coating.

[375]. Exposing a thickness monitor crystal to the ytterbium atom beam for 100 minutes produced a visible 162 nm coating. For a PDMS-coated surface, even at twice the exposure time, there is no visible coating on the crystal, and no increase in mass in the QCM measurements. This demonstrates that nearly all the atoms interacting with the PDMS surface are scattered. Additionally, the high percentage of atoms scattered is not merely a transient behavior of freshly coated surfaces, persisting for surfaces coated days earlier. The thickness monitor measurements were taken in the dark, eliminating the possibility of light-induced atomic desorption (LIAD) effects. The "non-stick" behavior of the PDMS coating is consistent with the low sticking probability of $\sim 10^{-5}$ at 300 K noted in literature for rubidium on PDMS [382].

4.2.3 Chilled substrates: TEC and LN2

PDMS owes its non-stick and low-adsorption characteristics to low surface energy due to methyl termination. For our atomic beam, this likely explains the observed low sticking probabilities and rapid desorption under vacuum. The relevant processes are thermally activated:

$$S(T) \approx S_0 e^{-E_a/k_B T}, \quad \tau_{\text{res}}(T) = \tau_0 e^{E_{\text{des}}/k_B T} \tag{4.25}$$

where $S(T)$ is the sticking probability, τ_{res} is the mean residence time, and E_{des} is desorption energy, typically in the range $0.1 - 0.4$eV. Residence times for alkali atoms are typically in the microsecond to millisecond range at 300 K . The glass transition temperature of PDMS is approximately -125°C, depending on molecular weight and crosslinking. It is among the lowest glass transition temperature ($\mathrm{T_g}$) values known for any polymer and the primary reason for PDMS's flexibility at low temperatures. Below $\mathrm{T_g}$, chain mobility is reduced, and the surface methyl groups can no longer rearrange to "shed" adsorbates. The sticking probability increases, residence times can reach seconds for some atoms, and the material can trap atoms by physisorption. In vacuum, adsorbate residence times are governed almost entirely by E_{des} . The effective non-stick behavior depends on the interplay between desorption rate and the atomic beam dwell time on the surface. With the PDMS rigid and cold, incident atoms that sample its attractive physisorption well have no thermal energy to escape: at 77 K, $k_B T \approx 0.0066$ eV. The initial sticking probability becomes near-unity for species like Na, K, Rb, and Cs.

$$E_{\text{des}} = 0.20\text{eV} \rightarrow \tau_{\text{res}} \approx 1.2 \text{ s at } 77 \text{ K} \, (\text{vs} \sim 2 \times 10^{-10} \text{ s at } 300 \text{ K}) \tag{4.26}$$

$$E_{\text{des}} = 0.25\text{eV} \rightarrow \tau_{\text{res}} \approx 2.3 \times 10^{3} \text{ s } (\sim 38 \text{ min}) \tag{4.27}$$

$$E_{\text{des}} = 0.35\text{eV} \rightarrow \tau_{\text{res}} \approx 8 \times 10^{9} \text{ s } (\sim 250 \text{ years }) \tag{4.28}$$

We investigated whether ytterbium scattering persists in chilled substrates by mounting the atom beam targets on a liquid nitrogen cold finger. Our cold finger takes roughly three hours to equilibrate to around 100 K from room temperature. This cooling period is long enough to take measurements at different surface temperatures. For every temperature, we detected the presence of atom scattering by observing the fluorescence spectrum of ytterbium. Like the iron spectrum, a broad background

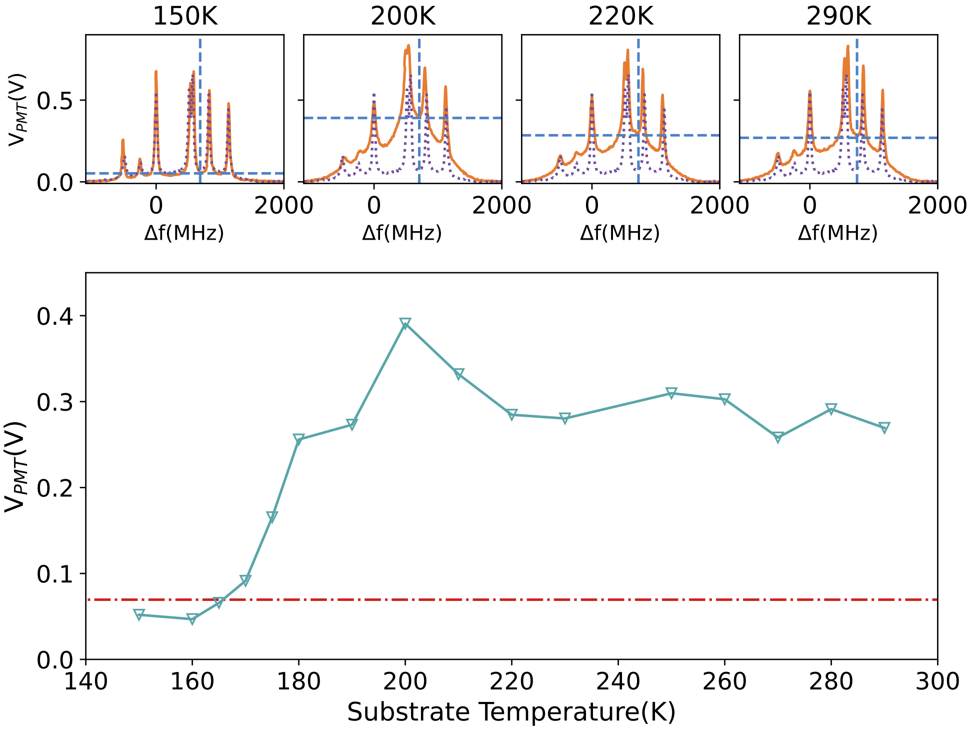

Figure 4.12: Top: Yb fluorescence spectra from PDMS coated thickness monitor crystal. Bottom: maximum intensity of scattered atom fluorescence.

indicates the presence of scattered atoms. Unlike iron, ytterbium has more than one intense isotope peak in its spectrum. Thus, the background cannot be approximated by a single Voigt function, as was done for the iron spectrum. This background fitting makes the temperature estimation of the scattered ytterbium atoms non-trivial.

The top row of Fig. 4.12 shows spectra for ytterbium when the excitation laser is aligned close to where the collimated atoms fall on a thickness monitor crystal coated with a 10% PDMS solution. The y-axis is the PMT voltage without any normalization. Like the iron spectrum, the sharp peaks are due to the collimated incoming atoms, and the broad background is due to the scattered atoms. For reference, a spectrum when the substrate is removed from the path of incoming collimated atoms is plotted with a purple dotted line. The intensity maximum of the background is approximated by the local minima between the isotope peaks ^{173}Yb ($F' = 7/2$) and

^{171}Yb (F$'$ = 3/2). In the representative spectra for a few substrate temperatures shown in the top row of Fig. 4.12, the background intensity maxima are marked with dashed blue lines. The bottom row shows a plot of background intensity maxima versus substrate temperature. The difference between the background intensity maxima and the value for the substrate-less spectrum is proportional to the number of scattered atoms. The number of scattered atoms remains approximately unchanged for substrate temperatures in the range 290 K to 210 K, as the corresponding spectral backgrounds overlap, with similar background intensity maxima. Below 190 K, the background begins to decrease, and spectra below 170 K overlap the substrate-less spectrum. This trend is clearly seen in the background intensity maxima, where below 170 K, the values are comparable to the background intensity maxima of the substrate-less spectrum, shown with a red line. This suggests that below substrate temperatures of 170 K, nearly all ytterbium atoms are being adsorbed on the PDMS surface. This change in scattering from the PDMS surface may be attributable to embrittlement below 200 K [383].

4.3 Numerical model

A simple numerical model provides a demonstration of an interesting potential application for the thermalized scattering behavior of atom beams incident on polymer-coated surfaces. With carefully chosen geometry, a scattering surface placed between a point source of hot atoms[6] and a collimating aperture can produce a beam of thermalized atoms with comparable Doppler width and flux to the hot beam that would result from directly collimating the hot atoms. This provides a temperature reduction at the minor cost of increased geometrical complexity for the collimation setup. As mentioned in the preface to Chapter 4, barring the introduction of ultra-low glass transition silane polymers, the practical limit of temperature reduction is $\sim$ 200 K, and this technique cannot be used as a true cold atom source. Neverthe-

---

[6] As from laser ablation, etc.

less, this effect may have some scientific or technological applications, particularly in trapped atom systems.

Consider a finite square scattering surface of side s and distance d from a rectangular slit of width w and length L. In practice, if the scattering surface dimensions are comparable to the slit-square distance, a larger fraction of scattered particles pass through the slit than from a point source at the same distance. Assume that only those trajectories that intersect the slit opening are transmitted. When the scatterer extends above and below the slit's vertical position, some parts of it "see" the slit at a non-zero polar angle. For a Lambertian point source, the angular distribution of atoms passing through the slit is sharply peaked near zero. For an extended source, surface points lying off-axis view the slit under an angle $\alpha \approx \tan^{-1}(y_0/d)$. Those atoms' mean velocity vectors are tilted by $\pm\alpha$. These small angular deviations contribute an additional spread of line-of-sight velocities:

$$v_{\|} = v_z \cos\alpha + v_y \sin\alpha. \tag{4.29}$$

A distribution of α values adds an extra term to the variance:

$$\sigma_{v\|}^2 = \sigma_{\text{thermal}}^2 + \langle v\rangle^2 \,\mathrm{Var}(\sin\alpha), \tag{4.30}$$

where $\langle v\rangle \approx \sqrt{8k_BT/(\pi m)}$ is the mean speed. The second term is very small because the allowed α is only a few degrees, but it does slightly broaden the Doppler distribution. When $s \ll d$, the "multi-angle" broadening is negligible, and the Doppler width is essentially comparable to that from a point source.

In the numerical model, for purposes of comparison with the scattering case, consider a collimating slit 1 mm wide, 10 mm long, and lying 10 mm above the ablation point. With these parameters, the slit produces a collimated atomic beam consisting of roughly 3.5% of the original flux, with a Doppler width of around 50 MHz . The surface is a square with its midpoint lying some distance above the point

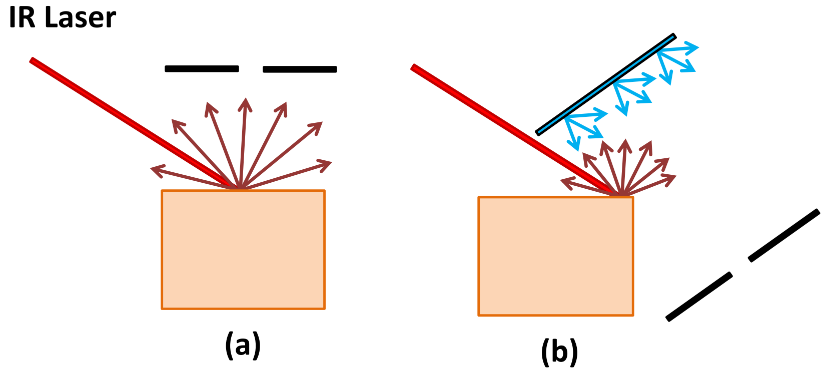

Figure 4.13: (a): Laser ablation and collimation by a slit. (b): Laser ablation followed by scattering from a surface, with subsequent collimation by a slit placed below the line of sight of the ablation point.

of ablation, which scatters atoms towards the collimating slit. This slit is placed parallel to the scattering surface but away from the line of sight of the ablation point, located on the edge of a step, or "cliff," as shown in Fig. 4.13. The surface is angled such that part of the scattered flux reaches the slit, which is below the level of the step.

The flux from the ablation point is assumed to have a cosine distribution with respect to the surface normal [354]. The atoms scattered from the surface are further assumed to thermally equilibrate with the surface, and scatter at room temperature. The scattering surface acts as a kind of extended source; since the scattering is approximated as purely diffuse, each individual point on the surface can be modeled as a Lambertian point source of flux, with a cosine distribution relative to the surface normal. The behavior of the continuous extended source can be approximated with a sufficiently dense grid of scattering points; this example uses 10^6 points. The flux from the ablation point to a point on the scattering surface, and then the scattered fraction which passes through the slit is computed for each point on the scattering surface. The total flux and Doppler broadening through the slit is the sum of the contributions from each of the 10^6 points on the scattering surface. Because the scattering is Lambertian and has angular dependence, the solid angle subtended by the slit for each surface point has to be individually computed, and the flux accepted by the slit appropriately weighted by both the fraction of scattered flux present in the solid angle, but also in the ablated flux intensity impinging on that point. The fraction of the original ablated flux which ultimately passes through the collimating slit can be computed by finding the fraction of the ablated flux which is scattered by the surface, and then the fraction of this scattered flux passing through the collimating slit.

For the scattering system, the scattering surface's height above the ablation point, its angle of tilt, and the dimensions of the surface all affect the Doppler broadening and flux of atoms passing through the slit [7]. If the surface is positioned close to the ablation point, it is possible to achieve parity of flux, or even modest enhancement, relative to the non-scattering case. This is because part of the ablated flux that would otherwise be lost is scattered on a trajectory passing through the slit. Let us choose the surface to be an 8 mm × 8 mm square, with its midpoint 4 mm above the ablation point, and rotated nearly 45° with respect to the vertical. The angle of tilt is set to expose as much as possible of the surface to the ablated flux, while ensuring that every point on the surface has a line of sight to the collimating slit unobstructed by the "cliff" edge. The collimating slit is located 10 mm away from the surface and is parallel to it. The slit length is again 10 mm, but the width is chosen to be 1.2 mm, to match the Doppler width of the slit-only case. For these parameters, the fraction of total flux through the collimating slit is around 5.21%, with a Doppler width again of 50 MHz , meaning that the collimated flux scattered from the surface is improved relative to the case for a slit alone, but at room temperature rather than 1400 K , and with the same degree of Doppler broadening.

---

[7] See Fig. 4.13(b).

Chapter 5: Future Directions

5.1 Push to 1-drop detection

As of the writing of this dissertation, we are on track to achieve one-drop detection of iron isotopes using LIF spectroscopy in early 2026. Improved scanning efficiency, including a novel LIF method, will be added in the coming Spring.

5.2 Ionization spectroscopy

Another intriguing possibility, and the obvious next frontier in sensitivity, is the adaptation of laser ionization spectroscopy to biomedical isotope ratio analysis; unlike LIF, which can only practically capture a limited fraction of the fluorescence emitted into 4π steradians, laser ionization methods have an achievable single-atom detection floor, but also have the isotopic selectivity of LIF.

5.3 Isotope separation

Separation of isotopes of medical interest, including iron, calcium and strontium is being pursued through a variety of methods. Calcium and strontium should see at least preliminary results in 2026; the initial investigation for iron will begin shortly as well.

5.4 Isotope detection in other elements

Relatedly, the methods developed in this dissertation will be adapted to other elements, such as calcium, zinc, and copper; the blood processing methods will need to be evaluated for their applicability to urine and other biosamples.

5.5 Scaleup of blood sample handling

As the LIF spectroscopy methods for ashed blood move closer to being finalized, methods for analyzing many samples at once will need to be developed. One particular area of interest is how to produce a multi-sample holder that is inexpensive, disposable, and durable enough to withstand the rigors of ashing and high vacuum. As mentioned above, a vacuum load-lock system will be implemented to speed the rotation of samples through the system.

Bibliography

[1] Il-Young Kim, Sang-Hoon Suh, In-Kyu Lee, and Robert R Wolfe. Applications of stable, nonradioactive isotope tracers in in vivo human metabolic research. *Experimental & Molecular Medicine*, 48(1):e203–e203, 2016.

[2] George Crișan, Nastasia Sanda Moldovean-Cioroianu, Diana-Gabriela Timaru, Gabriel Andrieș, Călin Căinap, and Vasile Chiș. Radiopharmaceuticals for PET and SPECT imaging: a literature review over the last decade. *International Journal of Molecular Sciences*, 23(9):5023, 2022.

[3] Young Kyung Lim and Dohyeon Kim. Brachytherapy: A comprehensive review. *Progress in Medical Physics*, 32(2):25–39, 2021.

[4] Stanley J. Goldsmith. Targeted radionuclide therapy: a historical and personal review. In *Seminars in Nuclear Medicine*, volume 50, pages 87–97. Elsevier, 2020.

[5] Copenhagen Center for Biomedical Quantum Sensing (CBQS), 2025. URL `https://cbqs.ku.dk/`. Accessed 2025-08-19.

[6] Copenhagen Center for Biomedical Quantum Sensing (CBQS). Our work, 2025. URL `https://cbqs.ku.dk/our-work/`. Accessed 2025-10-05.

[7] Copenhagen Center for Biomedical Quantum Sensing (CBQS). CBQS external collaborators, 2025. URL `https://cbqs.ku.dk/cbqs-external-collaborators/`. Accessed 2025-10-05.

[8] The Pointsman Foundation, 2025. URL `https://www.pointsman.org/`. Accessed 2025-10-06.

[9] Advanced Accelerator Applications USA. Lutathera (lutetium Lu-177 dotatate), 2025. URL `https://us.lutathera.com/`. Accessed 2025-09-10.

[10] Novartis Pharmaceuticals Corporation. Pluvicto (lutetium Lu-177 vipivotide tetraxetan), 2025. URL `https://us.pluvicto.com/`. Accessed 2025-10-03.

[11] Henri Becquerel. Sur les radiations invisible emises par les corps phosphorescents. *Comptes Rendus*, 122:501–503, 1896.

[12] Bain News Service. Sir Ernest Rutherford. URL `https://lccn.loc.gov/2014716719`. George Grantham Bain Collection; glass negative, 5 × 7 in.; no date recorded on caption card; Reproduction No. LC-DIG-ggbain-36570.

[13] The Nobel Prize in Chemistry 1921 — Frederick Soddy. URL `http://www.nobelprize.org/nobel_prizes/chemistry/laureates/1921/soddy.html`. Accessed 2025-10-29.

[14] Herbert N McCoy and WH Ross. The specific radioactivity of thorium and the variation of the activity with chemical treatment and with time. *Journal of the American Chemical Society*, 29(12):1709–1718, 1907.

[15] Daniel Strömholm and The Svedberg. Untersuchungen über die chemie der radioaktiven grundstoffe. i. *Zeitschrift für Anorganische Chemie*, 61(1):338–346, 1909.

[16] Frederick Soddy. The origins of the conceptions of isotopes. Nobel Lecture, December 1922. URL `https://www.nobelprize.org/uploads/2018/06/soddy-lecture.pdf`. Nobelprize.org; accessed 2025-09-10.

[17] Otto Hahn. XIII. On some properties of the α rays of radiothorium.(II.). *The London, Edinburgh, and Dublin Philosophical Magazine and Journal of Science*, 12(67):82–93, 1906.

[18] Henry Gwyn Jeffreys Moseley. XCIII. The high-frequency spectra of the elements. *The London, Edinburgh, and Dublin Philosophical Magazine and Journal of Science*, 26(156):1024–1034, 1913.

[19] Niels Bohr. I. On the constitution of atoms and molecules. *The London, Edinburgh, and Dublin Philosophical Magazine and Journal of Science*, 26(151): 1–25, 1913.

[20] Jagdish Mehra and Helmut Rechenberg. *The Historical Development of Quantum Theory*, volume 1. Springer Science & Business Media, 2000.

[21] American Institute of Physics. AIP Repository Record 53932, Portrait of Henry Moseley, . URL `https://repository.aip.org/node/53932`. Accessed 2025-09-22.

[22] Graham Travers. *Book News*, 20(240):939, 1902.

[23] Death of Dr. Margaret Todd. *Whitstable Times and Herne Bay Herald*, September 1918. Newspaper article.

[24] American Institute of Physics. AIP Repository Record 85591, Joseph Thomson, . URL `https://repository.aip.org/node/85591`. Accessed 2025-10-30.

[25] Joseph John Thomson. Bakerian lecture:—rays of positive electricity. *Proceedings of the Royal Society of London. Series A, Containing Papers of a Mathematical and Physical Character*, 89(607):1–20, 1913.

[26] AIP Repository Record 54889, Aston's Mass Spectrograph, 2025. URL `https://repository.aip.org/node/54889`. Accessed 2025-09-25.

[27] Frederick W. Aston. The constitution of the elements. *Nature*, 104(2616): 393–393, 1919.

[28] F. W. Aston. Isotopes and atomic weights. *Nature*, 105:617–619, July 1920.

[29] Alfred O. Nier and Earl A. Gulbransen. Variations in the relative abundance of the carbon isotopes. *Journal of the American Chemical Society*, 61(3):697–698, 1939.

[30] Maria Goeppert Mayer. Autobiography — Maria Goeppert Mayer, 2025. URL `http://nobelprize.org/nobel_prizes/physics/laureates/1963/mayer-autobio.html`. Accessed 2025-09-15.

[31] U.S. Department of Energy. Lawrence Award, 1966, . URL `https://www.flickr.com/photos/departmentofenergy/11841907935/`. Flickr; DOE photo archive.

[32] U.S. Department of Energy. Harold Urey, Nobel Prize for Chemistry, 1934, . URL `https://www.flickr.com/photos/departmentofenergy/11086396296/`. Flickr; DOE photo archive.

[33] Harold C. Urey. The thermodynamic properties of isotopic substances. *Journal of the Chemical Society (Resumed)*, pages 562–581, 1947.

[34] Jacob Bigeleisen and Maria Goeppert Mayer. *Calculation of Equilibrium Constants for Isotopic Exchange Reactions*, volume 707. Technical Information Division, Oak Ridge Operations, 1947.

[35] Edwin A. Schauble. Applying stable isotope fractionation theory to new systems. *Reviews in Mineralogy and Geochemistry*, 55(1):65–111, 2004.

[36] V.I. Pupyshev, Yu. N. Panchenko, and N.F. Stepanov. A new derivation for the Teller—Redlich isotopic product rule. *Vibrational Spectroscopy*, 7(2):191–196, 1994.

[37] Jacob Bigeleisen. The relative reaction velocities of isotopic molecules. *Journal of Chemical Physics*, 17(8):675, 1949.

[38] Robert D. Guy, Marilyn L. Fogel, and Joseph A. Berry. Photosynthetic fractionation of the stable isotopes of oxygen and carbon. *Plant Physiology*, 101 (1):37–47, 1993.

[39] Mark Pagani. The alkenone-CO_2 proxy and ancient atmospheric carbon dioxide. *Philosophical Transactions of the Royal Society of London. Series A: Mathematical, Physical and Engineering Sciences*, 360(1793):609–632, 2002.

[40] Yi Ge Zhang, Mark Pagani, Zhonghui Liu, Steven M. Bohaty, and Robert DeConto. A 40-million-year history of atmospheric CO_2. *Philosophical Transactions of the Royal Society of London. Series A: Mathematical, Physical and Engineering Sciences*, 371(2001), 2013.

[41] Encyclopaedia Britannica. *Bone Formation — Definition & Physiology*. January 2025.

[42] Standing Committee on the Scientific Evaluation of Dietary Reference Intakes. *Dietary Reference Intakes for Calcium, Phosphorus, Magnesium, Vitamin D, and Fluoride*, volume 565. National Academies Press, 1999.

[43] Mohammad Tinawi. Disorders of calcium metabolism: hypocalcemia and hypercalcemia. *Cureus*, 13(1), 2021.

[44] Tomoka Hasegawa, Hiromi Hongo, Tomomaya Yamamoto, Miki Abe, Hirona Yoshino, Mai Haraguchi-Kitakamae, Hotaka Ishizu, Tomohiro Shimizu, Norimasa Iwasaki, and Norio Amizuka. Matrix vesicle-mediated mineralization and osteocytic regulation of bone mineralization. *International Journal of Molecular Sciences*, 23(17):9941, 2022.

[45] Harry C. Blair, Quitterie C. Larrouture, Yanan Li, Hang Lin, Donna Beer-Stoltz, Li Liu, Rocky S. Tuan, Lisa J. Robinson, Paul H. Schlesinger, and Deborah J. Nelson. Osteoblast differentiation and bone matrix formation in vivo and in vitro. *Tissue Engineering Part B: Reviews*, 23(3):268–280, 2017.

[46] Abhishek Indurkar, Rajan Choudhary, Kristaps Rubenis, and Janis Locs. Role of carboxylic organic molecules in interfibrillar collagen mineralization. *Frontiers in Bioengineering and Biotechnology*, 11:1150037, 2023.

[47] Nikolaus Gussone, Michael E. Böttcher, Anika C. Conrad, Jens Fiebig, Markus Peltz, Georg Grathoff, and Burkhard C. Schmidt. Calcium isotope fractionation upon experimental apatite formation. *Chemical Geology*, 551:119737, 2020.

[48] Joseph Skulan and Donald J. DePaolo. Calcium isotope fractionation between soft and mineralized tissues as a monitor of calcium use in vertebrates. *Proceedings of the National Academy of Sciences*, 96(24):13709–13713, 1999.

[49] Anton Eisenhauer, M. Müller, Alexander Heuser, Ana Kolevica, C-C Glüer, M. Both, C. Laue, U.V. Hehn, S. Kloth, R. Shroff, et al. Calcium isotope ratios in blood and urine: a new biomarker for the diagnosis of osteoporosis. *Bone Reports*, 10:100200, 2019.

[50] Alexander Heuser, Petra Frings-Meuthen, Jörn Rittweger, and Stephen J.G. Galer. Calcium isotopes in human urine as a diagnostic tool for bone loss: additional evidence for time delays in bone response to experimental bed rest. *Frontiers in Physiology*, 10:12, 2019.

[51] Jennifer L.L. Morgan, Joseph L. Skulan, Gwyneth W. Gordon, Stephen J. Romaniello, Scott M. Smith, and Ariel D. Anbar. Rapidly assessing changes in bone mineral balance using natural stable calcium isotopes. *Proceedings of the National Academy of Sciences*, 109(25):9989–9994, 2012.

[52] Marina Ziche, John Jones, and Pietro M Gullino. Role of prostaglandin E1 and copper in angiogenesis. *Journal of the National Cancer Institute*, 69(2): 475–482, 1982.

[53] Vincent Balter, Andre Nogueira da Costa, Victor Paky Bondanese, Klervia Jaouen, Aline Lamboux, Suleeporn Sangrajrang, Nicolas Vincent, François Fourel, Philippe Télouk, Michelle Gigou, et al. Natural variations of copper and sulfur stable isotopes in blood of hepatocellular carcinoma patients. *Proceedings of the National Academy of Sciences*, 112(4):982–985, 2015.

[54] Philippe Télouk, Alain Puisieux, Toshiyuki Fujii, Vincent Balter, Victor P Bondanese, Anne-Pierre Morel, Gilles Clapisson, Aline Lamboux, and Francis Albarede. Copper isotope effect in serum of cancer patients. a pilot study. *Metallomics*, 7(2):299–308, 2015.

[55] Emily Miaou and François L.H. Tissot. Copper isotope ratios in serum do not track cancerous tumor evolution, but organ failure. *Metallomics*, 15(11): mfad060, 2023.

[56] Fiona Larner, Laura N. Woodley, Sami Shousha, Ashley Moyes, Emma Humphreys-Williams, Stanislav Strekopytov, Alex N. Halliday, Mark Rehkämper, and R. Charles Coombes. Zinc isotopic compositions of breast cancer tissue. *Metallomics*, 7 (1):112–117, 2015.

[57] Kathrin Schilling, Fiona Larner, Amina Saad, Rhiannon Roberts, Hemant M. Kocher, Oleg Blyuss, Alex N. Halliday, and Tatjana Crnogorac-Jurcevic. Urine metallomics signature as an indicator of pancreatic cancer. *Metallomics*, 12(5): 752–757, 2020.

[58] Agustina AMB Hastuti, Marta Costas-Rodríguez, Akihiro Matsunaga, Takayuki Ichinose, Shotaro Hagiwara, Mari Shimura, and Frank Vanhaecke. Cu and Zn isotope ratio variations in plasma for survival prediction in hematological malignancy cases. *Scientific Reports*, 10(1):16389, 2020.

[59] Frédéric Moynier, Marie Le Borgne, Esther Lahoud, Brandon Mahan, Francois Mouton-Liger, Jacques Hugon, and Claire Paquet. Copper and zinc isotopic excursions in the human brain affected by Alzheimer's disease. *Alzheimer's & Dementia: Diagnosis, Assessment & Disease Monitoring*, 12(1):e12112, 2020.

[60] Johannes Meyer. Ole Chievitz. *Acta Orthopaedica Scandinavica*, 17(1-4): 173–176, 1948.

[61] Hilde Levi. *George de Hevesy: Life and Work, A Biography.* Rhodos, Copenhagen, 1985.

[62] University of Manchester. *The Physical Laboratories of the University of Manchester: A Record of 25 Years' Work by the University of Manchester.* At the University Press, Manchester, 1906.

[63] George de Hevesy. Some applications of isotopic indicators. In *Nobel Lectures, Chemistry 1942–1962*, pages 525–553. Elsevier Publishing Company, Amsterdam, 1966.

[64] George de Hevesy and F. Paneth. Die löslichkeit des bleisulfids und bleichromats. *Zeitschrift für Anorganische Chemie*, 82:323–328, 1913. English translation by Howard Gest.

[65] Frédéric Joliot and Irène Curie. Artificial production of a new kind of radioelement. *Nature*, 133(3354):201–202, 1934.

[66] O. Chiewitz and G. de Hevesy. Radioactive indicators in the study of phosphorus metabolism in rats. *Nature*, 136(3445):754–755, 1935.

[67] Howard Gest. The early history of ^{32}P as a radioactive tracer in biochemical research: A personal memoir. *Biochemistry and Molecular Biology Education*, 33(3):159–164, 2005.

[68] John B. Livingood. Radioactivity by bombardment. *Electronics*, 8(11):6, November 1935. McGraw-Hill Publishing Co., New York.

[69] Joseph G. Hamilton and Robert S. Stone. Excretion of radio-sodium following intravenous administration in man. *Proceedings of the Society for Experimental Biology and Medicine*, 35(4):595–598, 1937.

[70] Joseph G. Hamilton and Robert S. Stone. The intravenous and intraduodenal administration of radio-sodium. *Radiology*, 28(2):178–188, 1937.

[71] Joseph G. Hamilton. The rates of absorption of radio-sodium in normal human subjects. *Proceedings of the National Academy of Sciences*, 23(9):521–527, 1937.

[72] Joseph G. Hamilton. The rates of absorption of the radioactive isotopes of sodium, potassium, chlorine, bromine, and iodine in normal human subjects. *American Journal of Physiology*, 124(3):667–678, 1938.

[73] Wendell C. Peacock, Robley D. Evans, John W. Irvine, Wilfred M. Good, Arthur F. Kip, Soma Weiss, John G. Gibson, et al. The use of two radioactive isotopes of iron in tracer studies of erythrocytes. *The Journal of Clinical Investigation*, 25(4):605–615, 1946.

[74] Hugh W. Josephs. Absorption of iron as a problem in human physiology: A critical review. *Blood*, 13(1):1–54, 1958.

[75] R.L. Huff, T.G. Hennessy, R.E. Austin, J.F. Garcia, B.M. Roberts, J.H. Lawrence, et al. Plasma and red cell iron turnover in normal subjects and in patients having various hematopoietic disorders. *The Journal of Clinical Investigation*, 29 (8):1041–1052, 1950.

[76] P.F. Hahn, W.M. Balfour, J.F. Ross, W.F. Bale, and G.H. Whipple. Red cell volume circulating and total as determined by radio iron. *Science*, 93(2404): 87–88, 1941.

[77] W.M. Balfour, P.F. Hahn, W.F. Bale, W.T. Pommerenke, and G.H. Whipple. Radioactive iron absorption in clinical conditions: normal, pregnancy, anemia, and hemochromatosis. *The Journal of Experimental Medicine*, 76(1):15, 1942.

[78] William J. Darby, Paul F. Hahn, Margaret M. Kaser, Ruth C. Steinkamp, Paul M. Densen, and Mary B. Cook. The absorption of radioactive iron by children 7–10 years of age: two figures. *The Journal of Nutrition*, 33(1):107–119, 1947.

[79] Robert C. Neerhout, David H. Armstrong, Jeanette Schulz, and Nathan J. Smith. A quantitative study of the fate of recently absorbed food iron. *AMA Journal of Diseases of Children*, 95(2):126–133, 1958.

[80] Jeanette Schulz and Nathan J. Smith. A quantitative study of the absorption of food iron in infants and children. *AMA Journal of Diseases of Children*, 95 (2):109–119, 1958.

[81] Leon M. Sharpe, Wendell C. Peacock, Richard Cooke, and Robert S. Harris. The effect of phytate and other food factors on iron absorption. *The Journal of Nutrition*, 41(3):433–446, 1950.

[82] Lorraine Boissoneault. A Spoonful of Sugar Helps the Radioactive Oatmeal Go Down, March 2017. URL `https://www.smithsonianmag.com/history/spoonful-sugar-helps-radioactive-oatmeal-go-down-180962424/`.

[83] Roadmap to the Project U.S. Department of Energy — Openness: Human Radiation Experiments (OHRE). Chapter 7: The Studies at the Fernald School, 1995. URL `https://ehss.energy.gov/ohre/roadmap/achre/chap7_5.html`.

[84] Presidential Advisory Committee on Human Radiation Experiments; Georgetown University Bioethics Archive. Final report of the advisory committee on human radiation experiments — chapter 7.6, 1995. URL `https://bioethicsarchive.georgetown.edu/achre/final/chap7_6.html`. Accessed 2025-11-01.

[85] Ulrich Flenker. Isotope ratio mass spectrometry–history and terminology in brief. *Drug Testing and Analysis*, 4(12):893–896, 2012.

[86] Jerold C. Woodhead, Jean M. Drulis, Ronald R. Rogers, Ekhard E. Ziegler, Phyllis J. Stumbo, Morteza Janghorbani, Bill T.G. Ting, and Samuel J. Fomon.

Use of the stable isotope, ^{58}Fe, for determining availabilty of nonheme iron in meals. *Pediatric Research*, 23(5):495–499, 1988.

[87] Lu Yang. Accurate and precise determination of isotopic ratios by MC-ICP-MS: A review. *Mass Spectrometry Reviews*, 28(6):990–1011, 2009.

[88] OpenStax. Anatomy & Physiology 2e — Figure 18.7. OpenStax, Rice University, 2019. URL `https://openstax.org/details/books/anatomy-and-physiology-2e`.

[89] David L. Nelson and Michael M. Cox. *Lehninger Principles of Biochemistry.* W. H. Freeman, New York, 7th edition, 2017.

[90] F. Peter Guengerich. Human cytochrome P450 enzymes. In *Cytochrome P450: Structure, Mechanism, and Biochemistry*, pages 523–785. Springer, 2015.

[91] A. Jordan and P. Reichard. Ribonucleotide reductases. *Annual Review of Biochemistry*, 67(1):71–98, 1998.

[92] Christine C. Winterbourn, Anthony J. Kettle, and Mark B. Hampton. Reactive oxygen species and neutrophil function. *Annual Review of Biochemistry*, 85(1): 765–792, 2016.

[93] M. Indriati Hood and Eric P. Skaar. Nutritional immunity: transition metals at the pathogen–host interface. *Nature Reviews Microbiology*, 10(8):525–537, 2012.

[94] John L. Beard. Iron biology in immune function, muscle metabolism and neuronal functioning. *The Journal of Nutrition*, 131(2):568S–580S, 2001.

[95] Elaine K. McCarthy, Deirdre M. Murray, and Mairead E. Kiely. Iron deficiency during the first 1000 days of life: are we doing enough to protect the developing brain? *Proceedings of the Nutrition Society*, 81(1):108–118, 2022.

[96] Betsy Lozoff, John Beard, James Connor, Barbara Felt, Michael Georgieff, and Timothy Schallert. Long-lasting neural and behavioral effects of iron deficiency in infancy. *Nutrition Reviews*, 64(5), 2006.

[97] Sally Grantham-McGregor and Cornelius Ani. A review of studies on the effect of iron deficiency on cognitive development in children. *The Journal of Nutrition*, 131(2):649S–668S, 2001.

[98] World Health Organization. *Guideline Daily Iron Supplementation in Infants and Children*. World Health Organization, 2016.

[99] John L. Beard and James R. Connor. Iron status and neural functioning. *Annual Review of Nutrition*, 23(1):41–58, 2003.

[100] Betsy Lozoff, Elias Jimenez, and Abraham W. Wolf. Long-term developmental outcome of infants with iron deficiency. *New England Journal of Medicine*, 325 (10):687–694, 1991.

[101] Raghavendra Rao, Ivan Tkac, Elise L. Townsend, Rolf Gruetter, and Michael K. Georgieff. Perinatal iron deficiency alters the neurochemical profile of the developing rat hippocampus. *The Journal of Nutrition*, 133(10):3215–3221, 2003.

[102] Betsy Lozoff, Elias Jimenez, John Hagen, Eileen Mollen, and Abraham W. Wolf. Poorer behavioral and developmental outcome more than 10 years after treatment for iron deficiency in infancy. *Pediatrics*, 105(4):e51–e51, 2000.

[103] World Health Organization. *Accelerating Anaemia Reduction: a Comprehensive Framework for Action*. World Health Organization, 2023.

[104] Gretchen A. Stevens, Ty Beal, Mduduzi N.N. Mbuya, Hanqi Luo, Lynnette M. Neufeld, O. Yaw Addo, Seth Adu-Afarwuah, Silvia Alayón, Zulfiqar Bhutta,

Kenneth H. Brown, et al. Micronutrient deficiencies among preschool-aged children and women of reproductive age worldwide: a pooled analysis of individual-level data from population-representative surveys. *The Lancet Global Health*, 10(11):e1590–e1599, 2022.

[105] Institute for Health Metrics and Evaluation (IHME). Local Burden of Disease (LBD) — Anemia, 2025. URL `https://vizhub.healthdata.org/lbd/anemia`.

[106] Anne M. Williams, Nicholas Ansai, Namanjeet Ahluwalia, and Duong T. Nguyen. Anemia Prevalence: United States, August 2021-August 2023. *NCHS data brief*, (519), 2024.

[107] Nicole Kline, Kevin Meyers Mathieu, and Jeff Marr. WIC Participant and Program Characteristics: 2018 Food Packages and Costs, 2020.

[108] Susan Horton and Jay Ross. The economics of iron deficiency. *Food Policy*, 28 (1):51–75, 2003.

[109] Meera Shekar, Jakub Kakietek, Julia Dayton Eberwein, and Dylan Walters. *An Investment Framework for Nutrition: Reaching the Global Targets for Stunting, Anemia, Breastfeeding, and Wasting.* World Bank Publications, 2017.

[110] Meera Shekar, Richard Heaver, Yi-Kyoung Lee, et al. *Repositioning Nutrition as Central to Development: A Strategy for Large Scale Action.* World Bank Publications, 2006.

[111] V. Reggie Edgerton, G.W. Gardner, Yoshinobu Ohira, K.A. Gunawardena, and B. Senewiratne. Iron-deficiency anaemia and its effect on worker productivity and activity patterns. *British Medical Journal*, 2(6204):1546–1549, 1979.

[112] Md Mizanur Rahman, Sarah Krull Abe, Md Shafiur Rahman, Mikiko Kanda, Saki Narita, Ver Bilano, Erika Ota, Stuart Gilmour, and Kenji Shibuya. Ma-

ternal anemia and risk of adverse birth and health outcomes in low-and middle-income countries: systematic review and meta-analysis. *The American Journal of Clinical Nutrition*, 103(2):495–504, 2016.

[113] Eva Hertrampf. Iron fortification in the Americas. *Nutrition Reviews*, 60 (suppl_7):S22–S25, 2002.

[114] Richard Hurrell and Ines Egli. Iron bioavailability and dietary reference values. *The American Journal of Clinical Nutrition*, 91(5):1461S–1467S, 2010.

[115] Richard F. Hurrell, Manju Reddy, and James D. Cook. Inhibition of non-haem iron absorption in man by polyphenolic-containing beverages. *British Journal of Nutrition*, 81(4):289–295, 1999.

[116] Diego Moretti, Jeroen S. Goede, Christophe Zeder, Markus Jiskra, Vaiya Chatzinakou, Harold Tjalsma, Alida Melse-Boonstra, Gary Brittenham, Dorine W. Swinkels, and Michael B. Zimmermann. Oral iron supplements increase hepcidin and decrease iron absorption from daily or twice-daily doses in iron-depleted young women. *Blood, The Journal of the American Society of Hematology*, 126(17):1981–1989, 2015.

[117] Lena Davidsson, Triantafillia Dimitriou, Erick Boy, Thomas Walczyk, and Richard F. Hurrell. Iron bioavailability from iron-fortified Guatemalan meals based on corn tortillas and black bean paste. *The American Journal of Clinical Nutrition*, 75 (3):535–539, 2002.

[118] Meredith C. Fidler, Lena Davidsson, Thomas Walczyk, and Richard F. Hurrell. Iron absorption from fish sauce and soy sauce fortified with sodium iron EDTA. *The American Journal of Clinical Nutrition*, 78(2):274–278, 2003.

[119] Omar Dary and Richard Hurrell. Guidelines on food fortification with micronutrients. *World Health Organization, Food and Agricultural Organization of the United Nations: Geneva, Switzerland*, 2006:1–376, 2006.

[120] Salvador Villalpando, Teresa Shamah-Levy, Claudia Ivonne Ramírez-Silva, Fabiola Mejía-Rodríguez, and Juan A. Rivera. Prevalence of anemia in children 1 to 12 years of age: results from a nationwide probabilistic survey in Mexico. *Salud pública de México*, 45:490–498, 2003.

[121] Juan Rivera Dommarco and Teresa Shamah Levy. Presentación de resultados de la encuesta nacional de nutrición 1999: Estado nutricio de niños y mujeres en México. *Salud Pública de México*, 44:188–189, 2002.

[122] Manual para el suministro y control del suplemento alimenticio, 2017. URL `https://www.gob.mx/cms/uploads/attachment/file/218143/Manual_para_el_suministro_y_control_del_suplemento_alimenticio_2017.pdf`.

[123] Steven A. Abrams. New approaches to iron fortification: role of bioavailability studies. *The American Journal of Clinical Nutrition*, 80(5):1104–1105, 2004.

[124] Ana B. Perez-Exposito, Salvador Villalpando, Juan A. Rivera, Ian J. Griffin, and Steven A. Abrams. Ferrous sulfate is more bioavailable among preschoolers than other forms of iron in a milk-based weaning food distributed by PROGRESA, a national program in Mexico. *The Journal of Nutrition*, 135(1): 64–69, 2005.

[125] Teresa Shamah-Levy, Salvador Villalpando, Juan A. Rivera-Dommarco, Verónica Mundo-Rosas, Lucia Cuevas-Nasu, and Alejandra Jiménez-Aguilar. Ferrous gluconate and ferrous sulfate added to a complementary food distributed by the Mexican nutrition program Oportunidades have a comparable efficacy to reduce iron deficiency in toddlers. *Journal of Pediatric Gastroenterology and Nutrition*, 47(5):660–666, 2008.

[126] Ayoub Al Jawaldeh, Juan Pablo Peña-Rosas, Karen McColl, Quentin Johnson, Ibrahim Elmadfa, and Lara Nasreddine. Wheat flour fortification in the eastern Mediterranean region, April 2019. URL `https://pesquisa.bvsalud.org/portal/resource/pt/who-311730`.

[127] Meryem Lazrak, Khalid El Kari, Nicole U. Stoffel, Laila Elammari, Ayoub Al-Jawaldeh, Cornelia U. Loechl, Abdelhakim Yahyane, Amina Barkat, Michael B. Zimmermann, and Hassan Aguenaou. Tea consumption reduces iron bioavailability from NaFeEDTA in nonanemic women and women with iron deficiency anemia: Stable iron isotope studies in Morocco. *The Journal of Nutrition*, 151 (9):2714–2720, 2021.

[128] Aish.com. Moroccan mint tea (image), August 2024. URL `https://aish.com/wp-content/uploads/2024/08/Moroccan-Mint-Tea-1240_x_698.jpg`. Accessed 2025-11-04.

[129] Food and Agriculture Organization of the United Nations (FAO). Committee on Commodity Problems: Intergovernmental Group on Tea — Current Market Situation and Medium-Term Outlook, 2018. FAO report.

[130] P. B. Disler, S. R. Lynch, J. D. Torrance, T. H. Bothwell, R. W. Charlton, and R. B. Walker. The effect of tea on iron absorption. *The Lancet*, 2(7933): 123–126, 1975.

[131] Appui à la politique du maroc pour lutter contre les carences en micronutriments, 2025. URL `https://www.iaea.org/fr/newscenter/news/appui-a-la-politique-du-maroc-pour-lutter-contre-les-carences-en-micronutriments`. Accessed 2025-08-11.

[132] Stanley Zlotkin and Kathryn G. Dewey. Perspective: Putting the youngest among us into the nutrition “call for action” for food fortification strategies. *The American Journal of Clinical Nutrition*, 114(4):1257–1260, 2021.

[133] Helena Pachón, Rebecca Spohrer, Zuguo Mei, and Mary K Serdula. Evidence of the effectiveness of flour fortification programs on iron status and anemia: a systematic review. *Nutrition Reviews*, 73(11):780–795, 2015.

[134] WHO Guideline. Use of Multiple Micronutrient Powders for Point-of-Use Fortification of Foods Consumed by Infants and Young Children Aged 6–23 Months and Children Aged 2–12 Years. *World Health Organization: Geneva, Switzerland*, 2016.

[135] Patsy M. Brannon, Patrick J. Stover, and Christine L. Taylor. Integrating themes, evidence gaps, and research needs identified by workshop on iron screening and supplementation in iron-replete pregnant women and young children. *The American Journal of Clinical Nutrition*, 106:1703S–1712S, 2017.

[136] UNICEF et al. Improving Young Children's Diets During the Complementary Feeding Period. *UNICEF Programming Guidance*, 76:118–122, 2020.

[137] Tomas Ganz. Hepcidin and iron regulation, 10 years later. *Blood, The Journal of the American Society of Hematology*, 117(17):4425–4433, 2011.

[138] Keith J. Collard. Iron homeostasis in the neonate. *Pediatrics*, 123(4):1208–1216, 2009.

[139] Sunil Sazawal, Robert E. Black, Mahdi Ramsan, Hababu M. Chwaya, Rebecca J. Stoltzfus, Arup Dutta, Usha Dhingra, Ibrahim Kabole, Saikat Deb, Mashavi K. Othman, et al. Effects of routine prophylactic supplementation with iron and folic acid on admission to hospital and mortality in preschool children in a high malaria transmission setting: community-based, randomised, placebo-controlled trial. *The Lancet*, 367(9505):133–143, 2006.

[140] Ami Neuberger, Joseph Okebe, Dafna Yahav, and Mical Paul. Oral iron supplements for children in malaria-endemic areas. *Cochrane Database of Systematic Reviews*, (2), 2016.

[141] Rebecca D. Merrill, Rachel M. Burke, Christine A. Northrop-Clewes, Pura Rayco-Solon, Rafael Flores-Ayala, Sorrel M.L. Namaste, Mary K. Serdula, and

Parminder S. Suchdev. Factors associated with inflammation in preschool children and women of reproductive age: Biomarkers reflecting inflammation and nutritional determinants of anemia (BRINDA) project. *The American Journal of Clinical Nutrition*, 106:348S–358S, 2017.

[142] World Health Organization et al. *WHO Guideline on Use of Ferritin Concentrations to Assess Iron Status in Populations*. World Health Organization, 2020.

[143] Jody A. Rusch, Diederick J. van der Westhuizen, Robert S. Gill, and Vernon J. Louw. Diagnosing iron deficiency: Controversies and novel metrics. *Best Practice & Research Clinical Anaesthesiology*, 37(4):451–467, 2023.

[144] Centers for Disease Control and Prevention (CDC). Recommendations to prevent and control iron deficiency in the United States. *MMWR Recomm Report*, 47:1–29, 1998.

[145] Robert S. Hillman and Kenneth A. Ault. *Hematology in Clinical Practice: A Guide to Diagnosis and Management*. McGraw-Hill Medical, New York, 5th edition, 2010.

[146] Leida Tandara and Ilza Salamunić. Iron metabolism: current facts and future directions. *Biochemia Medica*, 22(3):311–328, 2012.

[147] Cristina Rosário, Gisele Zandman-Goddard, Esther G Meyron-Holtz, David P D'Cruz, and Yehuda Shoenfeld. The hyperferritinemic syndrome: macrophage activation syndrome, still's disease, septic shock and catastrophic antiphospholipid syndrome. *BMC Medicine*, 11(1):185, 2013.

[148] Richard T. O'Brien and Howard A. Pearson. Physiologic anemia of the newborn infant. *The Journal of Pediatrics*, 79(1):132–138, 1971.

[149] Josh M. Jorgensen, Mayra Crespo-Bellido, and Kathryn G. Dewey. Variation in hemoglobin across the life cycle and between males and females. *Annals of the New York Academy of Sciences*, 1450(1):105–125, 2019.

[150] The Hong Kong Polytechnic University Department of Civil and Environmental Engineering. Advanced Environmental Engineering Laboratories, February 2024. URL `https://www.polyu.edu.hk/cee/-/media/department/cee/about-cee/facilities/2024/lab-2-lab-4--lab-15-advenvlabs__feb2024.pdf`.

[151] Magnus Domellöf, Bo Lönnerdal, Steven A. Abrams, and Olle Hernell. Iron absorption in breast-fed infants: effects of age, iron status, iron supplements, and complementary foods. *The American Journal of Clinical Nutrition*, 76(1): 198–204, 2002.

[152] LEIF Hallberg, MATS Brune, and LENA Rossander. The role of vitamin C in iron absorption. *International Journal for Vitamin and Nutrition Research.*, 30:103–108, 1989.

[153] Sean R. Lynch and James D. Cook. Interaction of vitamin C and iron. *Annals of the New York Academy of Sciences*, 355(1):32–44, 1980.

[154] Tomas Walter, Fernando Pizarro, Steven A. Abrams, and Erick Boy. Bioavailability of elemental iron powder in white wheat bread. *European Journal of Clinical Nutrition*, 58(3):555–558, 2004.

[155] Lena Davidsson, Pilar Galan, Françoise Cherouvrier, Peter Kastenmayer, Marcel A. Juillerat, Serge Hercberg, and Richard F. Hurrell. Bioavailability in infants of iron from infant cereals: effect of dephytinization. *The American Journal of Clinical Nutrition*, 65(4):916–920, 1997.

[156] Lena Davidsson, Peter Kastenmayer, Hanna Szajewska, Richard F. Hurrell, and Denis Barclay. Iron bioavailability in infants from an infant cereal fortified with

ferric pyrophosphate or ferrous fumarate. *The American Journal of Clinical Nutrition*, 71(6):1597–1602, 2000.

[157] Diego Moretti, Michael B Zimmermann, Rita Wegmüller, Thomas Walczyk, Christophe Zeder, and Richard F. Hurrell. Iron status and food matrix strongly affect the relative bioavailability of ferric pyrophosphate in humans. *The American Journal of Clinical Nutrition*, 83(3):632–638, 2006.

[158] Steven A. Abrams, Kimberly O. O'Brien, Jianping Wen, Lily K. Liang, and Janice E. Stuff. Absorption by 1-year-old children of an iron supplement given with cow's milk or juice. *Pediatric Research*, 39(1):171–175, 1996.

[159] Steven A. Abrams. Using stable isotopes to assess mineral absorption and utilization by children. *The American Journal of Clinical Nutrition*, 70(6): 955–964, 1999.

[160] Lena Davidsson, Pilar Galan, Peter Kastenmayer, Françoise Cherouvrier, Marcel A. Juillerat, Serge Hercberg, and Richard F. Hurrell. Iron bioavailability studied in infants: the influence of phytic acid and ascorbic acid in infant formulas based on soy isolate. *Pediatric Research*, 36(6):816–822, 1994.

[161] Morteza Janghorbani, Bill T.G. Ting, and Samuel J. Fomon. Erythrocyte incorporation of ingested stable isotope of iron (^{58}Fe). *American Journal of Hematology*, 21(3):277–288, 1986.

[162] Peter Kastenmayer, Lena Davidsson, Pilar Galanz, Françise Cherouvrier, Serge Hercberg, and Richard F. Hurrell. A double stable isotope technique for measuring iron absorption in infants. *British Journal of Nutrition*, 71(3):411–424, 1994.

[163] Ellen van den Heuvel, Theo Muys, Hillie Pellegrom, Joost P. Bruyntjes, Wim Van Dokkum, Steven Spanhaak, and Gertjan Schaafsma. A new method to

measure iron absorption from the enrichment of 57Fe and 58Fe in young erythroid cells. *Clinical Chemistry*, 44(3):649–654, 1998.

[164] Lena Davidsson, Ekhard E. Ziegler, Peter Kastenmayer, and Richard F. Hurrell. Erythrocyte incorporation of iron by infants: iron bioavailability from a low-iron infant formula and an evaluation of the usefulness of correcting erythrocyte incorporation values, using a reference dose or plasma ferritin concentrations. *British Journal of Nutrition*, 84(6):847–853, 2000.

[165] Samuel B. Nadler, John U. Hidalgo, and Ted Bloch. Prediction of blood volume in normal human adults. *Surgery*, 51(2):224–232, 1962.

[166] O. Linderkamp, H.T. Versmold, K.P. Riegel, and K. Betke. Estimation and prediction of blood volume in infants and children. *European Journal of Pediatrics*, 125(4):227–234, 1977.

[167] Thomas R.C. Sisson, Curtis J. Lund, Lorraine E. Whalen, and Amalia Telek. The blood volume of infants: I. the full-term infant in the first year of life. *The Journal of Pediatrics*, 55(2):163–179, 1959.

[168] R.M. Rowan, C. Fraser, J.H. Gray, and G.A. McDonald. The Coulter Counter Model S Plus–the shape of things to come. *Clinical and Laboratory Haematology*, 1(1):29–40, 1979.

[169] Wallace H. Coulter. Means for Counting Particles Suspended in a Fluid, October 20 1953. US Patent 2,656,508.

[170] Marshall Don. The Coulter principle: foundation of an industry. *JALA: Journal of the Association for Laboratory Automation*, 8(6):72–81, 2003.

[171] T. Lehto and P. Hedberg. Performance evaluation of Abbott CELL-DYN Ruby for routine use. *International Journal of Laboratory Hematology*, 30(5): 400–407, 2008.

[172] Howard M. Shapiro. *Practical Flow Cytometry.* Wiley-Liss, Hoboken, NJ, 4th edition, 2003.

[173] Lynnea Waters. Demystifying the flow cytometry optics system: A peek under the hood, January 2025. URL `https://bitesizebio.com/31638/flow-cytometry-optics-system/`. Bitesize Bio.

[174] Marion G. Macey. *Flow Cytometry.* Springer, Berlin, Germany, 2007.

[175] UK Government — Contracts Finder. Contracts Finder Notice c9a37858-2e84-401d-b763-34e2f5d1374f. URL `https://www.contractsfinder.service.gov.uk/Notice/c9a37858-2e84-401d-b763-34e2f5d1374f`. Accessed 2025-10-06.

[176] S. Weyer and J.B. Schwieters. High precision Fe isotope measurements with high mass resolution MC-ICPMS. *International Journal of Mass Spectrometry*, 226(3):355–368, 2003.

[177] Nicolas Dauphas and Olivier Rouxel. Mass spectrometry and natural variations of iron isotopes. *Mass Spectrometry Reviews*, 25(4):515–550, 2006.

[178] Yu-Hsuan Liang, Kuan-Ying A. Huang, Der-Chuen Lee, Kwan-Nang Pang, and Shih-Hsiang Chen. High-precision iron isotope analysis of whole blood, erythrocytes, and serum in adults. *Journal of Trace Elements in Medicine and Biology*, 58:126421, 2020.

[179] Thomas Walczyk and Friedhelm von Blanckenburg. Natural iron isotope variations in human blood. *Science*, 295(5562):2065–2066, 2002.

[180] Takeshi Ohno, Atsuko Shinohara, Ichitaro Kohge, Momoko Chiba, and Takafumi Hirata. Isotopic analysis of Fe in human red blood cells by multiple collector-ICP-mass spectrometry. *Analytical Sciences*, 20(4):617–621, 2004.

[181] Stephen R.C. Howie. Blood sample volumes in child health research: review of safe limits. *Bulletin of the World Health Organization*, 89:46–53, 2011.

[182] Clinical and Laboratory Standards Institute (CLSI). *Collection of Capillary Blood Specimens*. Number GP42. Wayne, PA, 7th edition, 2020.

[183] Ruth E. McCall and Cathey M. Tankersley. *Phlebotomy Essentials*. Jones Bartlett Learning, 8th edition, 2023.

[184] World Health Organization. WHO Guidelines on Drawing Blood: Best Practices in Phlebotomy. pages 130–130. 2010.

[185] Clinical and Laboratory Standards Institute (CLSI). *Procedures and Devices for the Collection of Diagnostic Capillary Blood Specimens*. Number GP42-A6. Wayne, PA, 6 edition, 2019.

[186] Committee on Fetus, Newborn, Section on Anesthesiology, Pain Medicine, Erin Keels, Navil Sethna, Kristi L. Watterberg, James J. Cummings, William E. Benitz, Eric C. Eichenwald, Brenda B. Poindexter, Dan L. Stewart, Susan W. Aucott, et al. Prevention and management of procedural pain in the neonate: an update. *Pediatrics*, 137(2):e20154271, 2016.

[187] Enrico Schalk, Katrin Scheinpflug, and Martin Mohren. Capillary blood count analyses in clinical practice: a safe, reliable and valid method 1. *Journal of Laboratory Medicine/Laboratoriums Medizin*, 33(5), 2009.

[188] WIRED. Police used a baby's DNA to investigate its father for a crime, 2025. URL `https://www.wired.com/story/police-used-a-babys-dna-to-investigate-its-father-for-a-crime/`. Accessed 2025-10-22.

[189] NIDirect Government Services (Northern Ireland Government). Newborn screening, 2025. URL `https://www.nidirect.gov.uk/articles/newborn-screening`. Accessed 2025-11-02.

[190] Clinical and Laboratory Standards Institute (CLSI). Blood collection on filter paper for newborn screening programs, 2013. CLSI document NBS01-A6.

[191] Robert Guthrie and Ada Susi. A simple phenylalanine method for detecting phenylketonuria in large populations of newborn infants. *Pediatrics*, 32(3): 338–343, 1963.

[192] B.W. Adam, E.M. Hall, M. Sternberg, T.H. Lim, S.R. Flores, S. O'Brien, D. Simms, L.X. Li, V.R. De Jesus, and W.H. Hannon. The stability of markers in dried-blood spots for recommended newborn screening disorders in the United States. *Clinical Biochemistry*, 44(17-18):1445–1450, 2011.

[193] Neil Spooner, Rakesh Lad, and Matt Barfield. Dried blood spots as a sample collection technique for the determination of pharmacokinetics in clinical studies: considerations for the validation of a quantitative bioanalytical method. *Analytical Chemistry*, 81(4):1557–1563, 2009.

[194] Aongart Mahittikorn, Frederick Ramirez Masangkay, Kwuntida Uthaisar Kotepui, Giovanni De Jesus Milanez, and Manas Kotepui. Comparative performance of PCR using DNA extracted from dried blood spots and whole blood samples for malaria diagnosis: a meta-analysis. *Scientific Reports*, 11(1):4845, 2021.

[195] M. Aramendía, L. Rello, Sylvain Bérail, A. Donnard, Christophe Pécheyran, and M. Resano. Direct analysis of dried blood spots by femtosecond-laser ablation-inductively coupled plasma-mass spectrometry: feasibility of split-flow laser ablation for simultaneous trace element and isotopic analysis. *Journal of Analytical Atomic Spectrometry*, 30(1):296–309, 2015.

[196] Sarah M. Lofgren, Anne B. Morrissey, Caroline C. Chevallier, Anangisye I. Malabeja, Sally Edmonds, Ben Amos, David J. Sifuna, Lorenz Von Seidlein, Werner Schimana, Wendy S. Stevens, et al. Evaluation of a dried blood spot HIV-1 RNA program for early infant diagnosis and viral load monitoring at rural and remote healthcare facilities. *AIDS*, 23(18):2459–2466, 2009.

[197] World Health Organization (WHO). Guidelines on Hepatitis B and C Testing, 2017.

[198] E.M. Tanvir, Tatiana Komarova, Eva Comino, Ronald Sumner, Karen M. Whitfield, and P. Nicholas Shaw. Effects of storage conditions on the stability and distribution of clinical trace elements in whole blood and plasma: Application of ICP-MS. *Journal of Trace Elements in Medicine and Biology*, 68:126804, 2021.

[199] Rhode Island Department of Health. Lead, Whole Blood, Capillary — Department of Health, September 2025. URL `https://health.ri.gov/laboratory-testing/clinical-specimen-submission-guidance/lead-whole-blood-capillary`. Accessed 2025-10-11.

[200] Johan Björkesten, Stefan Enroth, Qiujin Shen, Lotta Wik, David M. Hougaard, Arieh S. Cohen, Lene Sörensen, Vilmantas Giedraitis, Martin Ingelsson, Anders Larsson, et al. Stability of proteins in dried blood spot biobanks. *Molecular & Cellular Proteomics*, 16(7):1286–1296, 2017.

[201] World Health Organization (WHO). *WHO Guidelines on Drawing Blood: Best Practices in Phlebotomy.* WHO Press, Geneva, 2010.

[202] Centers for Disease Control and Prevention (CDC). Dried Specimen Shipping — Poster, March 2025. URL `https://www.cdc.gov/laboratory-quality-assurance/media/pdfs/2025/03/Poster-Dried-Shipping-508.pdf`. CDC Laboratory Quality Assurance.

[203] International Air Transport Association (IATA). Dangerous Goods Regulations (DGR), 66th Edition — Section 3.6.2, 2025. URL `https://www.iata.org/contentassets/b08040a138dc4442a4f066e6fb99fe2a/dgr-66-en-3.6.2.pdf`.

[204] CWI Medical. GE Bio-Sciences Blood Stain Card (GE-BLDCARD). URL `https://www.cwimedical.com/blood-collection-products/ge-bio-sciences-blood-stain-card-ge-bldcard`.

[205] TruLaboratories Corporation. Capillary Tubes and Sealing Wax. URL `https://www.trulaboratories.com/component/virtuemart/blood-collection/capillary-tubes-and-sealing-wax-detail.html?Itemid=0`.

[206] Clinical and Laboratory Standards Institute (CLSI). *Dried Blood Spot Specimen Collection for Newborn Screening*. Number NBS01. Malvern, PA, 7th edition, 2021.

[207] M. O'Mara, B. Hudson-Curtis, K. Olson, Y. Yueh, J. Dunn, and N. Spooner. The effect of hematocrit and punch location on assay bias during quantitative bioanalysis of dried blood spot samples. *Bioanalysis*, 3(20):2335–2347, 2011.

[208] George de Hevesy. The absorption and translocation of lead by plants: A contribution to the application of the method of radioactive indicators in the investigation of the change of substance in plants. *Biochemical Journal*, 17 (4-5):439, 1923.

[209] Mario E. Austoni and David M. Greenberg. Studies in iron metabolism with the aid of its artificial radioactive isotope: The absorption, excretion, and distribution of iron in the rat on normal and iron-deficient diets. *Journal of Biological Chemistry*, 134(1):27–41, 1940.

[210] National Institute of Standards and Technology (NIST). Composition of BLOOD (ICRP) — STAR Database, 2025. URL `https://physics.nist.gov/cgi-bin/Star/compos.pl?matno=118`.

[211] Stefanie A. Bragg and Zi-Ling Xue. Optimization of dry ashing of whole blood samples for trace metal analysis. *American Journal of Analytical Chemistry*, 2 (8):979, 2011.

[212] Innovative Research, 2025. URL `https://www.innov-research.com`. Accessed 2025-10-07.

[213] Carbolite Gero Ltd. Ashing Furnace AAF — 3 & 7 litres (AAF 11/3 & AAF 11/7), 2025. URL `https://www.carbolite.com/products/chamber-furnaces/ashing-furnaces/aaf-11-3-11-7/`.

[214] McMaster-Carr Supply Company. Micropipettes, 2025. URL `https://www.mcmaster.com/products/micropipettes/micropipettes-6/`. Product catalog page.

[215] McMaster-Carr Supply Company. Rods (Glass, Mica, Ceramic), 2025. URL `https://www.mcmaster.com/products/rods/material~glass-mica-ceramic/`. Product catalog page.

[216] S.R. Koirtyohann and Carole A. Hopkins. Losses of trace metals during the ashing of biological materials. *Analyst*, 101(1208):870–875, 1976.

[217] L. Vesterberg and T. Bergström. Determination of cadmium in blood by use of atomic absorption spectroscopy with crucibles–and a rational procedure for dry-ashing. *Clinical Chemistry*, 23(3):555–559, 1977.

[218] U.S. Environmental Protection Agency. Laboratory sample preparation. In *Multi-Agency Radiological Laboratory Analytical Protocols (MARLAP) Manual, Volume II*, number EPA 402-B-04-001B, chapter 12. Washington, DC, July 2004. URL `https://www.epa.gov/sites/default/files/2015-05/documents/402-b-04-001b-12-final.pdf`.

[219] National Environmental Methods Index (NEMI). NEMI Method Summary 4696, 2025. URL `https://www.nemi.gov/methods/method_summary/4696`. Accessed 2025-08-20.

[220] Lars Jorhem, G. Afthan, G. Cumont, H.P. Dypdahl, K. Gadd, G.N. Havre, K. Julshamn, K. Kåverud, B. Lind, J. Loimaranta, M. Merseburg, A. Olsson, S. Piepponen, B. Sundström, B.J. Uppstad, T. Waaler, and L. Winnerstam. Determination of metals in foods by atomic absorption spectrometry after dry ashing: NMKL1 collaborative study. *Journal of AOAC International*, 83(5): 1204–1211, 2000.

[221] Sigma-Aldrich (MilliporeSigma). Iron(III) oxide, powder, $< 5\mu\text{m}, \geq 96\%$ (Product No. 310050). URL `https://www.sigmaaldrich.com/US/en/product/sigald/310050`. CAS 1309-37-1; Fe_2O_3.

[222] T. Stehrer, B. Praher, R. Viskup, J. Jasik, H. Wolfmeir, E. Arenholz, J. Heitz, and J.D. Pedarnig. Laser-induced breakdown spectroscopy of iron oxide powder. *Journal of Analytical Atomic Spectrometry*, 24(7):973–978, 2009.

[223] Michaël Susset, Axelle Leduc-Gauthier, Anne-Claire Humbert, Fabien Pointurier, and Christophe Pécheyran. Comparison of the fluctuations of the signals measured by icp-ms after laser ablation of powdered geological materials prepared by four methods. *Analytical Sciences*, 39(6):999–1014, 2023.

[224] Kazumi Ito, Noriko Hasebe, Ryosuke Sumita, Shoji Arai, Masayoshi Yamamoto, Kenji Kashiwaya, and Yoshihiro Ganzawa. LA-ICP-MS analysis of pressed powder pellets to luminescence geochronology. *Chemical Geology*, 262(3-4): 131–137, 2009.

[225] C.D. Boley, Saad A. Khairallah, and Alexander M. Rubenchik. Calculation of laser absorption by metal powders in additive manufacturing. *Applied Optics*, 54(9):2477–2482, 2015.

[226] A.V. Gusarov, I. Yadroitsev, P. Bertrand, and I. Smurov. Model of radiation and heat transfer in laser-powder interaction zone at selective laser melting. *Journal of Heat Transfer*, 131:072101–1, 2009.

[227] Benedikt Brandau, Adrien Da Silva, Christoph Wilsnack, Frank Brueckner, and Alexander FH Kaplan. Absorbance study of powder conditions for laser additive manufacturing. *Materials & Design*, 216:110591, 2022.

[228] M.G. Cooper, B.B. Mikic, and M. Michael Yovanovich. Thermal contact conductance. *International Journal of Heat and Mass Transfer*, 12(3):279–300, 1969.

[229] Jingwen Mo and Heng Ban. Measurements and theoretical modeling of effective thermal conductivity of particle beds under compression in air and vacuum. *Case Studies in Thermal Engineering*, 10:423–433, 2017.

[230] M. Díaz-Heras, J.F. Belmonte, and J.A. Almendros-Ibáñez. Effective thermal conductivities in packed beds: Review of correlations and its influence on system performance. *Applied Thermal Engineering*, 171:115048, 2020.

[231] Jihui Ye, Tiejue Chen, and Carolin Körner. Correlating outgassing and smoke phenomenon in electron beam powder bed fusion of Ti6Al4V using a residual gas analyzer. *Progress in Additive Manufacturing*, 10(4):2191–2203, 2025.

[232] Cang Zhao, Qilin Guo, Xuxiao Li, Niranjan Parab, Kamel Fezzaa, Wenda Tan, Lianyi Chen, and Tao Sun. Bulk-explosion-induced metal spattering during laser processing. *Physical Review X*, 9(2):021052, 2019.

[233] Saad A. Khairallah, Andrew T. Anderson, Alexander Rubenchik, and Wayne E. King. Laser powder-bed fusion additive manufacturing: Physics of complex melt flow and formation mechanisms of pores, spatter, and denudation zones. *Acta Materialia*, 108:36–45, 2016.

[234] Zheng Li, Hao Li, Jie Yin, Yan Li, Zhenguo Nie, Xiangyou Li, Deyong You, Kai Guan, Wei Duan, Longchao Cao, et al. A review of spatter in laser powder bed fusion additive manufacturing: In situ detection, generation, effects, and countermeasures. *Micromachines*, 13(8):1366, 2022.

[235] B. Schmitz and G. Goch. Photothermal radiometry–principle and applications. *ILM, Lasermeßtechnik, Ulm*, 2000.

[236] Barbara Larwa, Monika Gwadera, Izabela Kicińska, and Krzysztof Kupiec. Parameters of the Carslaw-Jaeger equation describing the temperature distribution in the ground. *Technical Transactions/Czasopismo Techniczne*, 11(9), 2018.

[237] Eric W. Weisstein. Fourier Series—Square Wave. From MathWorld—A Wolfram Web Resource, 2025. URL `https://mathworld.wolfram.com/FourierSeriesSquareWave.html`.

[238] McMaster-Carr Supply Company. Crucibles, 2025. URL `https://www.mcmaster.com/products/crucibles/`. Product catalog page.

[239] Denys Moskal, Jiří Martan, and Milan Honner. Scanning strategies in laser surface texturing: A review. *Micromachines*, 14(6):1241, 2023.

[240] N.M. Ferreira, M.C. Ferro, G. Gaspar, A.J.S. Fernandes, M.A. Valente, and F.M. Costa. Laser-induced hematite/magnetite phase transformation. *Journal of Electronic Materials*, 49(12):7187–7193, 2020.

[241] Laurent Weiss, M. Aillerie, Abdel Tazibt, and A. Tidu. Surface oxidation and phase transformation of the stainless steel by hybrid laser-waterjet impact. *Materials Research Express*, 1(3):036501, 2014.

[242] Nick A. Shepelin, Zahra P. Tehrani, Natacha Ohannessian, Christof W. Schneider, Daniele Pergolesi, and Thomas Lippert. A practical guide to pulsed laser deposition. *Chemical Society Reviews*, 52(7):2294–2321, 2023.

[243] Lukas Braun, Jonas Spielmann, Dmitry E. Doronkin, Carola Kuhn, Aleksandr Maliugin, Dmitry I. Sharapa, Isabel Huck, Jianing Bao, Steffen Tischer, Felix Studt, et al. Following the structural changes of iron oxides during reduction under transient conditions. *ChemSusChem*, 17(24):e202401045, 2024.

[244] EVS Explore: NCIt Concept C48491, 2025. URL `https://evsexplore.semantics.cancer.gov/evsexplore/concept/ncit/C48491?sources=NCI`. EVS Explore (NCI Thesaurus).

[245] William Nicholson. *The British Encyclopedia; or, Dictionary of Arts and Sciences comprising an accurate and popular view of the present improved state of human knowledge*. Whittingham, 1809.

[246] Inc. Accu-Glass Products. Rotary Feedthroughs, 2025. URL `https://www.accuglassproducts.com/motion-feedthroughs/rotary-feedthroughs`.

[247] G. David Scott and D. Marc Kilgour. The density of random close packing of spheres. *Journal of Physics D: Applied Physics*, 2(6):863, 1969.

[248] Pierre-Gilles de Gennes, Françoise Brochard-Wyart, and David Quéré. *Capillarity and Wetting Phenomena: Drops, Bubbles, Pearls, Waves*. Springer, New York, 2004.

[249] Boston Museum of Fine Arts. Oxalic acid — CAMEO Materials Database, 2025. URL `https://cameo.mfa.org/wiki/Oxalic_acid`. Accessed 2025-10-25.

[250] Rooha Khurram, Zhan Wang, Muhammad Fahad Ehsan, Song Peng, Maryam Shafiq, and Bushra Khan. Synthesis and characterization of an α-Fe2O3/ZnTe heterostructure for photocatalytic degradation of Congo red, methyl orange and methylene blue. *RSC Advances*, 10(73):44997–45007, 2020.

[251] M. Capra, A. Lodesani, A. Brambilla, M. Finazzi, L. Duò, F. Ciccacci, and A. Picone. Reversible metamorphosis from Fe_3O_4 to FeO of epitaxial iron oxide films grown on the Fe-p(1×1)O surface. *RSC Advances*, 11(19):11513–11518, 2021.

[252] Mohammed Liaket Ali, Quentin Fradet, and Uwe Riedel. Kinetic mechanism development for the direct reduction of single hematite pellets in H2/CO atmospheres. *Steel Research International*, 93(12):2200043, 2022.

[253] C-Y Kim, A.A. Escuadro, M.J. Bedzyk, L. Liu, and P.C. Stair. X-ray scattering study of the stoichiometric recovery of the $\alpha - \mathrm{Fe_2O_3}(0001)$ (0 0 0 1) surface. *Surface Science*, 572(2-3):239–246, 2004.

[254] Anglo Pacific Minerals. Hematite — product page, 2025. URL `https://angpacmin.com/products/hematite/`. Accessed 2025-11-09.

[255] Kremer Pigments GmbH & Co. KG. Magnetite, very fine (48800), 2025. URL `https://shop.kremerpigments.com/us/shop/pigments/48800-magnetite-very-fine.html`.

[256] FunCMater (Functional Materials). Iron(II) Oxide (FeO) Powder, 2025. URL `https://www.funcmater.com/iron-ii-oxide-feo-powder.html`.

[257] Frances E. Zengotita, Nabajit Lahiri, Mark H. Engelhard, Maksym Zhukovskyi, Manuel R. Vejar, Kevin M. Rosso, Carolyn I. Pearce, and Amy E. Hixon. Carbon-mediated oxygen vacancy creation at hematite interfaces. *The Journal of Physical Chemistry C*, 129(15):7316–7326, 2025.

[258] National Institute of Standards and Technology (NIST). NIST Physics Reference Data: Iron — Table 5, 2025. URL `https://physics.nist.gov/PhysRefData/Handbook/Tables/irontable5.htm`. Accessed 2025-10-17.

[259] Stéphanie Krins, S. Oppel, Nicolas Huet, J. Von Zanthier, and Thierry Bastin. Isotope shifts and hyperfine structure of the Fe I 372-nm resonance line. *Physical Review A—Atomic, Molecular, and Optical Physics*, 80(6):062508, 2009.

[260] E. te Sligte, R.C.M. Bosch, B. Smeets, P. van der Straten, H.C.W. Beijerinck, and K.A.H. van Leeuwen. Magnetic nanodots from atomic Fe: Can it be done? *Proceedings of the National Academy of Sciences*, 99(suppl_2):6509–6513, 2002.

[261] B. Smeets, R.W. Herfst, L.P. Maguire, E. te Sligte, P. van der Straten, H.C.W. Beijerinck, and K.A.H. van Leeuwen. Laser collimation of an Fe atomic beam on a leaky transition. *Applied Physics B*, 80(7):833–839, 2005.

[262] E. te Sligte, B. Smeets, K.M.R. van der Stam, R.W. Herfst, P. van der Straten, H.C.W. Beijerinck, and K.A.H. van Leeuwen. Atom lithography of Fe. *Applied Physics Letters*, 85(19):4493–4495, 2004.

[263] Bernd Kaifler, Christian Büdenbender, Peter Mahnke, Matthias Damm, Daniel Sauder, Natalie Kaifler, and Markus Rapp. Demonstration of an iron fluorescence lidar operating at 372 nm wavelength using a newly-developed Nd:YAG laser. *Optics Letters*, 42(15):2858–2861, 2017.

[264] Timothy J. Kane, Jun Qian, Daniel R. Scherrer, Daniel C. Senft, W. Matthew Pfenninger, George C. Papen, and Chester S. Gardner. Lidar probing of the mesosphere: Simultaneous observations of sporadic sodium and iron formations, calcium ion layers, neutral temperature and winds. In *Sixteenth International Laser Radar Conference, Part 1.* NASA Langley Research Center, July 1992.

[265] Chester S. Gardner, George C. Papen, Xinzhao Chu, and Weilin Pan. First lidar observations of middle atmosphere temperatures, Fe densities, and polar mesospheric clouds over the North and South Poles. *Geophysical Research Letters*, 28(7):1199–1202, 2001.

[266] J.C. Diettrich, G.J. Nott, P.J. Espy, G.R. Swenson, X. Chu, M.J. Taylor, D.M. Riggin, and D.C. Fritts. High frequency atmospheric gravity-wave properties using Fe-lidar and OH-imager observations. *Geophysical Research Letters*, 32 (9), 2005.

[267] George C. Papen and Daniel Treyer. Comparison of an Fe Boltzmann temperature lidar with a Na narrow-band lidar. *Applied Optics*, 37(36):8477–8481, 1998.

[268] Xinzhao Chu, Weilin Pan, George C. Papen, Chester S. Gardner, and Jerry A. Gelbwachs. Fe Boltzmann temperature lidar: design, error analysis, and initial results at the North and South Poles. *Applied Optics*, 41(21):4400–4410, 2002.

[269] D.S. Hughes and Carl Eckart. The effect of the motion of the nucleus on the spectra of Li I and Li II. *Physical Review*, 36(4):694, 1930.

[270] William Holland King. *Isotope Shifts in Atomic Spectra*. Springer Science & Business Media, 2013.

[271] U.S. National Park Service. The Calutron Girls, 1944. URL `https://www.nps.gov/articles/000/the-calutron-girls.htm`. Accessed 2025-11-10.

[272] Jesse W. Beams and F.B. Haynes. The separation of isotopes by centrifuging. *Physical Review*, 50(5):491, 1936.

[273] Alfred L. Yergey and A. Karl Yergey. Preparative scale mass spectrometry: A brief history of the calutron. *Journal of the American Society for Mass Spectrometry*, 8(9):943–953, 1997.

[274] Arvin S. Quist. A History of Classified Activities at Oak Ridge National Laboratory. Technical report, Oak Ridge National Lab.(ORNL), Oak Ridge, TN (United States), 2001.

[275] Office of Scientific U.S. Department of Energy and OpenNet Technical Information (OSTI). Alpha Racetrack — Manhattan Project Photo Gallery. URL `https://www.osti.gov/opennet/manhattan-project-history/Resources/photo_gallery/alpha_racetrack.htm`.

[276] Oak Ridge National Laboratory (ORNL). Isotope Development and Production, . URL `https://www.ornl.gov/research-area/isotope-development-and-production`. Accessed 2025-10-02.

[277] Oak Ridge National Laboratory (ORNL). Stable Isotope Production and Research Center, . URL `https://www.ornl.gov/content/stable-isotope-production-and-research-center`. Accessed 2025-10-02.

[278] Oak Ridge National Laboratory (ORNL). Energy secretary breaks ground on new isotope facility at ORNL, . URL `https://www.ornl.gov/news/energy-secretary-breaks-ground-new-isotope-facility-ornl`.

[279] Oak Ridge National Laboratory (ORNL). Oak Ridge Facilities Provide Significant Isotope Production, . URL `https://www.ornl.gov/news/oak-ridge-facilities-provide-significant-isotope-production`.

[280] Alvin Weinberg. The State of the Laboratory. *ORNL Review*, 3(3):1–13, 1970. Winter 1970 issue.

[281] Oak Ridge National Laboratory (ORNL). Rescuing History, . URL `https://www.ornl.gov/news/rescuing-history`.

[282] US Department of Energy Office of Scientific and Technical Information. Meeting isotope needs and capturing opportunities for the future: The 2015 long range plan for the DOE-NP isotope program, NSAC Isotopes Subcommitee, July 2015, 2015. URL `https://www.osti.gov/biblio/1298983`.

[283] U.S. Department of Energy, Office of Science. FY 2020 Congressional Budget Justification, 2019. URL `https://science.osti.gov/-/media/budget/pdf/sc-budget-request-to-congress/fy-2020/FY_2020_DOE-Congressional-Budget-justification.pdf`. Congressional Budget Request.

[284] Nuclear Science Advisory Committee Isotopes (NSACI) Subcommittee. Meeting Isotope Needs and Capturing Opportunities for the Future: The 2015 Long Range Plan for the DOE-NP Isotope Program, July 2015. URL `https://science.osti.gov/~/media/np/nsac/pdf/docs/2015/2015_NSACI_R`

`eport_to_NSAC_Final.pdf`. Report to the Nuclear Science Advisory Committee (NSAC).

[285] International Panel on Fissile Materials. U.S. Department of Energy report (PDF) — IPFM Library. URL `https://fissilematerials.org/library/doe15b.pdf`. Accessed 2025-10-31.

[286] T.S. Bigelow, F.J. Tarallo, and N.R. Stevenson. Production of stable isotopes utilizing the plasma separation process. *Nuclear Instruments and Methods in Physics Research Section B: Beam Interactions with Materials and Atoms*, 241 (1-4):652–654, 2005.

[287] Jehanne Gillo. Status of Isotope Program. Presentation to the Nuclear Science Advisory Committee (NSAC), March 2011. URL `https://science.osti.gov/-/media/np/nsac/pdf/mtg-3211/NSAC_isotope_0311.pdf`.

[288] U.S. Department of Energy, Office of Science, Isotope Program and National Isotope Development Center (NIDC). Isotope program — enriched stable isotopes, 2019. URL `https://www.isotopes.gov/sites/default/files/2019-07/Isotope-Program--Enriched-Stable-Isotopes.pdf`.

[289] U.S. Department of Energy Isotope Program; National Isotope Development Center (NIDC). Department of Energy awards $88M contract to build Stable Isotope Production and Research Facility. URL `https://www.isotopes.gov/department-energy-awards-88m-contract-build-stable-isotope-production-and-research-facility`. Accessed 2025-10-05.

[290] Oak Ridge National Laboratory (ORNL). Investment in New Facilities Expands Critical Isotope Supply Chains, . URL `https://www.ornl.gov/organization-news/investment-new-facilities-expands-critical-isotope-supply-chains`. Accessed 2025-10-03.

[291] Oak Ridge National Laboratory (ORNL) Isotope Science & Engineering Directorate. ISED Facility Overview - SIPF, 2025. URL `https://www.ornl.gov/file/ised-facility-overview-sipf/display`.

[292] E. M. Campbell. Laser Programs, the First 25 Years, 1972–1997. Technical report, Lawrence Livermore National Laboratory, 1998. URL `https://www.osti.gov/servlets/purl/16710`.

[293] Federation of American Scientists Project on Government Secrecy. Los Alamos National Laboratory publication. URL `https://sgp.fas.org/othergov/doe/lanl/pubs/00416665.pdf`.

[294] U.S. General Accounting Office. T-RCED-87-15A, 1987. URL `https://www.gao.gov/assets/t-rced-87-15a.pdf`.

[295] U.S. General Accounting Office. RCED-88-18, 1988. URL `https://www.gao.gov/assets/rced-88-18.pdf`.

[296] Lawrence Livermore National Laboratory (LLNL). Building 332 Fact Sheet, February 2022. URL `https://enviroinfo.llnl.gov/sites/enviroinfo/files/2022-02/Building332_reduced.pdf`.

[297] Christopher A. Haynam, Brian J. Comaskey, John Conway, Jon Eggert, Joseph Glaser, Edmund W. Ng, Jeffrey A. Paisner, Richard W. Solarz, and Earl F. Worden. Gadolinium Enrichment Technology at Lawrence Livermore National Laboratory. In *Laser Isotope Separation*, volume 1859, pages 24–36. SPIE, 1993.

[298] Charles Bradley Moore, National Research Council, et al. *Alternative Applications of Atomic Vapor Laser Isotope Separation Technology: A Report*. National Academies, 1991.

[299] INIS International Atomic Energy Agency (IAEA). INIS record a3j89-vqm50, 2025. URL `https://inis.iaea.org/records/a3j89-vqm50`. Accessed 2025-10-01.

[300] Lawrence Livermore National Laboratory (LLNL). AVLIS Technology Transfer, 2025. URL `https://www.llnl.gov/avlis-technology-transfer`. Accessed 2025-10-01.

[301] Laser Focus World. US Enrichment Corp. shuts down AVLIS, 2025. URL `https://www.laserfocusworld.com/lasers-sources/article/16548729/us-enrichment-corp-shuts-down-avlis`. Accessed 2025-10-07.

[302] U.S. General Accounting Office. Rced-91-88, 1991. URL `https://www.gao.gov/assets/rced-91-88.pdf`.

[303] Petr Artemovich Bokhan, Vladimir Vasilevich Buchanov, Nikolai Vasilevich Fateev, Mikhail Mikhajlovich Kalugin, Mishik Airazatovich Kazaryan, Alexander M. Prokhorov, and Dmitrij Eduardovich Zakrevskii. *Laser Isotope Separation in Atomic Vapor*. John Wiley & Sons, 2006.

[304] Hyunmin Park, Duck-Hee Kwon, Yong Ho Cha, Taek-Soo Kim, Jaemin Han, Kwang-Hoon Ko, Do-Young Jeong, and Cheol-Jung Kim. Stable isotope production of ^{168}Yb and ^{176}Yb for industrial and medical applications. *Journal of Nuclear Science and Technology*, 45(sup6):111–116, 2008.

[305] Do-Young Jeong, Kwang-Hoon Ko, Gwon Lim, and Cheol-Jung Kim. Method for isotope separation of thallium, January 29 2008. US Patent 7,323,651.

[306] M.V. Suryanarayana and M. Sankari. Numerical study of the laser isotope separation of optically pumped ^{102}Pd. *Scientific Reports*, 14(1):4080, 2024.

[307] M.V. Suryanarayana. Laser isotope separation of ^{203}Tl through pulsed laser optical pumping. *Journal of the Optical Society of America B*, 41(2):311–320, 2024.

[308] M. Guina, A. Rantamäki, and Antti Härkönen. Optically pumped VECSELs: review of technology and progress. *Journal of Physics D: Applied Physics*, 50 (38):383001, 2017.

[309] Alexei Baranov and Eric Tournié. *Semiconductor Lasers: Fundamentals and Applications*. Elsevier, 2013.

[310] Mark G. Raizen and Bruce Klappauf. Magnetically activated and guided isotope separation. *New Journal of Physics*, 14(2):023059, 2012.

[311] M. Jerkins, I. Chavez, U. Even, and M.G. Raizen. Efficient isotope separation by single-photon atomic sorting. *Physical Review A—Atomic, Molecular, and Optical Physics*, 82(3):033414, 2010.

[312] Thomas R. Mazur, Bruce Klappauf, and Mark G. Raizen. Demonstration of magnetically activated and guided isotope separation. *Nature Physics*, 10(8): 601–605, 2014.

[313] Mark G. Raizen and Bruce G. Klappauf. Isotope separation by magnetic activation and separation, March 18 2014. US Patent 8,672,138.

[314] Sharmila Banerjee, M.R.A. Pillai, and F.F. Knapp. Lutetium-177 therapeutic radiopharmaceuticals: linking chemistry, radiochemistry, and practical applications. *Chemical Reviews*, 115(8):2934–2974, 2015.

[315] H.J. Metcalf. *Laser Cooling of Atoms*. Berlin: Springer, 1999.

[316] E. Anciaux, G. Stratis, and M.G. Raizen. Brightening of a supersonic beam of neutral atoms. *Physica Scripta*, 93(12):124009, 2018.

[317] Jens-Volker Kratz. *Nuclear and Radiochemistry: Fundamentals and Applications*. John Wiley & Sons, 2022.

[318] Nikolay V. Vitanov, Andon A. Rangelov, Bruce W. Shore, and Klaas Bergmann. Stimulated Raman adiabatic passage in physics, chemistry, and beyond. *Reviews of Modern Physics*, 89(1):015006, 2017.

[319] Anthony E Siegman. *Lasers*. University Science Books, 1986.

[320] Isabelle Riou, Nicolas Mielec, Grégoire Lefèvre, Marco Prevedelli, Arnaud Landragin, Philippe Bouyer, Andrea Bertoldi, Remi Geiger, and Benjamin Canuel. A marginally stable optical resonator for enhanced atom interferometry. *Journal of Physics B: Atomic, Molecular and Optical Physics*, 50(15):155002, 2017.

[321] S. Miyoki, M. Ohashi, K. Waseda, H. Karoji, and T. Tomaru. Manufacture of a 10-km-scale radius-of-curvature surface by use of a thin-film coating technique. *Optics Letters*, 30(11):1399–1401, 2005.

[322] David Martin-Sanchez, Jing Li, Dylan M. Marques, Edward Z. Zhang, Peter R.T. Munro, Paul C. Beard, and James A. Guggenheim. ABCD transfer matrix model of Gaussian beam propagation in Fabry-Perot etalons. *Optics Express*, 30(26):46404–46417, 2022.

[323] Nur Ismail, Cristine Calil Kores, Dimitri Geskus, and Markus Pollnau. Fabry-Pérot resonator: spectral line shapes, generic and related Airy distributions, linewidths, finesses, and performance at low or frequency-dependent reflectivity. *Optics Express*, 24(15):16366–16389, 2016.

[324] Joshua R. Smith et al. The path to the enhanced and advanced LIGO gravitational-wave detectors. *Classical and Quantum Gravity*, 26(11):114013, 2009.

[325] Tariq Shamim Khwaja and Syed Azer Reza. Power transmittance of a laterally shifted Gaussian beam through a circular aperture. *arXiv preprint arXiv:1605.04241*, 2016.

[326] C.J. Dai, S.F. Hu, and J. Lu. Multistep excitation of autoionizing states of neutral strontium. *Journal of Quantitative Spectroscopy and Radiative Transfer*, 56(2):255–262, 1996.

[327] Norman Ramsey. *Molecular Beams*, volume 20. Oxford University Press, 1956.

[328] Ariel Anbar, Joseph Skulan, Gwyneth Gordon, and Jennifer Morgan. Isotopic biomarkers for rapid assessment of bone mineral balance in biomedical applications, February 16 2016. US Patent 9,261,519.

[329] Mark G. Raizen, David E. Kaplan, and Surjeet Rajendran. Do atoms age? *Physics Letters B*, 832:137224, 2022.

[330] Mark G. Raizen. New tests of quantum mechanics with unstable nuclei. *Physics Letters B*, page 139480, 2025.

[331] Ashutosh Dash, Maroor Raghavan Ambikalmajan Pillai, and Furn F. Knapp. Production of 177 Lu for targeted radionuclide therapy: available options. *Nuclear Medicine and Molecular Imaging*, 49:85–107, 2015.

[332] M. Brownnutt, V. Letchumanan, G. Wilpers, R.C. Thompson, P. Gill, and A.G. Sinclair. Controlled photoionization loading of 88Sr+ for precision ion-trap experiments. *Applied Physics B*, 87(3):411–415, 2007.

[333] National Institute of Standards and Technology. NIST Atomic Spectra Database Lines Form. URL `https://physics.nist.gov/PhysRefData/ASD/lines_form.html`.

[334] S. Mahmood, N. Amin, Y. Jamil, R. Ali, M.A. Baig, et al. Measurements of photoionization cross sections from the 5s5p $^1P_1$ and 5s6s $^1\mathrm{S}_0$ excited states of strontium. *Journal of Physics B: Atomic, Molecular and Optical Physics*, 39 (7):1587, 2006.

[335] W. Mende, K. Bartschat, and M. Kock. Near-threshold photoionization from the Sr I (5s5p) ${}^1P^{\text{o}}{}_1$ state. *Journal of Physics B: Atomic, Molecular and Optical Physics*, 28(12):2385, 1995.

[336] S.K. Borisov, M.A. Kuz'mina, and V.A. Mishin. A study of isotopically selective photoionization of ytterbium atoms for laser isotope separation. *Journal of Russian Laser Research*, 17(4):332–345, 1996.

[337] S.K. Borisov, Marina Al'bertovna Kuz'mina, and Vladimir Alekseevich Mishin. Selective photoionisation of 168Yb in an extended optically dense medium. *Quantum Electronics*, 28(2):169, 1998.

[338] Aleksei N. Tkachev and Sergei I. Yakovlenko. Multistage photoionisation of ytterbium. *Quantum Electronics*, 26(9):839, 1996.

[339] Aleksei N. Tkachev and Sergei I. Yakovlenko. On laser rare-isotope separation. *Quantum Electronics*, 33(7):581, 2003.

[340] Wolfgang Demtröder. *Laser Spectroscopy: Vol. 1, Basic Principles*. Springer, 2008.

[341] L.O. Love. Electromagnetic separation of isotopes at Oak Ridge: An informal account of history, techniques, and accomplishments. *Science*, 182(4110):343–352, 1973.

[342] Thorlabs, Inc. Nanosecond Pulsed Laser Systems. URL `https://www.thorlabs.com/newgrouppage9.cfm?objectgroup_id=10823&pn=NPL41B#ad-image-0`.

[343] Ekspla, Inc. NT260 series. URL `https://ekspla.com/products/narrow-linewidth-tunable-wavelength-laser-nt260/#specifications`.

[344] Quantel, Inc. Peacock XT 355. URL `www.quantel-laser.com/en/products/item/peacock-xt-355-405-nm-2850-um.html`.

[345] Marcis Auzinsh, Dmitry Budker, and Simon Rochester. *Optically Polarized Atoms: Understanding Light-Atom Interactions.* Oxford University Press, 2010.

[346] Diagnocine. PDMS Sheets and Films. URL `https://diagnocine.com/Product/PDMS-Sheets-and-Films/93366`.

[347] M. Stephens, R. Rhodes, and C. Wieman. Study of wall coatings for vapor-cell laser traps. *Journal of Applied Physics*, 76(6):3479–3488, September 1994.

[348] H. Mark Goldenberg, Daniel Kleppner, and Norman F. Ramsey. Atomic beam resonance experiments with stored beams. *Physical Review*, 123(2):530, 1961.

[349] Y.W. Yi, H.G. Robinson, Svenja Knappe, J.E. Maclennan, C.D. Jones, Chengjie Zhu, N.A. Clark, and John Kitching. Method for characterizing self-assembled monolayers as antirelaxation wall coatings for alkali vapor cells. *Journal of Applied Physics*, 104(2), 2008.

[350] M. H. Anderson, J. R. Ensher, M. R. Matthews, C. E. Wieman, and E. A. Cornell. Observation of Bose-Einstein condensation in a dilute atomic vapor. *Science*, 269(5221):198–201, July 1995.

[351] Ole Kock, Wei He, Dariusz Świerad, Lyndsie Smith, Joshua Hughes, Kai Bongs, and Yeshpal Singh. Laser controlled atom source for optical clocks. *Scientific Reports*, 6(1):37321, 2016.

[352] Masami Yasuda, Takehiko Tanabe, Takumi Kobayashi, Daisuke Akamatsu, Takumi Sato, and Atsushi Hatakeyama. Laser-controlled cold ytterbium atom source for transportable optical clocks. *Journal of the Physical Society of Japan*, 86(12):125001, 2017.

[353] Haotian Chi, Wei Quan, Junying Zhang, Lijiang Zhao, and Jiancheng Fang. Advances in anti-relaxation coatings of alkali-metal vapor cells. *Applied Surface Science*, 501:143897, January 2020.

[354] Naota Sekiguchi, Atsushi Hatakeyama, Kazane Okuma, and Hiroaki Usui. Scattering of an alkali-metal atomic beam on anti-spin-relaxation coatings. *Physical Review A*, 98(4):042709, October 2018.

[355] N. Huet, M. Pettens, and T. Bastin. Isotope shifts and hyperfine structure of the laser-cooling Fe I 358-nm line. *Physical Review A*, 92(5):052507, November 2015.

[356] Andrew D. Ludlow, Martin M. Boyd, Jun Ye, E. Peik, and P.O. Schmidt. Optical atomic clocks. *Reviews of Modern Physics*, 87(2):637–701, June 2015.

[357] T. D. Ladd, F. Jelezko, R. Laflamme, Y. Nakamura, C. Monroe, and J. L. O'Brien. Quantum computers. *Nature*, 464(7285):45–53, March 2010.

[358] C.L. Degen, F. Reinhard, and P. Cappellaro. Quantum sensing. *Reviews of Modern Physics*, 89(3):035002, July 2017.

[359] Inês Teixeira, Inês Castro, Violeta Carvalho, Cristina Rodrigues, Andrews Souza, Rui Lima, Senhorinha Teixeira, and João Ribeiro. Polydimethylsiloxane mechanical properties: a systematic review. *AIMS Materials Science*, 8(6), 2021.

[360] Dow Chemical Company. SYLGARD 184 Silicone Elastomer Kit — Product Overview, 2025. URL `https://www.dow.com/en-us/pdp.sylgard-184-silicone-elastomer-kit.01064291z.html#overview`.

[361] World Precision Instruments (WPI). SYLG184 Instruction Manual. URL `https://www.wpiinc.com/media/wysiwyg/pdf/SYLG184_IM.pdf`.

[362] Shuping Wang, Ajay Kallur, and Abeselom Goshu. Fabrication and characterization of PDMS thin film. In *Organic Photonic Materials and Devices XIII*, volume 7935, pages 109–114. SPIE, 2011.

[363] David B. Hall, Patrick Underhill, and John M. Torkelson. Spin coating of thin and ultrathin polymer films. *Polymer Engineering & Science*, 38(12): 2039–2045, 1998.

[364] Matej Bračič, Tamilselvan Mohan, Rupert Kargl, Thomas Griesser, Silvo Hribernik, Stefan Köstler, Karin Stana-Kleinschek, and Lidija Fras-Zemljič. Preparation of PDMS ultrathin films and patterned surface modification with cellulose. *RSC Advances*, 4(23):11955–11961, 2014.

[365] V.J. Ajith, Aaron Barr, and Mark Raizen. Surface scattering of atoms for high-sensitivity spectroscopy. *Physical Review Applied*, 23(6):064063, 2025.

[366] Alfred G. Emslie, Francis T. Bonner, and Leslie G. Peck. Flow of a viscous liquid on a rotating disk. *Journal of Applied Physics*, 29(5):858–862, 1958.

[367] Instras. Spin coaters, 2025. URL `https://instras.com/index.php/spin-coaters/`.

[368] Ted Pella. SEM Mounting Adhesives — Carbon/Conductive Tapes and Tabs. URL `https://www.tedpella.com/SEMmisc_html/SEMadhes.aspx#_16073`.

[369] H.M. Brothers Jr., T. Boehmer, R.A. Campbell, S. Dorn, J.J. Kerbleski, S. Lewis, C. Mund, D. Pero, K. Saito, M. Wieser, et al. Determination of cyclic volatile methylsiloxanes in personal care products by gas chromatography. *International Journal of Cosmetic Science*, 39(6):580–588, 2017.

[370] J.J. Park and C.H. Clatterbuck. A technique for reducing the outgassing of silicone compounds. In *ESA Spacecraft Materials in a Space Environment*, 1982.

[371] Gelest Inc. Gelest Product SIO6700.0, 2025. URL `https://www.gelest.com/product/SIO6700.0/`.

[372] Vacseal / NASA Reference Compilation. Outgassing Data for Selecting Spacecraft Materials (REV), 2017. URL `https://vacseal.net/wp-content/uploads/2017/08/Outgassing-Data-for-Selecting-Spacecraft-Materials-REV.pdf`.

[373] SwanTek. Element14 PDMS. URL `https://www.swantek.com/html/element14_pdms.pdf`.

[374] Ruwan Senaratne, Shankari V. Rajagopal, Zachary A. Geiger, Kurt M. Fujiwara, Vyacheslav Lebedev, and David M. Weld. Effusive atomic oven nozzle design using an aligned microcapillary array. *Review of Scientific Instruments*, 86(2), 2015.

[375] Igal Bucay. *Surface Ionization of Metastable Calcium and Ytterbium Atoms.* Doctoral dissertation, The University of Texas at Austin, 2019. URL `https://www.proquest.com/docview/2479389916/abstract/7C2F16124BA342D8PQ/1`.

[376] John H. Moore, Christopher C. Davis, and Michael A. Coplan. *Building Scientific Apparatus.* Cambridge University Press, Cambridge, 2nd edition, 1991.

[377] *CRC Handbook of Chemistry and Physics.* Chemical Rubber Company, Boca Raton, FL, 61st edition, 1981.

[378] Y. Takasu, K. Komori, K. Honda, M. Kumakura, T. Yabuzaki, and Y. Takahashi. Photoassociation spectroscopy of laser-cooled ytterbium atoms. *Physical Review Letters*, 93(12):123202, 2004.

[379] Ayan Banerjee, Umakant D. Rapol, Dipankar Das, Anusha Krishna, and Vasant Natarajan. Precise measurements of UV atomic lines: hyperfine structure and isotope shifts in the 398.8 nm line of Yb. *Europhysics Letters*, 63(3):340, 2003.

[380] Jauch Quartz GmbH & Co. KG. *Quartz Crystals in Theory and Practice*, 2022. URL `https://www.bce.it/wp-content/uploads/2022/04/JAUCH-Quartz-Crystals-in-Theory-and-Practice_BCE.pdf`.

[381] Günter Sauerbrey. Use of a quartz vibrator from weighing thin films on a microbalance. *Zeitschrift für Physik*, 155:206, 1959.

[382] S. N. Atutov and A. I. Plekhanov. Accurate measurement of the sticking time and sticking probability of Rb atoms on a polydimethylsiloxane coating. *Journal of Experimental and Theoretical Physics*, 120(1):1–8, January 2015.

[383] Guiguan Zhang, Yuli Sun, Bingkun Qian, Hang Gao, and Dunwen Zuo. Experimental study on mechanical performance of polydimethylsiloxane (PDMS) at various temperatures. *Polymer Testing*, 90:106670, October 2020.